

A Measurement of the Effective Electron Neutral Current Coupling Parameters from Polarized Bhabha Scattering at the Z0 Resonance*

Matthew D. Langston

Stanford Linear Accelerator Center
Stanford University
Stanford, CA 94309

SLAC-Report-629
June 2003

Prepared for the Department of Energy
under contract number DE-AC03-76SF00515

Printed in the United States of America. Available from the National Technical Information Service, U.S. Department of Commerce, 5285 Port Royal Road, Springfield, VA 22161.

*Ph.D. thesis, University of Oregon, Eugene, OR 97403.

A MEASUREMENT OF THE EFFECTIVE ELECTRON NEUTRAL CURRENT
COUPLING PARAMETERS FROM POLARIZED BHABHA SCATTERING AT THE
Z⁰ RESONANCE

by

MATTHEW D. LANGSTON

A DISSERTATION

Presented to the Department of Physics
and the Graduate School of the University of Oregon
in partial fulfillment of the requirements
for the degree of
Doctor of Philosophy

June 2003

“A Measurement of the Effective Electron Neutral Current Coupling Parameters from Polarized Bhabha Scattering at the Z0 Resonance”, a dissertation prepared by Matthew D. Langston in partial fulfillment of the requirements for the Doctor of Philosophy degree in the Department of Physics. This dissertation has been approved and accepted by:

Dr. James E. Brau, Chair of the Examining Committee

Date

Committee in charge: Dr. Raymond Frey
Dr. Nilendra Deshpande
Dr. J. David Cohen
Dr. Eugene Humphreys

Accepted by:

Dean of the Graduate School

The effective electron neutral current coupling parameters, \overline{g}_V^e and \overline{g}_A^e , have been measured from analyzing 43,222 polarized Bhabha scattered events ($e^+e^- \rightarrow e^+e^-$) using the SLAC Large Detector (SLD) experiment at the Stanford Linear Accelerator Center (SLAC). The SLAC Linear Collider (SLC) produced the Bhabha scattered events by colliding polarized electrons, with an average polarization of 74%, with unpolarized positrons at an average center-of-mass energy of 91.25 GeV. The analysis used the entire SLD data sample collected between 1994 and 1998 (the last year the SLD detector collected data). The results are

$$\overline{g}_A^e = -0.5038 \pm 0.0010 \text{ (stat.)} \pm 0.0043 \text{ (sys.)}$$

All Bhabha scattered events within the angular acceptance of the SLD calorimeter subsystems were used in this analysis, including both small-angle events ($28 \text{ mrad.} \leq \theta \leq 68 \text{ mrad.}$) measured by the Silicon/Tungsten Luminosity Monitor (LUM),

and large angle events ($0 \leq |\cos \theta| \leq 0.9655$) measured by the Liquid Argon Calorimeter (LAC). Using all of the data in this manner allows for the high-precision measurement of the luminosity provided by the LUM to constrain the uncertainty on \overline{g}_V^e and \overline{g}_A^e .

The measured integrated luminosity for the combined 1993 through 1998 SLD data sample is $\mathcal{L}_{\text{Integrated}} = 19,247 \pm 17(\text{stat.}) \pm 146(\text{sys.}) \text{ nb}^{-1}$.

In contrast with other SLD precision measurements of the effective weak mixing angle ($\sin^2 \theta_W^{\text{eff}}$), which are sensitive to the ratio $\overline{g}_V^e / \overline{g}_A^e$, this result independently determines \overline{g}_V^e and \overline{g}_A^e . The analysis techniques to measure \overline{g}_V^e and \overline{g}_A^e are described, and the results are compared with other SLD measurements as well as other experiments.

CURRICULUM VITA

NAME OF AUTHOR: Matthew D. Langston

PLACE OF BIRTH: Wenatchee, WA

GRADUATE AND UNDERGRADUATE SCHOOLS ATTENDED:

University of Oregon
Whitman College

DEGREES AWARDED:

Doctor of Philosophy in Physics, 2003, University of Oregon
Master of Science in Physics, 1991, University of Oregon
Bachelor of Arts in Physics and Mathematics, 1989, Whitman College

AREAS OF SPECIAL INTEREST:

Experimental High Energy Physics
Large Scale Data Analysis

PROFESSIONAL EXPERIENCE:

Research Assistant
Department of Physics, University of Oregon, Eugene, OR
1992-2003

Principal Scientist
Network Physics Inc., Menlo Park, CA
2001

Run Coordinator
SLD Experiment, Stanford Linear Accelerator Center, Menlo Park, CA
1994-1998

Luminosity Monitor Commissioner
SLD Experiment, Stanford Linear Accelerator Center, Menlo Park, CA
1994-1998

AWARDS AND HONORS:

Oregon Laurel Tuition Award, 1992
Pugh Science Grant, 1988

ACKNOWLEDGMENTS

Above all I wish to thank my parents, Clyde and Rosalie Langston, for making all of this possible. Their emphasis on the importance of education form some of my earliest memories, and they have always been an unwavering source of support, encouragement and love throughout all of this. My formal education, culminating in this Ph.D., simply would not have been possible were it not for their hard work and many sacrifices to send their son through school. I will forever be in their debt, and it is to them that I dedicate this dissertation. Thank you mom and dad.

Words simply cannot convey how thankful I am to my wife Kerry, but I will try nonetheless. From that day many years ago when she put her few worldly possessions along with mine into a little Ryder truck and moved with me on a leap of faith from Eugene, OR to Palo Alto, CA, Kerry has stood by my side and been an unending source of love, support and encouragement. I would not have made it this far without Kerry. Thank you Kerry – I love you.

I am deeply indebted to my advisor, Dr. Jim Brau, for his unwavering support and encouragement, and his unlimited patience, in seeing my formal education through to its conclusion. I feel the deepest gratitude to Jim for the faith he placed in me by providing the numerous leadership opportunities I was allowed to assume within the SLD collaboration. There was much, much more to my education that I received during my time at SLAC than what is reflected in the pages of this dissertation. I am deeply appreciative to Jim for allowing me to explore this wonderful place and learn what it had to offer.

I am especially thankful to Dr. Ray Frey and Dr. David Strom of the University of Oregon for their friendship, help and guidance. I also thank Dr. Anatoli Arodzero for both his friendship and for teaching me proper scientific lab technique. I thank Dr. Kevin Pitts, Jim's first graduate student, for his excellent work with the SLD Luminosity Monitor. I also thank Dr. Jenny Huber and Dr. Masako Iwasaki for their excellent work on the Luminosity Monitor as well. Other UO students who befriended me and showed me the ropes early on were Dr. Hwanbae Park and Dr. Hyun Wang. Finally, special thanks to Elaine Wigget and Jan Blankenship for taking care of my UO business while I was at SLAC.

There are numerous talented people at SLAC who had a significant impact on me. In particular I thank Dr. Phil Burrows for his friendship, guidance, and impeccable taste in wine. Phil befriended Kerry and I within hours of our arrival to SLAC, and made us feel immediately at home. I am grateful to Dr. Tom Markiewicz for being both a mentor and a friend. I also thank Dr. Peter Rowson and Dr. Mike Woods for their friendship, help and guidance over the years. I thank Dr. Paul Kunz for being my early mentor in computer science, and for his friendship over the years. My passion for the study of computer science as it applies to data analysis was inspired by Paul, and I am thankful for, and I will dearly miss, the countless conversations we shared together. I also thank Dr. Tom Pavel for his tutelage and friendship over the years. Tom was a kindred spirit who successfully balanced the competing passions for both physics and computer science as a graduate student, and set an example for me to follow.

A very large part of my education while at SLAC was provided by my good friends in Dr. Marty Breidenbach's group. In particular I thank Marty for providing me with numerous leadership opportunities within the SLD collaboration. I thank Dr. Richard Dubois not only for his physics and technical expertise, but for his warm friendship over the years. I also

thank Dr. Tony Johnson for his friendship, for humoring my endless questions about the SLD offline software, and for the many hours of technical discussions which I have thoroughly enjoyed and will miss. I also thank Dr. Jim “JJ” Russell for his friendship and help over the years. Many, many thanks to Dr. Tony Waite, whose pursuit of excellence balanced with his pragmatic *get the job done* attitude I have always admired, and it is his example which I strive for in my own work. I thank Tony for putting up with all of my late night calls from the CEH, and for his help, guidance and friendship. Finally, I thank Karen Heidenreich for her friendship and her invaluable help navigating the SLD databases.

I couldn't have asked for better officemates during my graduate student years than Dr. Jingchen Zhou and Xiaoqing “XQ” Yang, both of whom I entered graduate school with and whom I hold tremendous respect for. Other officemates I developed close friendships with include Sean Walston, Dr. Eugeni Grauges and Dr. Olga Igonkina.

My research would not have been possible were it not for the tireless efforts of those who contributed to the construction and operation of the SLC and the SLD. I particularly thank SLD machinist (and now Count Basie Orchestra vocalist) Jamie Davis, and all around handyman Howard Rogers. Both men came through for me on more than one occasion by machining or making just the right part hours before the SLD doors were supposed to close. Not only were these two professional in their jobs, but they made the SLD CEH a fun place to work. I am extremely fortunate to have worked with these men, and to call them friends.

This work was supported in part by a grant from the U.S. Department of Energy Division of High Energy Physics to the High Energy Physics Group at the University of Oregon, and by U.S. Department of Energy contract DE-AC03-76SF00515.

TABLE OF CONTENTS

Chapter	Page
1 Introduction.....	1
2 The Standard Model of Electroweak Interactions.....	5
2.1 The SU(2) and U(1) Symmetries	5
2.2 The Matter Content.....	6
2.3 The Physical Bosons: W^\pm , Z^0 and Photon	8
2.4 The Electroweak Lagrangian of the Standard Model.....	10
2.5 Standard Model Parameters	15
2.6 Radiative Corrections	16
2.7 Tests of the Standard Model.....	17
3 Bhabha Scattering	20
3.1 Analytical Expression for the Bhabha Differential Cross Section	21
3.2 Radiative Corrections	26
4 Experimental Apparatus: SLC and SLD.....	36
4.1 SLAC Linear Collider (SLC)	37
4.1.1 SLC Polarized Electron Source.....	40
4.1.2 Spin Transport Through the SLC.....	44
4.1.3 Polarization Measurement: SLD Polarimeter.....	45
4.1.4 Energy Measurement: SLD WISRD	49
4.2 SLAC Large Detector (SLD)	51
4.2.1 Vertex Detector	53
4.2.2 Drift Chamber	58
4.2.3 Cerenkov Ring Imaging Detector (CRID)	59
4.2.4 Liquid Argon Calorimeter.....	61
4.2.5 Warm Iron Calorimeter (WIC).....	71
4.2.6 Luminosity Monitor (LUM).....	72
5 Luminosity Measurement	84
5.1 Measuring Luminosity With Bhabha Scattering.....	84
5.2 Trigger	85
5.3 Event Selection	86
5.4 Classification.....	88
5.5 Accounting.....	89

5.6 Cross Section Calculation.....	91
5.7 Integrated Luminosity Measurement.....	93
5.8 Systematic Errors.....	94
6 Wide-Angle Bhabha Event Selection.....	98
6.1 The Data Acquisition Phase.....	98
6.2 The Pass 1 Filter	101
6.3 The Pass 2 Filter	102
6.4 Wide-Angle Bhabha Event Selection Criteria	103
6.4.1 Cluster Quality Cuts.....	104
6.4.2 Cluster Energy Cuts	108
6.4.3 Angle Dependent Energy Cut.....	111
6.4.4 Global Event Cuts: Total Energy and Energy Imbalance.....	112
6.4.5 Multiplicity Cut	117
6.4.6 Rapidity Cut.....	118
6.4.7 Event Selection Summary	125
6.5 Correction Factors.....	127
6.5.1 Efficiency.....	127
6.5.2 Contamination	132
6.5.3 Summary of Correction Factors.....	133
7 Data Analysis and Results.....	137
7.1 The Extended Maximum Likelihood Method.....	137
7.2 The Likelihood Function for Polarized Bhabha Scattering.....	140
7.3 Fitting the Polarized Bhabha Distribution for \bar{g}_V^e and \bar{g}_A^e	143
7.4 Systematic Errors.....	157
7.4.1 Luminosity Uncertainty	158
7.4.2 Luminosity Asymmetry	159
7.4.3 Polarization Uncertainty.....	160
7.4.4 Center-of-Mass Energy.....	162
7.4.5 Z^0 Mass Uncertainty.....	167
7.4.6 Z^0 Width Uncertainty.....	168
7.4.7 Radiative Correction Model.....	168
7.4.8 Efficiency Correction.....	168
7.4.9 Systematic Error Summary	169
7.5 Final Measurement of \bar{g}_V^e and \bar{g}_A^e	170
7.6 Comparison to the Standard Model.....	170
8 Conclusion	173
Appendix A SLD Collaboration	175
Bibliography	178

LIST OF FIGURES

Figure	Page
2-1	Three Fundamental Vertices of All Electroweak Interactions.....11
2-2	The g_V and g_A Plane Showing Standard Model Predictions and Recent LEP Measurements.....14
2-3	Z^0 Exchange Diagram.....16
3-1	Tree Level Bhabha Scattering Diagrams21
3-2	$\partial_{\cos\theta}\sigma$ for $P_e = -0.7292$ for Each Bhabha Scattering Term.....25
3-3	$\partial_{\cos\theta}\sigma$ for $P_e = +0.7292$ for Each Bhabha Scattering Term.....25
3-4	Overlay of UNIBAB Monte Carlo and Analytical Bhabha Cross Section Expression without Radiative Correction Coefficients.....30
3-5	Overlay of UNIBAB Monte Carlo and Analytical Bhabha Cross Section Expression with Radiative Correction Coefficients.....32
3-6	Wide-Angle Bhabha $\partial_{\cos\theta}\sigma$ vs. $\cos\theta$ for s, t and s-t Terms with and without Radiative Correction Coefficients34
4-1	Schematic View of the SLC.....37
4-2	Schematic View of the SLC Polarized Electron Source.....41
4-3	Energy Level Diagram of the SLC Polarized Electron Source.....43
4-4	SLD Compton Polarimeter47
4-5	Schematic View of the WISRD, the SLC Energy Spectrometers.....49
4-6	Isometric View of the SLD52
4-7	Quadrant View of the SLD53
4-8	VXD2 Schematic View55
4-9	VXD3 Schematic View56
4-10	VXD2 and VXD3 as Viewed in the r- φ Plane57
4-11	VXD2 and VXD3 as Viewed in the r-z Plane.....57

4-12	Schematic View of a Single CRID Module.....	61
4-13	LAC Radiator/Absorber Geometry Showing Lead Sheets and Tiles.....	63
4-14	LAC Barrel Assembly.....	64
4-15	EM and HAD Modules of the LAC.....	66
4-16	LAC Endcap Assembly.....	68
4-17	Endcap LAC Module.....	69
4-18	LUM as Viewed in the r-z Plane.....	74
4-19	LUM Quadrant View Showing Si:W Layers and Electronics	74
4-20	Transverse View of LUM, Pre-1996 (VXD2 Era).....	77
4-21	Transverse View of LUM, Runs 1996 and Later (VXD3 Era)	78
4-22	A Typical Small-Angle Bhabha Event from the 1998 Run	80
6-1	Number of Clusters Distribution for 1994-1995 Run Periods	106
6-2	Number of Clusters Distribution for 1996-1998 Run Periods	107
6-3	Cluster Energy Distributions for Highest Energy Cluster.....	109
6-4	Cluster Energy Distributions for Second Highest Energy Cluster.....	110
6-5	$E_{\text{cluster1}} + E_{\text{cluster2}}$ vs. $ \cos \theta_{\text{Thrust}} $	112
6-6	E_{Total} Distributions for All 1997 Pass 2 Events	115
6-7	$E_{\text{Imbalance}}$ Distribution for All 1997 Pass 2 Events.....	116
6-8	E_{Total} vs. $E_{\text{Imbalance}}$ for All 1997 Pass 2 Events	117
6-9	Cluster Multiplicity Distribution for 1997 Data.....	118
6-10	LAB and center-of-mass (CMS) Angle Definitions.....	121
6-11	Acolinearity vs. $\cos \theta_{\text{CMS}}$ for Three Values of Rapidity	123
6-12	Rapidity Distribution for 1997 Data.....	124
6-13	Average LAC Energy Response as a Function of $ \cos \theta_{\text{Thrust}} $	128
6-14	Efficiency as a Function of $ \cos \theta_{\text{Thrust}} $	132
6-15	$ \cos \theta_{\text{Thrust}} $ Distribution of Corrected WAB Events, 1994 Run	134

6-16	$ \cos \theta_{\text{Thrust}} $ Distribution of Corrected WAB Events, 1995 Run	134
6-17	$ \cos \theta_{\text{Thrust}} $ Distribution of Corrected WAB Events, 1996 Run	135
6-18	$ \cos \theta_{\text{Thrust}} $ Distribution of Corrected WAB Events, 1997 Run	135
6-19	$ \cos \theta_{\text{Thrust}} $ Distribution of Corrected WAB Events, 1998 Run	136
7-1	$\partial_{ \cos \theta_{\text{Thrust}} } N_{\text{WAB}}$ vs. $ \cos \theta_{\text{Thrust}} $ and Residuals for 1994 Left-Handed Fit Results	146
7-2	$\partial_{ \cos \theta_{\text{Thrust}} } N_{\text{WAB}}$ vs. $ \cos \theta_{\text{Thrust}} $ and Residuals for 1994 Right-Handed Fit Results	147
7-3	$\partial_{ \cos \theta_{\text{Thrust}} } N_{\text{WAB}}$ vs. $ \cos \theta_{\text{Thrust}} $ and Residuals for 1995 Left-Handed Fit Results	148
7-4	$\partial_{ \cos \theta_{\text{Thrust}} } N_{\text{WAB}}$ vs. $ \cos \theta_{\text{Thrust}} $ and Residuals for 1995 Right-Handed Fit Results	149
7-5	$\partial_{ \cos \theta_{\text{Thrust}} } N_{\text{WAB}}$ vs. $ \cos \theta_{\text{Thrust}} $ and Residuals for 1996 Left-Handed Fit Results	150
7-6	$\partial_{ \cos \theta_{\text{Thrust}} } N_{\text{WAB}}$ vs. $ \cos \theta_{\text{Thrust}} $ and Residuals for 1996 Right-Handed Fit Results	151
7-7	$\partial_{ \cos \theta_{\text{Thrust}} } N_{\text{WAB}}$ vs. $ \cos \theta_{\text{Thrust}} $ and Residuals for 1997 Left-Handed Fit Results	152
7-8	$\partial_{ \cos \theta_{\text{Thrust}} } N_{\text{WAB}}$ vs. $ \cos \theta_{\text{Thrust}} $ and Residuals for 1997 Right-Handed Fit Results	153
7-9	$\partial_{ \cos \theta_{\text{Thrust}} } N_{\text{WAB}}$ vs. $ \cos \theta_{\text{Thrust}} $ and Residuals for 1998 Left-Handed Fit Results	154
7-10	$\partial_{ \cos \theta_{\text{Thrust}} } N_{\text{WAB}}$ vs. $ \cos \theta_{\text{Thrust}} $ and Residuals for 1998 Right-Handed Fit Results	155
7-11	$\partial_{ \cos \theta_{\text{Thrust}} } \sigma$ vs. $ \cos \theta_{\text{Thrust}} $ of Combined Fit Results Overlaid with 1994-1998 WAB Events.....	156
7-12	E_{cm} vs. \bar{g}_{V}^e and \bar{g}_{A}^e From dMIBA Fit	165
7-13	$A_{\text{LR}}^{e^+e^-}(\cos \theta_{\text{Thrust}})$ vs. $ \cos \theta_{\text{Thrust}} $	171
7-14	Residual Distributions for Figure 7-13	172

LIST OF TABLES

Table	Page
3-1	Relative Contribution of Lowest Order Bhabha Scattering Terms.....24
3-2	Tree Level Bhabha Scattering Parameters.....26
3-3	UNIBAB Input Parameters.....28
3-4	Radiative Correction Coefficients for Born Level Bhabha Scattering.....31
4-1	Polarization Measurements for Each SLD Run Period48
4-2	E_{cm} and E_{cm} Width Measurements for Each SLD Run Period50
4-3	Dead Electronics Channels in LUM Before CDC Wire Break.....82
4-4	Dead Electronics Channels in LUM After CDC Wire Break83
5-1	Effective LUM Bhabhas for Each SLD Run Period.....90
5-2	Number of Precise and Gross LUM Bhabha Events.....90
5-3	Significant SLD Run Blocks.....93
5-4	Total Integrated Luminosity for Each SLD Run Period94
5-5	Luminosity Measurement Systematic Errors.....97
6-1	LAC Tower Thresholds 103
6-2	Effectiveness Summary of WAB Selection Criteria..... 125
6-3	Number of WAB Events for Each SLD Run Period 126
6-4	Angle Dependent Energy Thresholds for Selecting Pseudo Events..... 130
7-1	Maximum Likelihood Fit Results for Each SLD Run Period..... 144
7-2	Number of Unweighted, Weighted and Expected Wide-Angle Bhabha Events for Each SLD Run Period..... 144
7-3	Luminosity Weighted Systematic Errors for \bar{g}_V^e and \bar{g}_A^e 158
7-4	Luminosity Asymmetry as Measured by the LUM..... 160

7-5	\bar{g}_V^e and \bar{g}_A^e Convolved with E_{cm}	166
7-6	\bar{g}_V^e and \bar{g}_A^e Corrections for Finite E_{cm} Width	167

CHAPTER 1 INTRODUCTION

Physics is all about understanding how Nature works. It is the goal of all physicists to discover, through the process of experimental and theoretical discovery, the mathematical equations of motion that completely describe the physical systems of Nature.

While we may be far away from one mathematical equation describing all of Nature, it is nonetheless a prominent and consistent theme throughout the history of physics that our understanding of apparently independent phenomena is continually replaced, through the process of discovery, with a simpler understanding that explains these phenomena as different manifestations of the same thing. From Maxwell's unification of electricity and magnetism in 1864 to the unification of the electromagnetic and weak forces by Glashow, Weinberg and Salam nearly a century later, experimental observation has refined and guided our theories from the complex to the simple.

Our current best theory of the fundamental constituents of Nature at the time the research for this dissertation was performed is known as the Standard Model, which has been spectacularly successful in its ability to describe all experimentally observed phenomena within its predictive domain. Our strategy as present day quantum physicists has been to make precision measurements of the fundamental parameters of the Standard Model in an effort to guide our theories down the path to simplicity.

This dissertation presents the precision measurement of two parameters of the Standard Model, namely the electron's two electroweak coupling parameters to the Z^0 boson. These parameters were measured using the exclusive process of Bhabha scattering,

$e^+e^- \rightarrow e^+e^-$, at a center-of-mass energy on the peak of the Z^0 resonance. We analyzed 43,222 polarized Bhabha scattered events using the SLAC Large Detector (SLD) experiment at the Stanford Linear Accelerator Center (SLAC). The Bhabha scattered events were produced by colliding polarized electrons, with an average polarization of 74%, with unpolarized positrons at an average center-of-mass energy of 91.25 GeV. The SLAC Linear Collider (SLC), the first and so far only e^+e^- linear collider, produced these colliding beams. The data analyzed in this dissertation are from the entire SLD data sample collected between 1994 and 1998.

All Bhabha scattered events within the angular acceptance of the SLD calorimeter subsystems were used in this analysis, including the small-angle events ($28 \text{ mrad.} \leq \theta \leq 68 \text{ mrad.}$) measured by the Silicon/Tungsten Luminosity Monitor (LUM), and wide-angle events ($0 \leq |\cos \theta| \leq 0.9655$) measured by the Liquid Argon Calorimeter (LAC). Using all of the data in this manner allows for the high-precision measurement of the luminosity measured by the LUM to constrain the uncertainty on the electron's two coupling parameters to the Z^0 . We do this by using the Extended Maximum Likelihood Method to perform unbinned fits of all of the polarized wide-angle Bhabha data to the theoretical model of the differential cross section for polarized wide-angle Bhabha scattering. The luminosity measured by the LUM provides the extended term, which greatly reduces the uncertainties of the results.

We note that in contrast with other SLD precision measurements of the effective weak mixing angle ($\sin^2 \theta_w^{\text{eff}}$), which are sensitive to the ratio of the electron's two coupling parameters to the Z^0 , the results of this dissertation independently determine the two coupling parameters.

The outline of this dissertation is as follows. Chapter 2 will describe the theoretical framework of the Standard Model of Electroweak Interactions, with specific attention paid to the physics of producing a Z^0 with e^+e^- collisions at a center-of-mass energy on the peak of the Z^0 resonance, and its subsequent decay. Chapter 3 will focus exclusively on the theory of the Bhabha scattering process $e^+e^- \rightarrow e^+e^-$ when it occurs at a center-of-mass energy on the peak of the Z^0 resonance, including the important effects of the purely quantum mechanical phenomena of the interference between the Z^0 and photon. Also discussed in this chapter are the radiative corrections that contribute to the Bhabha scattering process, a detailed knowledge of which is required to perform the precision measurements presented in this dissertation.

Chapter 4 will describe the SLC and SLD, the experimental apparatus used to collect the data used in this dissertation. Particular attention will be paid to the production and transport of the highly polarized SLC electron beam from the beginning of the SLAC Linear Accelerator to the SLD interaction point. Next, the major subsystems of the SLD will be described, including the polarimetry and beam energy detectors, calorimetry, tracking, and particle identification. We also tabulate the beam polarization and energy measurements for the 1994-1998 run periods since they are essential ingredients of the Extended Maximum Likelihood fits. Particular attention will be paid to the calorimetry subsystems comprised of the LAC and the LUM, since it is the data from these two detector subsystems on which the analysis and results presented in this dissertation are based.

Chapter 5 will present the measurement of the luminosity delivered by the SLC to the SLD for the 1993 through 1998 run periods. The luminosity is measured by the SLD LUM, and its performance, operation and upgrade will be described in some detail as it was

the author's primary responsibility during those run periods, and the final results of this dissertation rely on the precision luminosity measurement provided by the LUM.

Chapter 6 will describe how to find a wide-angle Bhabha event in the SLD data. We describe the entire SLD data-flow by beginning with an individual beam crossing and follow the data through all of the stages until it is reconstructed into physical observables. The selection criteria that separate wide-angle Bhabha events from other Z^0 decay products as well as SLC beam background is described in detail. We describe the importance of understanding the contamination and inefficiencies of our wide-angle Bhabha event sample, and introduce the Pseudo Event Method we invented to correct the event sample for these effects.

Chapter 7 will describe fitting the wide-angle Bhabha event sample from Chapter 6 to the theoretical model of the differential cross section for polarized Bhabha scattering. We build the Probability Distribution Function (p.d.f.) that describes polarized Bhabha scattering piece by piece, and pay careful attention to incorporating the all-important radiative corrections. The final fit results which extract the two electron coupling parameters to the Z^0 from the wide-angle Bhabha data will be presented, along with a detailed analysis and description of the systematic errors which affect the results.

Chapter 8 will conclude with comparisons of the results presented in this dissertation to the results from other experiments.

CHAPTER 2 THE STANDARD MODEL OF ELECTROWEAK INTERACTIONS

This chapter describes the theoretical framework upon which the physics results presented in this dissertation are based. The Standard Model is introduced, including the basic ideas and concepts of the theory as well as the underlying Quantum Physics.

2.1 The SU(2) and U(1) Symmetries

The theory of electroweak interactions as developed by Glashow, Weinberg and Salam[1-3], hereafter called the GWS theory, asserts that electroweak interactions are described by a gauge invariant Lagrangian with respect to two internal symmetries¹. The GWS theory assigns every fundamental particle two internal quantum numbers. The two symmetries are described by the mathematical group $SU(2)_L \otimes U(1)_Y$. The notation for the SU(2) and U(1) groups simply represent the standard mathematical groups from Group Theory, while the adornments consisting of the subscripts L and Y simply give a physics context to the group theory symbols which will be described below.

The GWS theory asserts that all particles carry a quantum number called *weak isospin* that assigns them to membership in either a SU(2) singlet or a SU(2) doublet based on the particle's helicity. Left-handed particles are assigned to a SU(2) doublet and right-handed particles are assigned to a SU(2) singlet. This distinction based on a particle's helicity is what

¹ There are a total of three internal symmetries in the full Standard Model, but here we only consider the two that give rise to the electromagnetic and weak interactions. The third internal symmetry based on SU(3) gives rise to the strong force.

gives rise to parity violation, which is the fundamental experimental signature of weak interactions and will be described further below.

The Lagrangian describing the interactions of these particles is invariant to arbitrary rotations of particles in the $SU(2)_L$ weak isospin space. The gauge bosons required by the invariance are the generators of the $SU(2)_L$ group, which are three massless spin-1 fields (i.e. quantum mechanical wave functions) W_μ^i , $i = 1, 2, 3$ and form a weak isospin triplet. These three massless vector bosons mediate the weak force, with a coupling strength g_w , between particles with weak isospin. The L in $SU(2)_L$ means that these bosons only couple to left-handed fields (i.e. to the members of the $SU(2)$ doublet); right-handed fields (the members of the $SU(2)$ singlet) are invisible to this weak force. Stated another way, the weak force maximally violates parity.

The GWS theory also asserts that all particles carry a quantum number called *hypercharge*, and that the electroweak Lagrangian is invariant to arbitrary rotations of particles in the $U(1)_Y$ hypercharge space. The gauge boson required by the invariance is the generator of the $U(1)_Y$ group, which is a massless spin-1 field B_μ and forms a *weak hypercharge* singlet. This massless vector field couples with strength g_Y to particles that have weak hypercharge. The Y in $U(1)_Y$ stands for hypercharge.

2.2 The Matter Content

The matter content of the Standard Model consists of a family of four spin- $\frac{1}{2}$ fermion fields that is replicated three times.

$$\begin{array}{ccc}
\text{weak isospin } T_3 & \text{leptons} & \text{quarks} \\
+\frac{1}{2} & \begin{pmatrix} \nu_i \\ l_i \end{pmatrix}_L & \begin{pmatrix} u_i \\ d'_i \end{pmatrix}_L \\
-\frac{1}{2} & & \\
0 & (\nu_i)_R \quad (l_i)_R & (u_i)_R \quad (d'_i)_R
\end{array}, i = 1, 2, 3 \quad (2.1)$$

Expression (2.1) groups the left-handed fermions of each family into $SU(2)_L$ doublets and right-handed fermions into $SU(2)_L$ singlets based on T_3 , the third component of weak isospin. All fermions have been directly observed experimentally, a relatively recent development with the discovery of the top quark[4] and direct observation of ν_τ [5].

The leptons have integer electric charge and couple to the *electroweak force*. The ν_i are called neutrinos and have electric charge $Q = 0$ and small but non-negligible mass². Although they are not a part of the Standard Model, the right-handed neutrinos (the $SU(2)_L$ singlets $(\nu_i)_R$ in expression (2.1)) are listed for completeness: right-handed neutrinos have neither electromagnetic interactions (since $Q = 0$) nor weak interactions (since $T_3 = 0$). The l_i have electric charge $Q = -1$ and are massive. Each lepton $SU(2)_L$ doublet has $Y = -1$ and each charged lepton $SU(2)_L$ singlet has $Y = -2$. The names of the leptons are $(l_1, l_2, l_3) \equiv (e^-, \mu^-, \tau^-) \equiv (\text{electron, muon, tau})$ and $(\nu_1, \nu_2, \nu_3) \equiv (\nu_e, \nu_\mu, \nu_\tau)$. The formula relating electric charge (Q in units of e), third component of isospin (T_3) and hypercharge (Y), is

$$Q = T_3 + \frac{1}{2} Y \quad (2.2)$$

The quarks have fractional electric charge and couple to the *color force* (or *strong force*) in addition to the electroweak force. The u_i have fractional electric charge $Q = +\frac{2}{3}$, and the

² The experimental evidence for neutrino oscillations[6] conclusively demonstrates that neutrinos have mass, where the neutrino's weak eigenstates are linear combination of its mass eigenstates. However, neutrino oscillation experiments are only sensitive to the mass differences between different neutrino species and not to the absolute value of any one neutrino's mass.

d' have fractional electric charge $Q = -\frac{1}{3}$. Each quark $SU(2)_L$ doublet has $Y = +\frac{1}{3}$ while the $SU(2)_L$ singlets $(u_i)_R$ and $(d')_R$ have hypercharge $Y = +\frac{4}{3}$ and $Y = -\frac{2}{3}$, respectively. The names of the quarks are $(u_1, u_2, u_3) \equiv (u, c, t) \equiv (\text{up, charm, top})$ and $(d'_1, d'_2, d'_3) \equiv (d, s, b) \equiv (\text{down, strange, bottom})$.

The weak eigenstates d'_i are linear combinations of the three mass eigenstates d_i (i.e. the energy levels of the system), where $d'_i \equiv \sum_j V_{ij} d_j$ and V_{ij} is a unitary matrix called the Cabibbo-Kobayashi-Maskawa (CKM) mixing matrix. Since it is unitary, the nine elements of V_{ij} are not all independent and are reduced to three angles and one phase $(\theta_1, \theta_2, \theta_3, \delta)_{\text{CKM}}$. The Standard Model does not specify how the weak eigenstates d'_i are related to the mass eigenstates d_i , and therefore the $(\theta_1, \theta_2, \theta_3, \delta)_{\text{CKM}}$ must be determined experimentally. The phase δ is responsible for the breaking of CP symmetry in the Standard Model (so-called CP violation).

The Standard Model does not explain why there is more than one family, so the number of families must be determined experimentally which is currently measured to be three. Each of the three families is identical except for the individual particle masses that must also be determined experimentally. Other than using the masses for the kinematics and phase space calculations, the dynamics of the GWS theory are identical for each family.

2.3 The Physical Bosons: W^\pm , Z^0 and Photon

Experimentally, the four massless bosons $W_1^\mu, W_2^\mu, W_3^\mu$ and B^μ introduced in section 2.1 above do not exist. Instead there exists two massive electrically charged physical bosons W^\pm with mass 80.423 ± 0.039 GeV [7, p. 85], the massive boson Z^0 with mass 91.1876 ± 0.0021 GeV [7, p. 7], and the massless photon γ .

The four massless bosons are transformed to three massive and one massless boson when the symmetry of the ground state of the electroweak Lagrangian is broken³ (a process also known as *Spontaneous Symmetry Breaking*). One way to incorporate this into the Standard Model is by asserting that a spin-0 field that only couples to the electroweak force permeates the universe. This field, called the Higgs field, is a weak SU(2)_L doublet, has non-zero U(1)_Y hypercharge, and is a color singlet SU(3)_C (i.e. it has no strong interactions). The addition of the Higgs field to the Standard Model is called the *Minimal Standard Model* (or MSM for short)⁴. In the MSM the two states of the SU(2)_L doublet Higgs field is composed of two complex scalar fields $\phi^+(x) = \frac{1}{\sqrt{2}}(\phi_1(x) + i\phi_2(x))$ and $\phi^0(x) = \frac{1}{\sqrt{2}}(\phi_3(x) + i\phi_4(x))$, and a specific choice of the Higgs field ground state is chosen which obviously breaks the SU(2)_L symmetry:

$$\phi(x) = \begin{pmatrix} \phi(x)^+ \\ \phi(x)^0 \end{pmatrix} \xrightarrow[\text{symmetry breaking}]{\text{spontaneous}} \phi_{\text{ground state}}(x) = \begin{pmatrix} 0 \\ v + H(x) + \dots \end{pmatrix} \quad (2.3)$$

By choosing a specific rotation in the SU(2)_L space we have broken three local symmetries and caused three massless spin-0 bosons to disappear, which reappear as the longitudinal polarization states of three (and hence now massive) bosons which are a linear combination of the original electroweak massless bosons $W_1^\mu, W_2^\mu, W_3^\mu$ and B^μ . Written more suggestively as a mixing matrix between the SU(2)_L and U(1)_Y spaces:

³ The gauge symmetry of the Lagrangian itself is preserved, which it must be. It is only the ground state of the system that is no longer symmetric.

⁴ We call it minimal because it is the simplest, most straight-forward way of adding Spontaneous Symmetry Breaking to the Standard Model, which is necessary for the theory to give the W^\pm and Z^0 mass related by $M_{W^\pm} = M_{Z^0} \cos \theta_W$. Spontaneous Symmetry Breaking could result from the Standard Model spin-0 Higgs field, or other alternative fields.

$$\begin{pmatrix} A_\mu \\ Z_\mu^0 \end{pmatrix} = \begin{pmatrix} \cos \theta_W & \sin \theta_W \\ -\sin \theta_W & \cos \theta_W \end{pmatrix} \begin{pmatrix} B_\mu \\ W_\mu^3 \end{pmatrix} \quad (2.4)$$

The angle $\theta_W \equiv \tan^{-1} \left(\frac{g_Y}{g_W} \right)$ in equation (2.4) is called the *weak mixing angle* or *Weinberg angle*, and specifies the mixture of the gauge fields W_μ and B_μ in the two physical fields A_μ and Z_μ , where g_W and g_Y are the couplings of the gauge fields W_μ and B_μ , respectively. The field A_μ is just the vector potential from electromagnetism and represents the photon. The Standard Model does not predict a value for θ_W , so its value must be determined experimentally.

2.4 The Electroweak Lagrangian of the Standard Model

The formalism and definitions presented up to this point allow us to write the full electroweak Lagrangian that describes all interactions between the fermions and the four gauge bosons as follows:

$$\begin{aligned} \mathcal{L}_{\text{fermion}} = & \sum_i \bar{\psi}_i \left(i \not{\partial} - m_i - \frac{g_W m_i H}{2M_{W^\pm}} \right) \psi_i \\ & - e \sum_i Q_i \bar{\psi}_i \gamma^\mu \psi_i A_\mu \\ & - \frac{g_W}{2\sqrt{2}} \sum_i \bar{\psi}_i \gamma^\mu (1 - \gamma^5) (T^{++} W_\mu^+ + T^{--} W_\mu^-) \psi_i \\ & - \frac{g_W}{2\cos\theta_W} \sum_i \bar{\psi}_i \gamma^\mu (g_V^i - g_A^i \gamma^5) \psi_i Z_\mu^0 \end{aligned} \quad (2.5)$$

Equation (2.5) is the Lagrangian of the Minimal Standard Model of Electroweak Interactions and contains the physics of all of electrodynamics and of all weak interactions. The ψ_i are the fermion wave functions. The coupling strengths are not all independent and are related by

$$g_w = \frac{e}{\sin \theta_w} \quad (2.6)$$

The vertex factors for each of the interactions are shown in Figure 2-1.

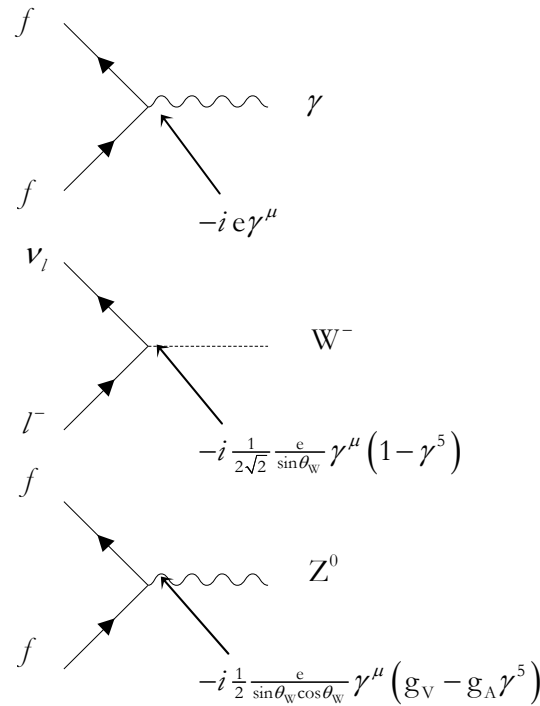


Figure 2-1 The three fundamental vertices of all electroweak interactions. The symbol f represents any fermion or anti-fermion \bar{f} . The middle diagram, which shows a charged lepton l^- and its associated neutrino ν_l coupling to a W^- , is representative of all of the weak charged currents. In principle the boson can be either W^- or W^+ and the fermions can be any $SU(2)_L$ doublet.

The first term of equation (2.5) contains the kinetic energy and Higgs potential. The massive spin-0 boson H , the Higgs boson, has not been seen experimentally. However, if in

fact the Higgs boson exists then limits can be put on its mass via the radiative corrections to some observables (see section 2.6 below).

The second term is the familiar Lagrangian of electrodynamics, and its parity conserving nature can be seen explicitly due to the vector nature of the vertex factor $i e \gamma^\mu$ (i.e. $\bar{\psi}_i \gamma^\mu \psi_i$ transforms as a vector). Another way to say this is that the photon couples to left-handed fermions with the same coupling-strength as it does to right-handed fermions.

The third term in equation (2.5) describes the weak charged current. The T^\pm are the $SU(2)_L$ raising and lowering operators that, for example, transform an electron e^- to a ν_e by emission of a W^- (or absorption of a W^+). The parity violating nature of this weak current can be seen explicitly in the vertex factor $-i \frac{1}{2\sqrt{2}} \frac{e}{\sin\theta_w} \gamma^\mu (1 - \gamma^5)$, since $\bar{\psi}_i \gamma^\mu \psi_i$ transforms as a vector while $\bar{\psi}_i \gamma^\mu \gamma^5 \psi_i$ transforms as an axial-vector, and adding a vector to an axial-vector will obviously violate parity. This particular combination violates parity maximally since γ^5 is the helicity operator, meaning that $\gamma^5 \psi = \pm 1 \psi$ (+1 for right-handed states, -1 for left-handed states), so $\frac{1}{2}(1 - \gamma^5) \psi_R = \frac{1}{2}(1 - 1) \psi_R = 0$ for right-handed states and $\frac{1}{2}(1 - \gamma^5) \psi_L = \frac{1}{2}(1 + 1) \psi_L = \psi_L$. This interaction is called pure V-A (read “pure V minus A” or “pure vector minus axial-vector”).

The last term in equation (2.5) describes the neutral weak current mediated by the Z^0 boson. The parity violating nature of this neutral current can also be seen explicitly from its vertex factor $-i \frac{1}{2} \frac{e}{\sin\theta_w \cos\theta_w} \gamma^\mu (g_V - g_A \gamma^5)$, which is similar to the vertex factor for the weak charged current except that the vector and axial-vector components are no longer maximally mixed. Instead the interaction is g_V parts vector and g_A parts axial-vector. The couplings g_V and g_A for Standard Model particles are:

$$\begin{aligned} g_V &\equiv T_3 - 2Q \sin^2 \theta_w \\ g_A &\equiv T_3 \end{aligned} \tag{2.7}$$

Where T_3 is the third component of weak isospin ($\pm \frac{1}{2}$ for the $SU(2)_L$ doublets, 0 for the $SU(2)_L$ singlet) and Q is the electric charge in units of the electron's charge.

The two parameters g_V and g_A can also be expressed in terms of the left and right-handed couplings g_L and g_R :

$$\begin{aligned} g_V &= \frac{1}{2}(g_L + g_R) \\ g_A &= \frac{1}{2}(g_L - g_R) \end{aligned} \tag{2.8}$$

Figure 2-2 shows the g_V and g_A plane with Standard Model predictions for the couplings (the shaded chevron in the center of the plot) along with 68% confidence limit contours from LEP experiments for the lepton couplings to the Z^0 .

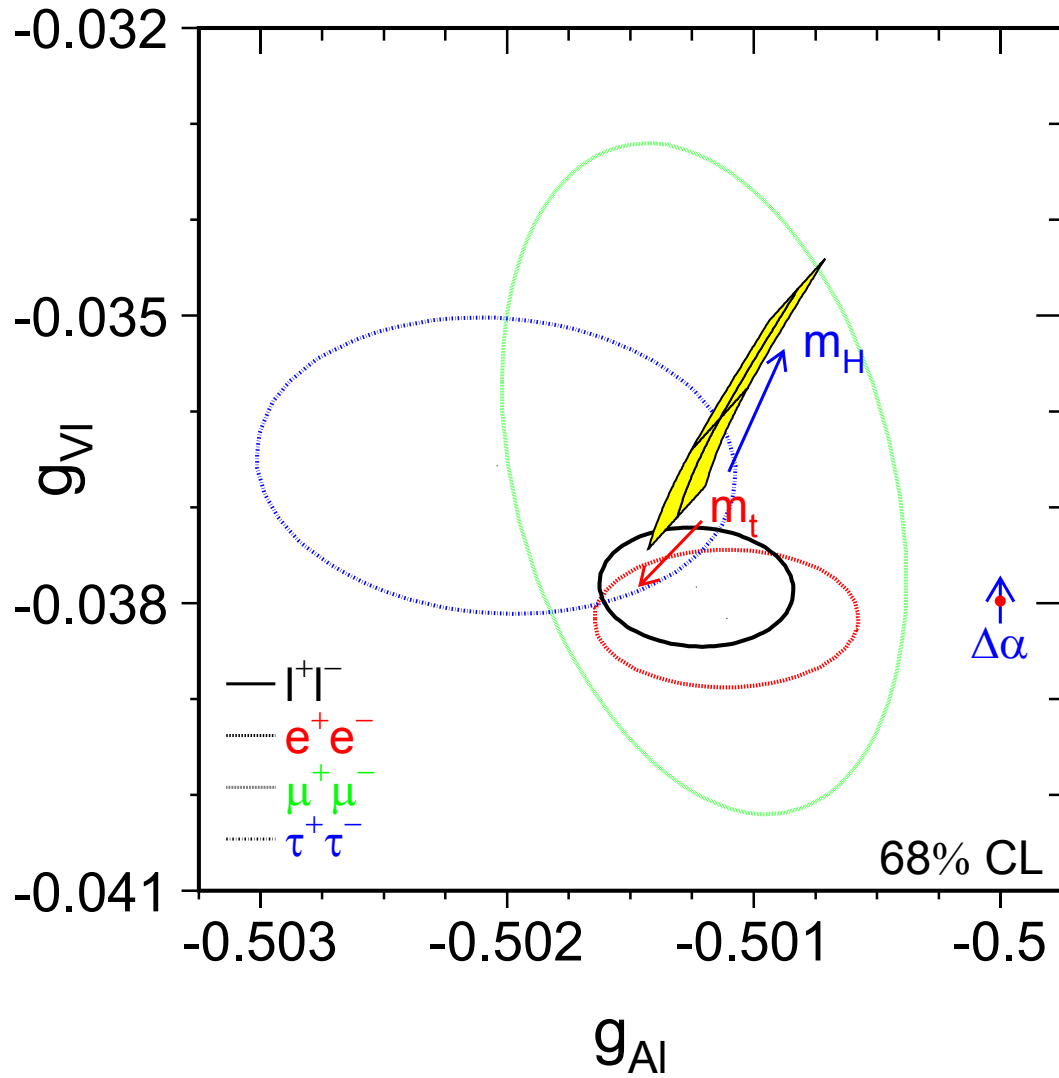


Figure 2-2 The g_V and g_A plane showing Standard Model predictions (the yellow chevron in the center) along with 68% confidence limit contours from LEP experiments for the lepton couplings to the Z^0 . The plot is courtesy of the LEP Electroweak Working Group and comes from Figure 12.2 in [7].

2.5 Standard Model Parameters

The Standard Model Lagrangian in equation (2.5) depends on free parameters that must be measured by experiment. These parameters boil down to a coupling constant for each of the four gauge bosons, the boson masses (M_{W^\pm} , M_{Z^0} and the Higgs mass M_H) and fermion masses (three charged lepton masses and six quark masses), and the CKM quark mixing matrix (three angles and one phase). However, within the theory many of these parameters are related by the weak mixing angle θ_W . For example, the coupling constants are completely specified by the electromagnetic coupling constant e (i.e. the electron's charge) and the weak mixing angle θ_W according to equation (2.6). Additionally, the masses of the W^\pm and Z^0 bosons are related by

$$M_{W^\pm} = M_{Z^0} \cos \theta_W \quad (2.9)$$

In practice those quantities which are the most precisely measured are used to do calculations with the Standard Model, which are currently the fine structure constant⁵ $\alpha = (137.03599976(50))^{-1}$ [8, p. 77], the Fermi constant $G_F = 1.16639(1) \times 10^{-5}$ [8, p. 77] and $\sin^2 \theta_W = 0.23097 \pm 0.00027$ [9].

To lowest order in perturbation theory, the mass of the W^\pm bosons can be directly calculated:

$$M_{W^\pm} = \frac{1}{\sin \theta_W} \sqrt{\frac{\pi \alpha}{\sqrt{2} G_F}} \quad (2.10)$$

⁵ The Fine Structure Constant quoted here is for low momentum transfer, $\alpha(q^2 = 0) \approx \frac{1}{137}$. This stands in contrast to $\alpha(q^2 = M_{Z^0}^2) \approx \frac{1}{128}$. We call α a running coupling constant since its value runs with q^2 .

The earliest measurements of θ_w [10] pointed experimentalists to the discovery of the W^\pm bosons [11] and Z^0 boson [12] at the masses predicted by equations (2.9) and (2.10). This discovery was an overwhelming confirmation of the GWS theory.

2.6 Radiative Corrections

All physical processes mediated by the electroweak force are made simply by combining the three fundamental vertices shown in Figure 2-1. The simplest combinations are called *tree level* or *Born level* diagrams and involves combining just two vertices. For example, the diagram for an electron and positron exchanging a Z^0 is shown in Figure 2-3.

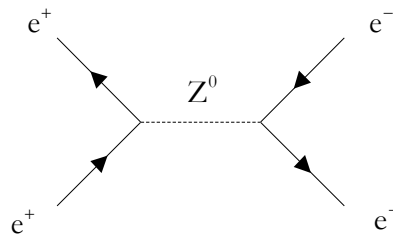


Figure 2-3 Z^0 exchange. Putting two fundamental vertices together from Figure 2-1 creates the tree level diagram of an electron and positron exchanging a Z^0 .

However, any diagram that can be drawn will occur in nature, which means that fundamental processes such as the Z^0 exchange shown in Figure 2-3 occur in addition to an infinite number of other diagrams. This is dealt with using perturbation theory because of the smallness of the coupling parameter at each vertex (i.e. $\alpha \ll 1$), and all diagrams other than the tree level diagram are said to *modify* the tree level diagram since their contributions

are small relative to the tree level diagram. All of these higher order diagrams fall under the general category called *radiative corrections*.

Although the radiative corrections are small compared to the tree level diagrams, their effects on observables are non-negligible and require a careful, thorough understanding. Practically this is done by choosing a *renormalization scheme* whereby one defines the *bare* input parameters to the theory and a set of renormalization equations that are used to relate them to experimentally accessible parameters.

There are generally two broad classes of radiative corrections: photonic and non-photonic corrections. By far the largest correction at momentum transfers near the Z^0 resonance are the photonic correction consisting of initial and final state photon radiation. The Initial State Radiation (ISR) reduces the Bhabha cross section at the Z^0 pole by about 30%. The largest of the non-photonic corrections are the Z^0 and photon self-energies (the literature also calls these vacuum polarization corrections, oblique corrections, and propagator corrections) which account for cross section corrections at the level of $\leq 10\%$. The Weak and QED Vertex corrections are the next largest and account for cross section corrections at the level of $\leq 1\%$ but have no $\cos\theta$ dependence. Finally, the Weak box corrections are the smallest, being very small near the Z^0 -peak due to their non-resonant structure. The Weak box corrections account for cross section corrections at the level of $\leq 0.02\%$, although their size does depend on $\cos\theta$.

2.7 Tests of the Standard Model

Tests of the Standard Model involve experimentally measuring the parameters of the theory (see section 2.5) and comparing the measurements to Standard Model predictions.

Chapter 7 describes our measurement of \bar{g}_V^e and \bar{g}_A^e , the *effective* vector and axial-vector coupling parameters of the electron to the Z^0 . We call them effective parameters because they are the quantities accessible by experiment, and are measured at a center-of-mass energy $\sqrt{s} = M_Z$. The bar over these quantities means *effective*, and serves to distinguish them from the purely theoretical values of g_V and g_A appearing in equation (2.7). The superscript e emphasizes that it is the electron coupling to the Z^0 that is measured (as opposed to some other fermion coupling to the Z^0).

The effective weak mixing angle θ_W^{eff} may also be expressed in terms of \bar{g}_V^e and \bar{g}_A^e using equation (2.7):

$$\sin^2 \theta_W^{\text{eff}} = \frac{1}{4} \left(1 - \frac{\bar{g}_V^e}{\bar{g}_A^e} \right) \quad (2.11)$$

Another particularly simple way to measure the extent of parity violation for the fermion vertex $Z^0 \rightarrow f \bar{f}$ is to measure the asymmetry parameter A_f [13, 14] defined as

$$A_f \equiv \frac{g_L^2 - g_R^2}{g_L^2 + g_R^2} = \frac{2g_V g_A}{g_V^2 + g_A^2} = \frac{2(1 - 4\sin^2 \theta_W)}{1 + (1 - 4\sin^2 \theta_W)^2} \quad (2.12)$$

The simplest of the asymmetry parameters to measure is A_e due to its relation to the left-right cross section asymmetry A_{LR} :

$$A_e = A_{\text{LR}} \equiv \frac{\sigma_L - \sigma_R}{\sigma_L + \sigma_R} \quad (2.13)$$

where σ_L and σ_R are the total integrated cross sections for $e^+e_{L,R}^- \rightarrow Z^0$ for initial state left-handed (L) and right-handed (R) electrons. Measuring A_{LR} is a particularly simple, robust and high precision measurement of A_e since all final states from the Z^0 decay are used with the exception of the e^+e^- final state⁶, all angular dependence and all dependence on the final state cancel, and the measurement does not require knowledge of detector efficiency or acceptance.

Since the number of events N for any physics process described by the cross section σ is related to the integrated luminosity $\mathcal{L}_{\text{Integrated}}$ by the relation $N = \mathcal{L}_{\text{Integrated}} \sigma$, measuring A_{LR} turns into a simple number counting experiment provided that both left-handed and right-handed luminosities are equal. Experimentally, longitudinally polarized beams of left and right-handed electrons are collided with unpolarized positrons to create polarized Z^0 bosons, and the number of Z^0 decays are counted for each helicity to measure A_{LR} . However, in practice the electron beams are not 100% polarized but instead have a polarization $P_e < 1$, so that the measurement of A_{LR} is given by the equation:

$$A_{LR} = \frac{1}{P_e} \frac{N_L - N_R}{N_L + N_R} \quad (2.14)$$

where N_L and N_R are the number of Z^0 decays produced by left and right-handed beams, respectively.

⁶ The e^+e^- final state is excluded from the measurement of A_{LR} because of the asymmetry dilution due to the t-channel photon contribution to the cross section.

CHAPTER 3 BHABHA SCATTERING

Precision measurements of the properties of the Z^0 boson are best studied in the relatively clean environment of electron-positron colliders. Therefore, the coupling of the electron to the Z^0 at the production vertex $e^+e^- \rightarrow Z^0$ is a critical measurement. For example, knowledge of the coupling of the Z^0 to the electron allows one to extract the coupling of the Z^0 to other fermions in the process $e^+e^- \rightarrow Z^0 \rightarrow f\bar{f}$, where f is any fermion from equation (2.1).

The process where both the initial state and final state particles are an electron and positron, $e^+e^- \rightarrow e^+e^-$, is called Bhabha scattering[15]. All electron-positron colliders use Bhabha scattering to determine the luminosity delivered by the accelerator to the experiment. The reason for this is due to the extremely large cross section of the process $e^+e^- \rightarrow e^+e^-$ at small angles ($\theta < 70\text{mrad.}$) which provides a small statistical error, and the theoretical precision and accuracy of which this cross section is known, which provides a small systematic error. Since the Bhabha scattering at these small angles is almost purely described by Quantum Electrodynamics (QED), the cross section can be calculated to great precision. This chapter will describe all of this in more detail.

Bhabha scattering was historically only concerned with the exchange of photons between electrons and positrons. These photons could be exchanged between the electron and positron through either the s-channel annihilation diagram or the t-channel radiation diagram. However, at higher energy the role of the Z^0 boson must also be included.

This chapter will provide a detailed description of the Bhabha Scattering process with particular attention paid to the rich physics that occurs when the Bhabha scattering process occurs at a center-of-mass energy near the Z^0 resonance of about 91 GeV. It will be shown that although a Born-level treatment of Bhabha scattering is enough to grasp the essential physics involved in Bhabha scattering, a detailed knowledge of radiative corrections, is essential to make precision measurements of the Z^0 parameters.

3.1 Analytical Expression for the Bhabha Differential Cross Section

The s-channel and t-channel diagrams describing the differential cross section for $e^+e_{L,R}^- \rightarrow Z^0 \rightarrow e^+e^-$ and $e^+e_{L,R}^- \rightarrow \gamma \rightarrow e^+e^-$ in shown in Figure 3-1.

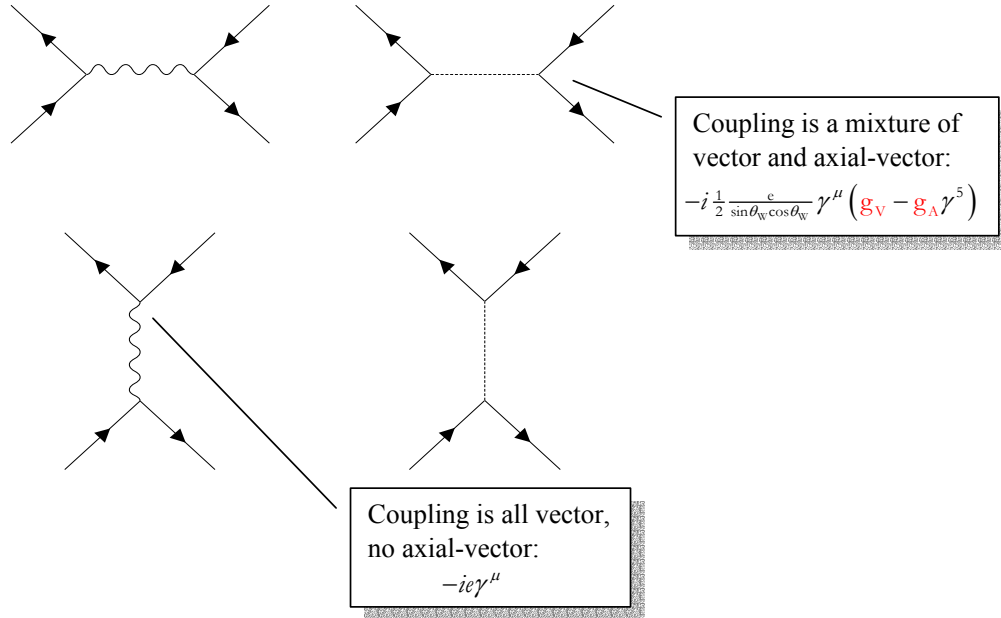


Figure 3-1 Tree level diagrams for the process $e^+e_{L,R}^- \rightarrow Z^0 \rightarrow e^+e^-$ and $e^+e_{L,R}^- \rightarrow \gamma \rightarrow e^+e^-$. The two upper figures are the s-channel annihilation diagrams, while the two lower figures are the t-channel exchange diagrams.

When written out mathematically using the Feynman calculus these diagrams give 10 terms to lowest order; three terms representing pure photon exchange, three terms representing pure Z^0 exchange, and 4 terms representing the interference between the photon and Z^0 . These 10 terms were calculated in [16] to include electron polarization, and are listed below in equations (3.1) through (3.10) in decreasing order of the size of their relative contribution to the total integrated cross section.

$$\begin{aligned} \frac{\partial}{\partial x} \sigma_{Z(s)Z(s)} = & \frac{\pi\alpha^2}{2s(\sin^2 2\theta_w)^2} \frac{s^2}{(s-M_Z^2)^2 + \frac{s^2}{M_Z^2} \Gamma_Z^2} \times \\ & (g_A^2 + g_V^2)^2 \left(\frac{4g_A g_V \left(\frac{2g_A g_V}{g_A^2 + g_V^2} + P_e \right) x}{g_A^2 + g_V^2} + \left(1 + \frac{2g_A g_V}{g_A^2 + g_V^2} P_e \right) (1+x^2) \right) \end{aligned} \quad (3.1)$$

$$\frac{\partial}{\partial x} \sigma_{\gamma(t)\gamma(t)} = \frac{\pi\alpha^2}{2s} 2 \frac{4+(1+x)^2}{(x-1)^2} \quad (3.2)$$

$$\frac{\partial}{\partial x} \sigma_{Z(s)\gamma(t)} = \frac{\pi\alpha^2}{2s \sin^2 2\theta_w} 2 \frac{s(s-M_Z^2)}{(s-M_Z^2)^2 + \frac{s^2}{M_Z^2} \Gamma_Z^2} \frac{g_V^2 \left(1 + 2 \frac{g_A}{g_V} P_e + \frac{g_A^2}{g_V^2} \right) (1+x)^2}{(x-1)} \quad (3.3)$$

$$\frac{\partial}{\partial x} \sigma_{\gamma(s)\gamma(t)} = \frac{\pi\alpha^2}{2s} 2 \frac{(1+x)^2}{x-1} \quad (3.4)$$

$$\frac{\partial}{\partial x} \sigma_{\gamma(s)\gamma(s)} = \frac{\pi\alpha^2}{2s} (1+x^2) \quad (3.5)$$

$$\frac{\partial}{\partial x} \sigma_{Z(t)\gamma(t)} = \frac{\pi\alpha^2}{2s \sin^2 2\theta_w} 2 \frac{s(t - M_Z^2)}{(t - M_Z^2)^2 + \frac{s^2}{M_Z^2} \Gamma_Z^2} \times$$

$$\frac{g_V^2 \left(4 \left(1 - \frac{g_A^2}{g_V^2} \right) + \left(1 + 2 \frac{g_A}{g_V} P_e + \frac{g_A^2}{g_V^2} \right) (1+x)^2 \right)}{x-1} \quad (3.6)$$

$$\frac{\partial}{\partial x} \sigma_{Z(t)\gamma(s)} = \frac{\pi\alpha^2}{2s \sin^2 2\theta_w} \frac{s(t - M_Z^2)}{(t - M_Z^2)^2 + \frac{s^2}{M_Z^2} \Gamma_Z^2} g_V^2 \left(1 + 2 \frac{g_A}{g_V} P_e + \frac{g_A^2}{g_V^2} \right) (1+x)^2 \quad (3.7)$$

$$\frac{\partial}{\partial x} \sigma_{Z(s)Z(t)} = \frac{\pi\alpha^2}{2s (\sin^2 2\theta_w)^2} \frac{s^2 \left((s - M_Z^2)(t - M_Z^2) + \frac{s^2}{M_Z^2} \Gamma_Z^2 \right)}{\left((s - M_Z^2)(t - M_Z^2) + \frac{s^2}{M_Z^2} \Gamma_Z^2 \right)^2 + \frac{s^2}{M_Z^2} \Gamma_Z^2 (t-s)^2} \times$$

$$(g_A^2 + g_V^2)^2 \left(1 + \frac{4g_A g_V}{g_A^2 + g_V^2} P_e + \frac{4g_A^2 g_V^2}{(g_A^2 + g_V^2)^2} \right) (1+x)^2 \quad (3.8)$$

$$\frac{\partial}{\partial x} \sigma_{Z(s)\gamma(s)} = \frac{\pi\alpha^2}{2s \sin^2 2\theta_w} 2 \frac{s(s - M_Z^2)}{(s - M_Z^2)^2 + \frac{s^2}{M_Z^2} \Gamma_Z^2} \times$$

$$g_V^2 \left(\frac{2g_A \left(\frac{g_A}{g_V} + P_e \right) x}{g_V} + \left(1 + \frac{g_A}{g_V} P_e \right) (1+x^2) \right) \quad (3.9)$$

$$\frac{\partial}{\partial x} \sigma_{Z(t)Z(t)} = \frac{\pi\alpha^2}{2s (\sin^2 2\theta_w)^2} \frac{1}{2} \frac{s^2}{(t - M_Z^2)^2 + \frac{s^2}{M_Z^2} \Gamma_Z^2} \times \frac{1}{2} (g_A^2 + g_V^2)^2 \times$$

$$\left(4 \left(1 - \frac{4g_A^2 g_V^2}{(g_A^2 + g_V^2)^2} \right) + \left(1 + \frac{4g_A g_V}{g_A^2 + g_V^2} P_e + \frac{4g_A^2 g_V^2}{(g_A^2 + g_V^2)^2} \right) (1+x)^2 \right) \quad (3.10)$$

The size of the relative contribution to the total cross section for each of these 10 terms is given in Table 3-1 for two values of the initial state e^- polarization $P_e = \pm 0.7292$, where positive values of P_e correspond to right-handed electrons, and negative values of P_e

correspond to left-handed electrons. Each of the 10 terms was integrated over the range $|\cos \theta| < 0.9655$, which is the angular acceptance used in the data analysis presented in Chapter 7.

Table 3-1 Size of the relative contribution to the total cross section for each of the 10 terms given in equations (3.1) through (3.10) for two values of initial e^- polarization P_e . The cross section is integrated over the range $|\cos \theta| < 0.9655$. The table is sorted by the data in the column for $P_e = -0.7292$.

Term	Relative size	
	$P_e = -0.7292$ (left-handed)	$P_e = +0.7292$ (right-handed)
$\sigma_{Z(s)Z(s)}$	51.06%	45.71%
$\sigma_{\gamma(t)\gamma(t)}$	43.82%	48.97%
$\sigma_{Z(s)\gamma(t)}$	2.31%	2.06%
$\sigma_{\gamma(s)\gamma(t)}$	2.13%	2.38%
$\sigma_{\gamma(s)\gamma(s)}$	0.26%	0.29%
$\sigma_{Z(t)\gamma(t)}$	0.22%	0.42%
$\sigma_{Z(t)\gamma(s)}$	0.09%	0.08%
$\sigma_{Z(s)Z(t)}$	0.06%	0.05%
$\sigma_{Z(s)\gamma(s)}$	0.03%	0.03%
$\sigma_{Z(t)Z(t)}$	0.02%	0.02%

The $\cos \theta$ dependence of each term is shown in Figure 3-2 for left-handed electrons and Figure 3-3 for right-handed electrons.

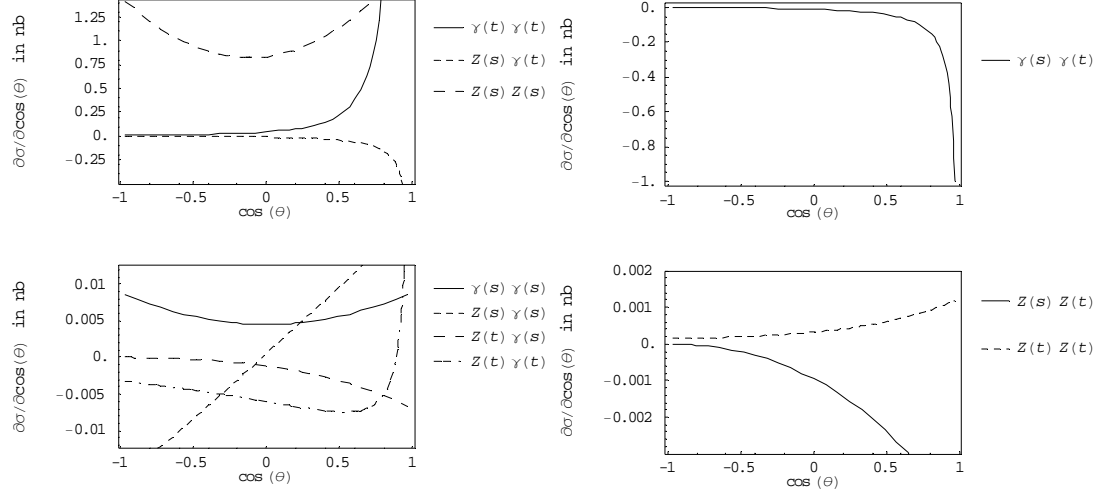


Figure 3-2 $\partial_{\cos\theta}\sigma$ for $P_e = -0.7292$ (which corresponds to left-handed electrons) for each of the 10 lowest order Bhabha scattering terms given by equations (3.1) through (3.10). The values used for the 10 parameters in these equations to generate the plots are given in Table 3-2, as well as $\bar{g}_V^e = -0.03816$ and $\bar{g}_A^e = -0.50111$.

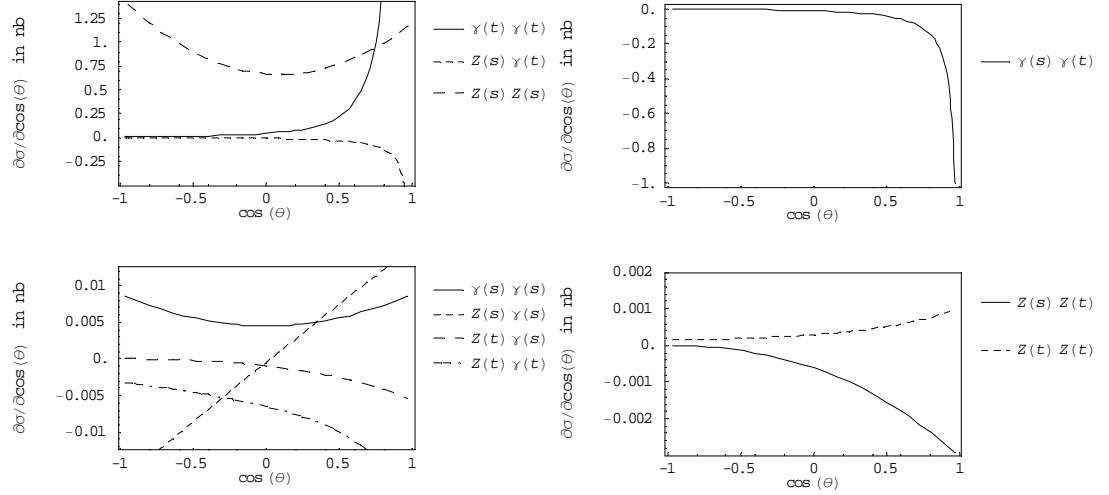


Figure 3-3 $\partial_{\cos\theta}\sigma$ for $P_e = +0.7292$ (which corresponds to right-handed electrons) for each of the 10 lowest order Bhabha scattering terms given by equations (3.1) through (3.10). The values used for the 10 parameters in these equations to generate the plots are given in Table 3-2, as well as $\bar{g}_V^e = -0.03816$ and $\bar{g}_A^e = -0.50111$.

The complete expression (the sum of all 10 terms) has 10 parameters, which are listed in Table 3-2.

Table 3-2 Parameters appearing in the tree level expression of Bhabha scattering at the Z^0 resonance given in equations (3.1) through (3.10).

Symbol	Name	Value
$\alpha(q^2 = M_{Z^0}^2)$	Fine Structure Constant	$\approx 1/128$
$\sin^2 \theta_W$	Effective Weak Mixing Angle[17]	0.23097 ± 0.00027
M_Z	Z^0 mass[7]	$91.1876 \pm 0.0021 \text{ GeV}$
Γ_Z	Z^0 width[7]	$2.4952 \pm 0.0023 \text{ GeV}$
x	$\cos \theta$	Scattering angle in center-of-mass frame
s	Square of center-of-mass Energy ⁷	$(91.28 \text{ GeV})^2$
t	Mandelstam variable	$-\frac{s}{2}(1-x)$
P_e	Initial state electron polarization ⁷	0.7292
g_A	electron- Z^0 axial-vector coupling	value extracted from log-likelihood fit (see section 7.3)
g_V	electron- Z^0 vector coupling	value extracted from log-likelihood fit (see section 7.3)

3.2 Radiative Corrections

As pointed out in Chapter 2, radiative corrections must be correctly taken into account as they significantly alter the size and shape of the differential cross section.

There are several classes of radiative corrections that must be understood and included properly. The most important are initial and final state photon radiation

⁷ The values shown in the table for the electron polarization P_e and center-of-mass energy E_{cm} is for the 1997 run as measured by the Compton Polarimeter (see section 4.1.3) and WISRD energy spectrometer (see section 4.1.4). The actual values of P_e and E_{cm} for each run and dataset are given in Table 4-1 and Table 4-2, respectively, and the log-likelihood fits use these correct values. The values shown in the table for the 1997 run period is true for 70% of the entire wide-angle Bhabha dataset, and is typical for all datasets.

(collectively called photonic corrections), which can reduce the Bhabha cross section by as much as 30%. Section 2.6 above describes this in more detail.

In principle, these diagrams can be calculated and included analytically as we did for the tree level expressions describing Bhabha scattering. However, the expressions are quite involved, particularly when taking into account phase space cuts on the kinematics (which represent the event selection cuts in 6.4 below) for the photonic corrections. Many of the integrals are so computationally involved that they must be performed numerically, so in practice special purpose programs are used (such as Monte Carlo generators) to calculate these radiative corrections.

Although there are several approaches we could take to incorporate these radiative corrections in the tree level expressions[18], we choose a simple, straightforward approach of fitting the tree level expressions to the angular distributions generated by a wide-angle Bhabha Monte Carlo program which takes into account all of the important radiative corrections

We use UNIBAB[19], a wide-angle Bhabha Monte Carlo program that explicitly supports helicity amplitudes (therefore allowing us to specify initial state lepton polarization, extremely important in this analysis), and handles leading logarithmic radiative corrections to all orders using a parton shower algorithm which includes exponentiation of the soft photon contribution as well as multiple emission of hard collinear photons. UNIBAB includes in the generated particles the full kinematics from multi-photon emission for both ISR (initial state radiation) and FSR (final state radiation), although the interference between ISR and FSR is not included. Except for this initial-final state radiation interference, all other QED as well as Weak virtual corrections are included.

A few of the input parameters to UNIBAB were changed from their default values to reflect more recent values of experimental results and to increase the phase space into which events are generated. These values are given in Table 3-3.

Table 3-3 UNIBAB input parameters changed from their default values to reflect more recent experimental results and to increase the phase space into which events are generated.

Variable Name	Semantics	Value
masslz	Z^0 mass[7]	91.1876 GeV
masslt	top quark mass	175 GeV
masslh	Higgs mass	150 GeV
alphas	$\alpha_s(q^2 = M_{Z^0}^2)$	0.118
ctsmmin	minimum $\cos \theta_{\text{CMS}}$	-0.985
ctsmmax	maximum $\cos \theta_{\text{CMS}}$	0.985
ecut	minimum outgoing e^+e^- energy	10 GeV
acocut	maximum e^+e^- acolinearity angle	40°
evisct	minimum invariant mass of final state	0 GeV

Two datasets, each containing 10^6 events, were generated for two different initial-state electron polarization values, $P_e = -0.7292$ and $P_e = +0.7292$, which corresponds to the 1997 run period configuration. For these datasets, UNIBAB reported cross sections of 6.0126 ± 0.0059 nb for the left helicity events and 5.607 ± 0.0055 nb for the right helicity events. These events were then passed through the appropriate event selection criteria described in section 6.4 below, after which 554,125 left helicity events remained and 527,971 right helicity events remained, giving effective cross sections of 3.3317 nb and 2.9603 nb respectively. To form a single dataset containing the proper fraction of left and right helicity events for $P_e = \pm 0.7292$, the 554,125 left helicity events were combined with

$$\frac{2.9603 \text{ nb}}{3.3317 \text{ nb}} \times 554,125 = 492,354 \text{ right helicity events.}$$

The procedure we invented to extract the radiative corrections from this dataset is to group the 10 tree level terms into three logical categories based on our knowledge of the physics involved: the 4 s-t interference terms, the three s-channel terms, and the three t-channel terms. One coefficient is assigned to each group, and the resulting sum of all three groups, given below by equation (3.11), is then simultaneously fit to the UNIBAB generated dataset, the angular distributions of which are shown in Figure 3-4.

$$\begin{aligned}
\frac{\partial \sigma}{\partial x} = & \epsilon_1 \left(\frac{\partial}{\partial x} \sigma_{\gamma(s)\gamma(t)} + \frac{\partial}{\partial x} \sigma_{Z(s)\gamma(t)} + \frac{\partial}{\partial x} \sigma_{Z(t)\gamma(s)} + \frac{\partial}{\partial x} \sigma_{Z(s)Z(t)} \right) + \\
& \epsilon_2 \left(\frac{\partial}{\partial x} \sigma_{\gamma(s)\gamma(s)} + \frac{\partial}{\partial x} \sigma_{Z(s)\gamma(s)} + \frac{\partial}{\partial x} \sigma_{Z(s)Z(s)} \right) + \\
& \epsilon_3 \left(\frac{\partial}{\partial x} \sigma_{\gamma(t)\gamma(t)} + \frac{\partial}{\partial x} \sigma_{Z(t)\gamma(t)} + \frac{\partial}{\partial x} \sigma_{Z(t)Z(t)} \right)
\end{aligned} \tag{3.11}$$

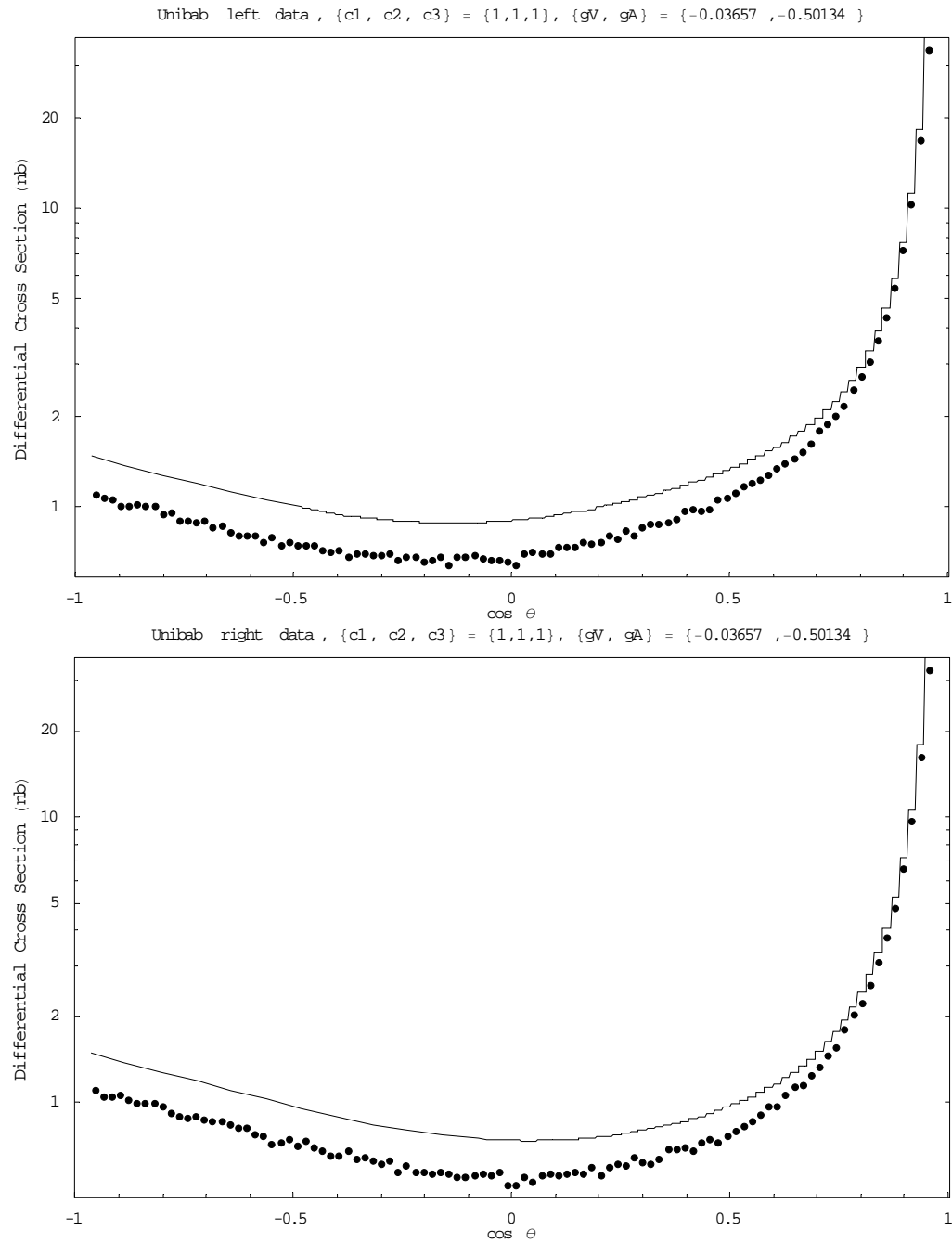


Figure 3-4 Overlay of tree level expression (solid line) and UNIBAB generated events (points) showing the Bhabha differential cross section as a function of $\cos \theta$. The difference between the two curves is entirely due to radiative corrections, which can be seen to be as much as 30% over a significant range of $\cos \theta$.

Since values for \bar{g}_v^c and \bar{g}_a^c are not among UNIBAB's free parameters we use the program ZFITTER[20] to determine the Standard Model values of \bar{g}_v^c and \bar{g}_a^c that correspond to UNIBAB's input parameters. ZFITTER calculated $\bar{g}_v^c = -0.03657$ and $\bar{g}_a^c = -0.50134$ for $M_{\text{top}} = 175$ GeV and $M_H = 150$ GeV, which we also verified from Figure 12.2 in[7].

The fit for c_1 , c_2 and c_3 is performed using Mathematica[21], and the results of the fit are given in Table 3-4 and shown in Figure 3-5. Notice the change in sign of c_1 , the s-t interference coefficient.

Table 3-4 Radiative correction coefficients from fitting equation (3.11) to the UNIBAB distributions in Figure 3-5.

Coefficient Name	Description	Radiative Correction Coefficient
c_1	s-t interference terms	-0.2199
c_2	s-channel terms	0.7346
c_3	t-channel terms	0.8510

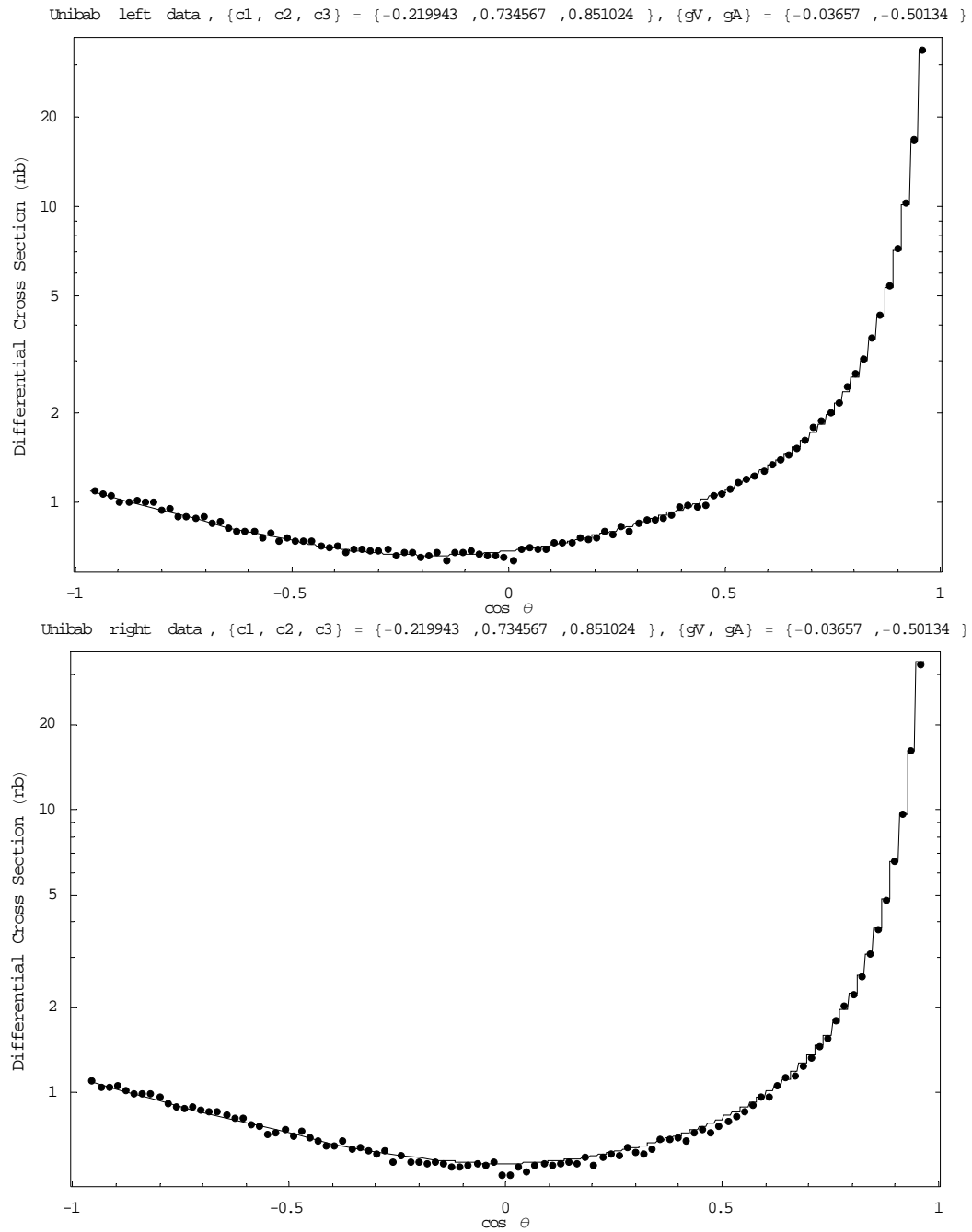


Figure 3-5 Overlay of tree level expression corrected for radiative corrections using c_1 , c_2 , and c_3 from Table 3-4 (solid line) and UNIBAB generated events (points) showing the Bhabha differential cross section as a function of $\cos \theta$.

The sum of each of the three groups of terms with and without radiative corrections are plotted as a function of $\cos\theta$ in Figure 3-6 using the coefficients from Table 3-4. The top plot represents the fit for left-handed UNIBAB events ($P_e = -0.7292$), the bottom plot for the right-handed UNIBAB events ($P_e = +0.7292$). The upper line in each plot is the s-channel group, the middle line is the t-channel group, and the lower line is the s-t interference group. The solid lower line in both plots (the s-t interference group) has been inverted to allow it to be shown on the plot since c_1 , the s-t interference coefficient, is negative.

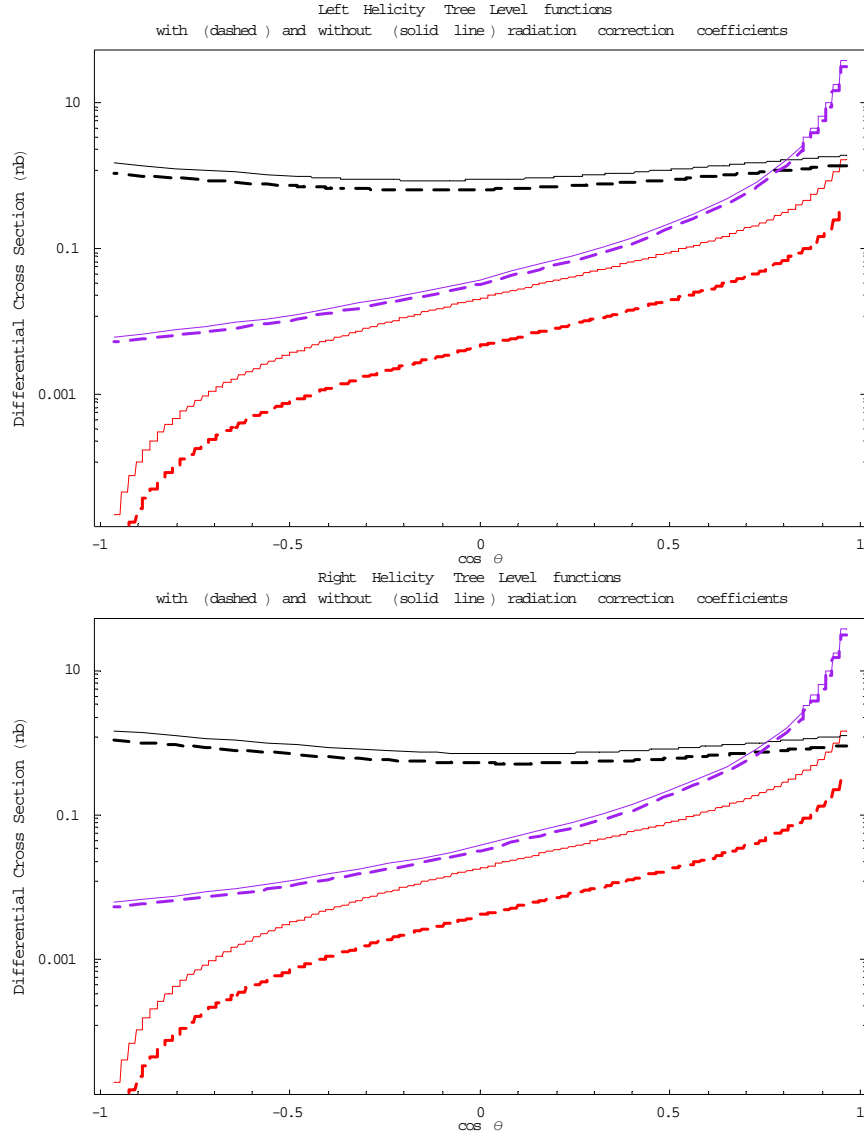


Figure 3-6 The three groups of terms without radiative corrections (solid line) and with radiative corrections (dashed line) using the coefficients from Table 3-4 plotted as a function of $\cos \theta$. The top plot represents the fit for left-handed UNIBAB events ($P_e = -0.7292$), the bottom plot for the right-handed UNIBAB events ($P_e = +0.7292$). The upper line in each plot is the s-channel group, the middle line is the t-channel group, and the lower line is the s-t interference group. The solid lower line in both plots (the s-t interference group) has been inverted to allow it to be shown on the plot since c_1 , the s-t interference coefficient, is negative

With these three coefficients in hand we now have an analytical expression for polarized wide-angle Bhabha scattering that incorporates radiative corrections which we can use to fit the wide-angle Bhabha angular distributions from section 6.4 below for the parameters \overline{g}_V^e and \overline{g}_A^e .

CHAPTER 4 EXPERIMENTAL APPARATUS: SLC AND SLD

The data used for the measurements presented in this dissertation were taken using the SLAC Large Detector (SLD) and the SLAC Linear Collider (SLC) located at the Stanford Linear Accelerator Center in Menlo Park, CA. This chapter describes this experimental apparatus combination.

The SLC is the world's first, and so far only, electron-positron linear collider. The SLC can collide polarized or unpolarized electrons with unpolarized positrons, and was designed specifically for Z^0 physics programs which began with the Mark II experiment[22] from 1989-1990 and continued with the SLD experiment from 1991-1998.

The design and construction of the SLC and SLD involved hundreds of talented physicists and engineers over the course of many years (a complete list of SLD collaborators and institutions is provided in Appendix A). Therefore, this chapter provides only a broad, descriptive overview of the SLC and SLD and focuses on the key characteristics of producing, transporting and colliding polarized electron beams with unpolarized positron beams, and detecting the output from these beam collisions. References to comprehensive and detailed descriptions of the SLC and SLD are provided in the citations.

4.1 SLAC Linear Collider (SLC)

The SLC was conceived as an inexpensive way to upgrade the existing SLAC linac to produce electron-positron collisions at a center-of-mass energy on and around the Z^0 resonance of about 91 GeV[23]. Unlike a storage ring, a linear collider is a single-pass device whereby the electrons and positrons are discarded after each pass through the machine. Figure 4-1 shows a schematic view of the SLC, which is a 3 km long linear accelerating structure composed of 230 klystrons and joined by two 1 km long non-accelerating arcs, one for the electrons and one for the positrons, which bring the particles into collision.

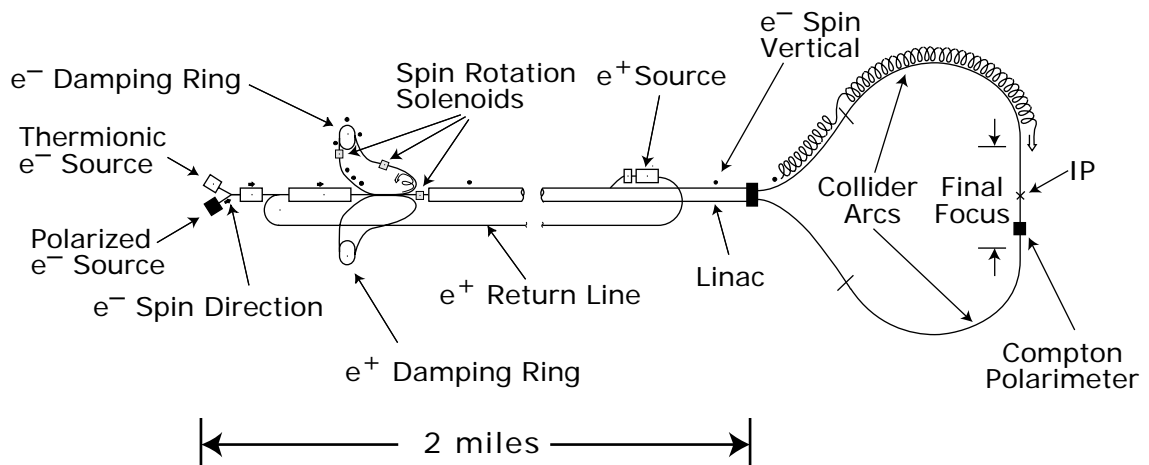


Figure 4-1 Schematic view of the SLC. Electrons and positrons are accelerated from the left of the diagram and collided at the interaction point at the far right (labeled IP in the figure), which is surrounded by the SLD detector.

Two bunches of highly polarized electrons (with a polarization $P_e \approx 78\text{-}80\%$) are produced by photoemission from a strained gallium arsenide cathode[24] and injected into the front of the linac along with one unpolarized positron bunch from the positron source. The SLC machine cycle begins when the first section (about 100 m) of the linac is pulsed

with radio frequency (RF) power which accelerates the three bunches to 1.2 GeV at which point the electron bunches are injected into the North Damping Ring (NDR) and the positron bunches are injected into the South Damping Ring (SDR). Each electron bunch is stored for one damping cycle (8.3 ms) in the NDR to reduce their transverse phase space, or *emittance*, by a factor of about 100 through radiation damping. Each positron bunch, which have much larger emittance due to the positron production process, spend two damping cycles (16.6 ms) in the SDR where their emittance is reduced by a factor of about 1000. The emittance must be reduced in this manner for the small beam sizes required at the interaction point. Each bunch is composed of about 3.5×10^{10} particles.

A positron bunch and two electron bunches are extracted from their respective damping rings and accelerated down the rest of the linac with an accelerating gradient of about 20 MeV/m. At about 2 km down stream where the energy of each bunch is about 30 GeV, the trailing electron bunch (the so-called scavenger bunch) is extracted and slammed into a transversely rotating⁸ six radiation length long tungsten-tantalum slab which produces a shower of low energy positrons, electrons and photons[27, 28]. A portion of the positron spectrum is collected and transported through the e^+ return line back to the injector at the front of the linac where the positron production cycle begins anew.

The remaining electron and positron bunches are accelerated to the end of the linac to an energy of about 47 GeV (about 1 GeV above the collision energy) where the electrons are steered into the North Arc and the positrons into the South Arc. The sole purpose of the 1 km long arcs is to preserve the low emittance electron and positron bunches while bringing

⁸ The tungsten-tantalum slab rotates to prevent it from cracking and melting due to the pressure shock from the concentrated 290 joules of incident energy contained in each electron bunch, which is dissipated in the target in only a few picoseconds[25, 26].

them into collision at the IP. Each arc has a bending radius of 279 m, which causes each bunch to dissipate about 1 GeV of energy through synchrotron radiation.

The electron and positron bunches finally enter the final focus section composed of three superconducting quadrupole magnets which focus the bunches into collision at the interaction point inside of the SLD detector. The size of the bunches at collision are about 2 μm wide and 0.5 μm high. The bunches pass through each other and into the opposing final focus sections where they are steered into beam dumps and discarded.

The whole SLC machine cycle from injection at the head of the linac to the beam dumps occurs at a repetition rate of 120 Hz.

The luminosity \mathcal{L} of a collider determines the rate for any physics process according to the equation

$$\text{rate} = \text{events per unit time} = \mathcal{L}\sigma \quad (4.1)$$

where σ is the cross section for the physics process of interest. For a linear collider the equation for luminosity is

$$\mathcal{L} = \frac{N^+ N^- f}{4\pi\sigma_x \sigma_y} H_d \quad (4.2)$$

where N^\pm are the number of electrons (N^-) and positrons (N^+) in each bunch at the interaction point, f is the collider repetition frequency, $\sigma_{x,y}$ are the average horizontal (x) and vertical (y) beam sizes and H_d is the dimensionless *disruption enhancement factor* whose value is $H_d \geq 1$ and increases with increasing beam intensities and decreasing transverse and longitudinal beam sizes. The disruption enhancement factor H_d is a phenomenon whereby

the electrostatic forces of the overlapping beams serve to pinch or squeeze the beam particles closer together, thereby increasing luminosity. For the SLC $f = 120$ Hz, $N^\pm \approx 4 \times 10^{10}$, $\sigma_x \approx 1.5 \mu\text{m}$, $\sigma_y \approx 0.7 \mu\text{m}$ and $H_d \approx 1-2$.

4.1.1 SLC Polarized Electron Source

The schematic view of the SLC Polarized electron source is shown in Figure 4-2. Circularly polarized light is created by two pulsed YAG pumped Ti:Sapphire lasers in combination with circular polarizers. The linearly polarized light from the lasers is passed through a Pockels Cell, an electro-optic device that can create left or right circularly polarized light depending on the drive voltage. This drive voltage is randomly varied for each laser pulse so that bunches of left and right circularly polarized photons are produced in equal amounts but in a random sequence in order to eliminate any possible systematic effects with other periodic effects of SLC operations.

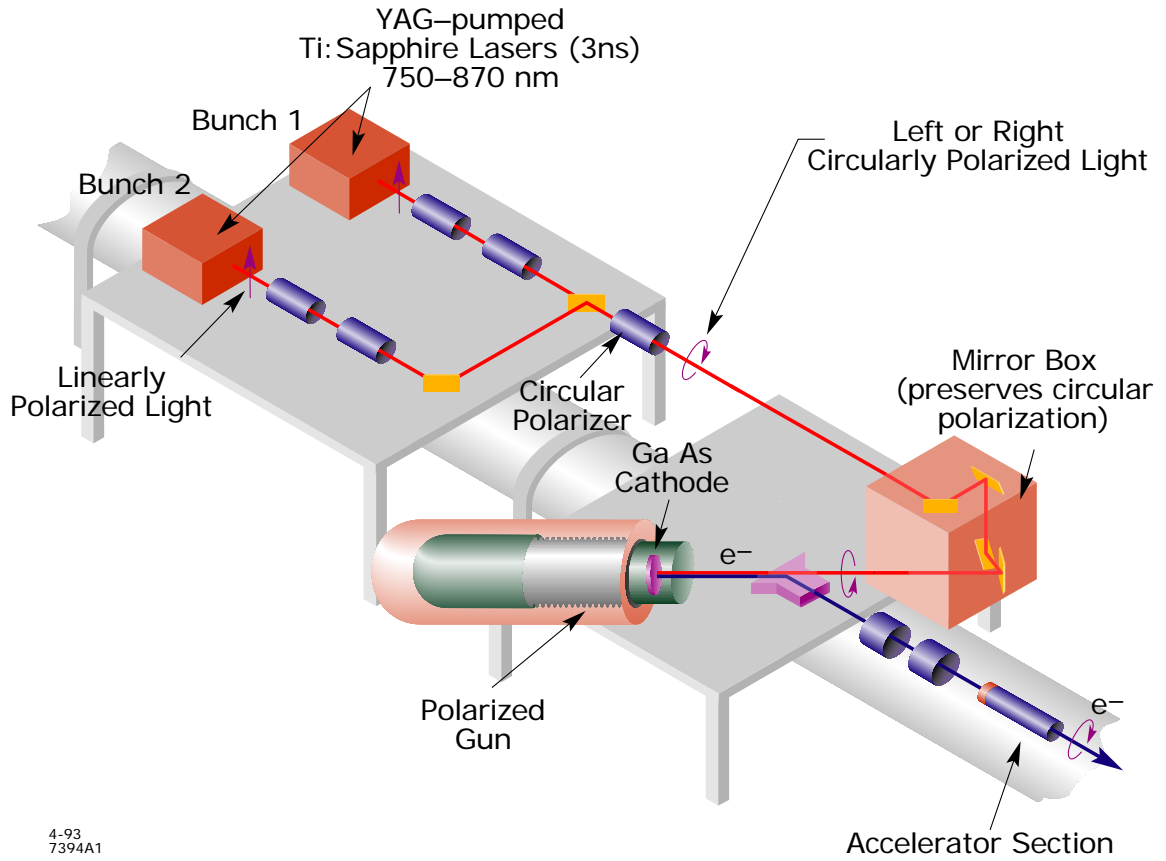


Figure 4-2 Schematic view of the SLC Polarized electron source.

The lasers operate at about 850 nm to produce the circularly polarized laser pulses, which are then used to irradiate a gallium arsenide (GaAs) semiconductor cathode to photoemit polarized electrons. Electrons are excited from the $P_{\frac{3}{2}}$ valence band to the $S_{\frac{1}{2}}$ conduction band with longitudinal polarization since they absorb one unit of angular momentum from the polarized photons.

In a normal *bulk* GaAs semiconductor the $P_{\frac{3}{2}}(m_j = \pm \frac{3}{2}) \rightarrow S_{\frac{1}{2}}(m_j = \pm \frac{1}{2})$ transitions occur in a 3:1 ratio to the $P_{\frac{3}{2}}(m_j = \pm \frac{1}{2}) \rightarrow S_{\frac{1}{2}}(m_j = \mp \frac{1}{2})$ transitions (this is simply Clebsch-Gordan coefficient algebra). These transitions would therefore normally yield a maximum theoretical polarization of $P_e = \frac{3-1}{3+1} = 50\%$.

However, the SLC polarized gun uses a *strained* photocathode, which consists of depositing a 100 nm thick layer of GaAs on a GaAsP substrate. The resulting photocathode is said to be *strained* because the difference in the lattice spacing of the two materials leads to a strain on the epitaxial GaAs layer, which breaks the degeneracy in the $P_{\frac{3}{2}}(m_j = \pm \frac{3}{2})$ and $P_{\frac{3}{2}}(m_j = \pm \frac{1}{2})$ valence bands and yields a maximum theoretical polarization of 100%. The energy level diagrams for bulk and strained GaAs semiconductors are shown in Figure 4-3.

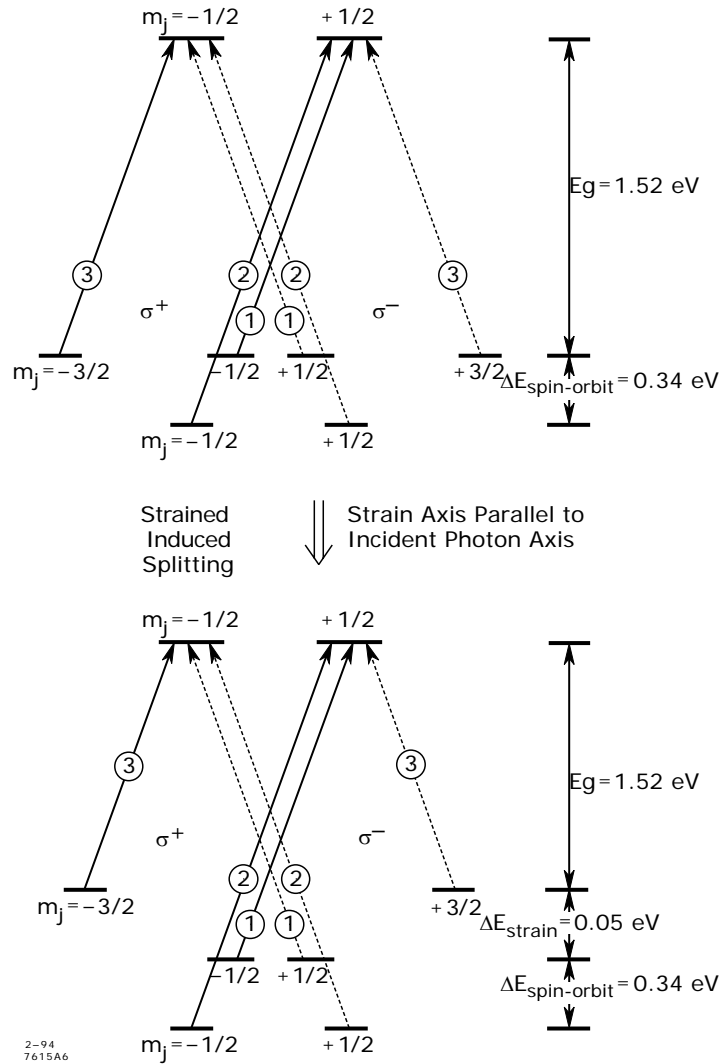


Figure 4-3 Energy level diagram of the SLC Polarized Electron Source. The diagram on the top is for normal *bulk* GaAs where the $P_{\frac{3}{2}} (m_j = \pm \frac{3}{2})$ and $P_{\frac{1}{2}} (m_j = \pm \frac{1}{2})$ energy levels are degenerate and the theoretical maximum polarization is 50%. The diagram on the bottom is for strained GaAs where the degeneracy is removed, allowing for a theoretical maximum polarization of 100%. The numbers in circles correspond to the Clebsch-Gordan transition probabilities.

The electrons emitted from the photocathode had a typical polarization of $P_e \approx 78\text{-}80\%$ for the 1994-1998 run periods.

4.1.2 Spin Transport Through the SLC

The SLC Polarized Source emits electrons with longitudinal polarization, which remains longitudinal during injection into the linac and throughout the 1.2 GeV acceleration phase to the NDR. However, the polarization of the electron bunch would quickly dissipate (by becoming randomized) in the NDR if the spin were left longitudinal because of spin-precession. Therefore, a combination of bending magnets and a solenoid (called the linac-to-ring or LTR solenoid) are used to rotate the electron spin vector perpendicular to the plane of the damping ring to preserve the polarization during the many thousands of orbits of the electron bunch within the NDR. However, the LTR was designed for a 1.21 GeV electron bunch while the actual energy of the electron bunch is closer 1.19 GeV, so the spin rotation perpendicular to the plane of the damping ring is not perfect which results in about a 1% loss in polarization once the electron bunch eventually exits the NDR.

Upon exiting the NDR the spin of the electron bunch remains transverse to the direction of motion (perpendicular to the plane of the NDR) and is accelerated to about 47 GeV to the end of the linac and the entrance to the SLC Arcs. The spin is unperturbed during this acceleration phase and has a magnitude of about 77-79%, which is about the same value as at the SLC Polarized Electron Source modulo the small 1% loss of polarization in the NDR.

The purpose of the SLC Arcs is to bend the trajectory of the electron and positron bunches by $\pm 90^\circ$, respectively, to bring them into collision while also rotating the electron spin from vertical to longitudinal by the time the electron bunch reaches the interaction point. The particle trajectories actually followed in the SLC Arcs are a complicated orbit in three dimensions dictated by the physical size constraints of the SLAC campus and its

irregular surface elevation. There are 23 achromats in the North Arc (and 22 in the South Arc) each comprised of 20 combined function magnets to provide the bending and focusing necessary to traverse the roughly 1 km horizontal distance and 23 m of vertical displacement to reach the interaction point.

The challenge of rotating the electron spin from a vertical orientation to a longitudinal orientation is solved by a natural⁹ resonance of the spin phase advance due to the dipole bending magnets and the spin phase advance due to betatron oscillations¹⁰ induced by the quadrupole focusing fields within each achromat. It was found that inducing two large betatron oscillations, or *spin bumps*, in the later sections of the North Arc could serve to align the electron spin longitudinally[29] at the interaction point. The sizes of these spin bumps were tuned empirically to maximize the longitudinal polarization at the SLD IP.

The 1 GeV energy loss in the SLC Arcs due to synchrotron radiation creates a natural energy spread in each bunch, which tends to depolarize the bunch. The luminosity weighted average polarization for the 1994-1998 SLD runs was 74%, indicating about a 4-6% loss of polarization in the SLC Arcs.

4.1.3 Polarization Measurement: SLD Polarimeter

The precise and accurate measurement of the electron beam polarization is fundamental to nearly every analysis of SLD data. This polarization measurement is performed by the SLD Compton Polarimeter, the most precise and accurate high-energy

⁹ Fortuitous might be a better word, since the spin phase advance due to the dipole bending magnets and the quadrupole field induced betatron oscillations wasn't designed to be equal. It was simply serendipity that such a resonance occurred.

¹⁰ Betatron oscillations are the induced transverse oscillations that occur due to the magnetic field of the quadrupole magnets.

polarimeter in the world. Detailed descriptions of every aspect of the SLD polarimetry program already exist in the literature, such as detailed overall descriptions of the hardware setup[30, 31], detector simulation[32], laser polarization and systematic error measurements[33] and numerous cross-checks[34, 35]. Therefore, what follows will be an overview of the most important aspects of how electron polarization is measured at SLD.

The principle behind measuring the electron beam polarization is to use the well-known and easily calculable Compton scattering process¹¹. Circularly polarized photons are prepared with a known spin state and collided with the outgoing longitudinally polarized electrons from the SLD interaction point. There are two different scattering cross sections depending on whether the electron and photon spins are parallel ($\sigma_{j=\frac{3}{2}}$) or anti-parallel ($\sigma_{j=\frac{1}{2}}$). The size of the two cross sections are different ($\sigma_{j=\frac{3}{2}} > \sigma_{j=\frac{1}{2}}$) and can be calculated to extremely high precision since it is a pure QED process. Measurement of the cross section and knowledge of the photon polarization P_γ allows for the simple determination of P_e [17].

The schematic diagram of the SLD Compton Polarimeter setup is shown in Figure 4-4. The polarized electrons leaving the interaction point travel about 30 m downstream to collide with 2.33 eV circularly polarized photons from a 532 nm Nd:YAG laser, which is pulsed at 17 Hz. Since the electron bunches are produced by the SLC at 120 Hz while the Compton laser pulses at 17 Hz, only every seventh electron bunch is sampled. The laser light is circularly polarized using Pockels Cells similar to the SLC Polarized Source described in section 4.1.1 above. The rather round-about path of the laser light as depicted in Figure 4-4 is due to the limited space in the SLC Arcs and the desire to have access to the laser system during SLC running (the SLC Arcs are sealed during running due to radiation exposure safety hazards). The Compton laser and optics bench sit in a shack on the hilltop outside of

¹¹ See any introductory text on quantum field theory, for example[36].

the SLD Collider Hall, and the laser light is delivered through a shaft to the beam line about 50 m below. The laser light passes through a small window in the SLC vacuum beam pipe, collides with the electrons at a 10 mrad. crossing angle, and exits through another small window to an analysis box.

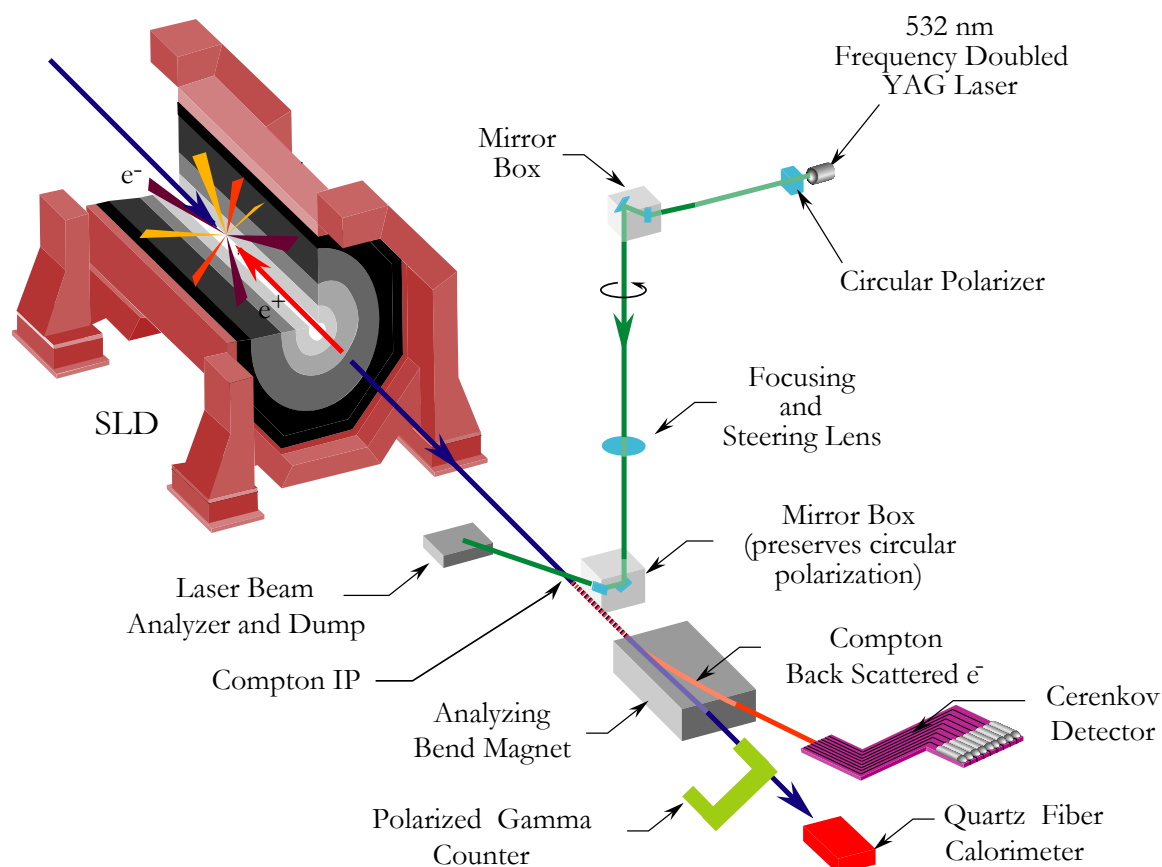


Figure 4-4 SLC Compton Polarimeter. After passing through the SLD Interaction Point at the center of the SLD detector, the polarized electron bunch continues about 30 m downstream to the Compton Interaction Point where the electrons are collided with polarized photons. The Compton scattered electrons are momentum analyzed by a bending magnet and detected in a segmented Cerenkov counter.

The now off-energy Compton scattered electrons (typically about 1,000 per laser pulse) are passed through momentum analyzing bend magnets and into a nine channel

threshold Cerenkov counter instrumented with photomultiplier tubes to measure the Cerenkov light. In practice only the first seven Cerenkov channels are used which corresponds to electrons with an energy in the range between 17.4 GeV (corresponding to full back scattering) and about 25 GeV.

The Polarimeter data acquisition system takes data for runs of about 20,000 beam crossings (or about 3 minutes), and each run occurs about once every 10 minutes during nominal running. Each 3 minute Polarimeter run therefore produces a polarization measurement with about a 2% statistical error. Since the electron beam polarization changes very slowly as a function of time (on the time scale of hours), each 3 minute Polarimeter run is an extremely accurate measurement of the electron beam polarization for the Z^0 events collected by the SLD during these runs.

Understanding of the Polarimeter systematic errors steadily improved throughout its operation, culminating in a total fractional error of only 0.50% for the final years of SLD data taking. The final polarization measurements for the data used in this dissertation are give in Table 4-1.

Table 4-1 Polarization measurements for each SLD run period[17].

Run Period	Electron Polarization
1994-1995	0.7723 ± 0.0052
1996	0.7616 ± 0.0040
1997-1998	0.7292 ± 0.0038

4.1.4 Energy Measurement: SLD WISRD

The energy of every electron and positron bunch is measured by a pair of energy spectrometers known collectively as the Wire Imaging Synchrotron Radiation Detector (WISRD)[31, 37, 38]. There is one spectrometer for the electron bunches and one spectrometer for the positron bunches, which are each located after the collision point in the respective extraction lines just before the beam dumps. The schematic layout of one WISRD detector is shown in Figure 4-5.

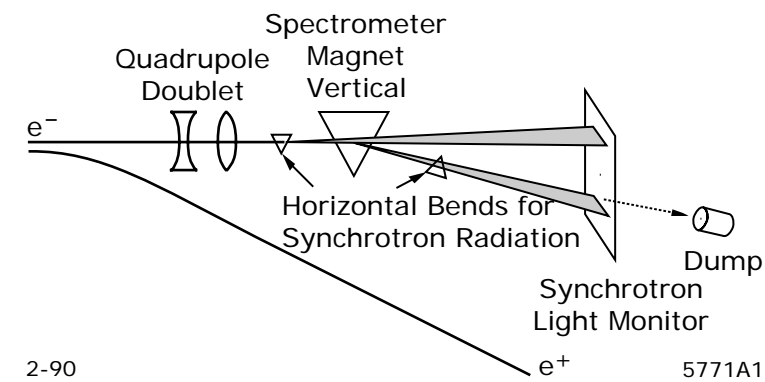


Figure 4-5 Schematic view of SLC Energy Spectrometers (WISRD).

Each spectrometer is composed of a string of three dipole bending magnets that each bunch passes through. The purpose of the first and last dipole bending magnets is to simply generate a stripe of synchrotron light that is detected via Compton scattering of electrons from an array of finely spaced copper wires ($100\text{ }\mu\text{m}$ on center) downstream of the magnets. The central dipole bending magnet is a precisely calibrated analysis magnet which bends the charged particles in each bunch by an amount inversely proportional to their energy. The first and last dipole bending magnets are oriented parallel to one another but perpendicular to the central dipole analysis magnet. This configuration generates two parallel

stripes of synchrotron radiation on the copper wire array. The deflection angle of the bunch is measured by measuring the distance between these two stripes and knowledge of the distance between the central dipole analysis magnet and the copper wire array. Knowing the magnetic field of the central dipole analysis magnet allows a precise determination of the bunch energy according to the equation $E_{\text{bunch}} = \frac{c}{\theta} \int |\vec{B} \times d\vec{l}|$, where θ is the deflection angle of the bunch, \vec{B} is the magnetic field of the central dipole analysis magnet, $d\vec{l}$ is the path of the bunch through this magnet and c is the speed of light.

The energy spectrometers have a measurement precision of ± 20 MeV. The accuracy of the spectrometers was measured during May of 1998 (a few months before the end of the final SLD run) by performing an energy scan of the Z^0 resonance to calibrate the energy spectrometers to the precisely known Z^0 mass from the LEP measurement. The energy scan used two carefully chosen off-peak energy points, a high energy point of $+0.88$ GeV and a low energy point of -0.93 GeV. The luminosity for the high and low energy points was 167 nb^{-1} and 177 nb^{-1} , respectively¹². Using a luminosity of $1,840 \text{ nb}^{-1}$ for the on-peak data¹² allowed for a statistical uncertainty of ± 20 MeV on the peak position. A careful analysis[39] showed an offset of -46 MeV on the peak position and a total uncertainty of ± 29 MeV. The final E_{cm} measurements for the data used in this dissertation are give in Table 4-2.

Table 4-2 E_{cm} and E_{cm} width (expressed as a percentage of E_{cm}) measurements for each SLD run period.

Run Period			Width
1994-1995	91.280 \pm	0.025 GeV[40]	$\pm 0.110\%$ [41]
1996	91.26 \pm	0.03[9]	$\pm 0.109\%$ [42]
1997	91.237 \pm	0.029[9]	$\pm 0.107\%$ [42]
1998	91.237 \pm	0.029[9]	$\pm 0.142\%$ [42]

¹² I calculated these luminosities using the Luminosity Monitor data for the run numbers given in Table 5-3.

4.2 SLAC Large Detector (SLD)

The SLD was originally proposed in 1984[43] to be a general purpose particle detector designed to measure physics observables at the Z^0 resonance. Specifically, it was designed to identify particles in the momentum range from several hundred MeV/c up to about 50 GeV/c. The SLD came online in 1991 for an engineering (or commissioning) run and subsequently ran from 1992 through 1998 taking data for the SLD collaboration's Z^0 physics program. The SLD sits in the Collider Experimental Hall (CEH) in Building 280 of the SLAC campus adjacent to its predecessor, the Mark II detector, which was rolled out of the beam-line to make room for the SLD.

A cutaway view of the SLD is shown in Figure 4-6 with the various subsystems labeled. The SLD is a state-of-the-art, fully digital particle detector composed of concentric layers of multiple detector subsystems that collectively measures the momentum, energy, charge and particle identity of the products of Z^0 decays. The entire SLD is located within a 0.6 Tesla solenoidal magnetic field¹³. All of the subsystems are fully digital, with analog-to-digital conversions occurring on electronics mounted on or near the subsystem's active elements inside of the SLD. All subsystem data is simultaneously delivered over a relatively small fiber optic cable plant to the data acquisition system which literally sits atop the SLD.

¹³ The magnetic flux return for the solenoid is itself an instrumented calorimeter, and is labeled "Magnet Iron and Warm Iron Calorimeter (WIC)" in Figure 4-5. So technically one of the SLD calorimeters does sit outside of the solenoidal field.

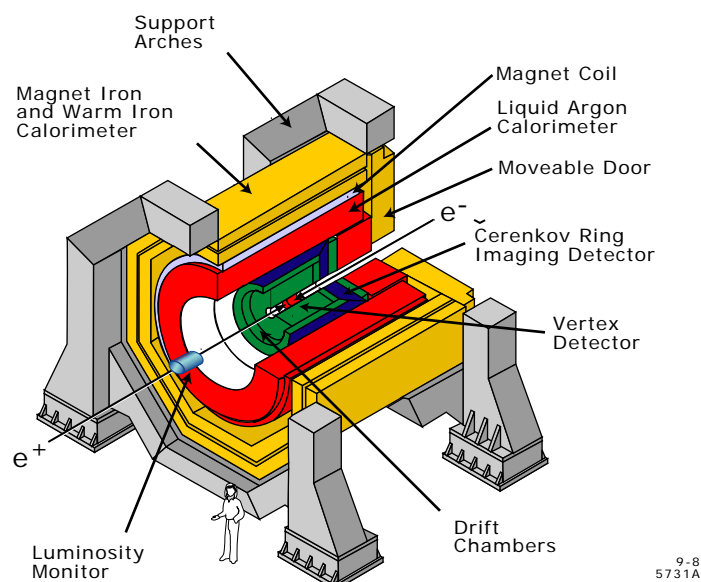


Figure 4-6 Isometric view of the SLD showing the cylindrical layout of the various barrel subsystems. The endcap subsystems are not shown. Only one of the two Luminosity Monitor modules is shown.

The SLD is centered on the SLC interaction point and covers nearly 4π of the solid angle. The SLD is physically separated into thirds, and is composed of one barrel assembly (which covers approximately $2/3$ of the solid angle), and two endcap assemblies. Figure 4-7 shows a quadrant view of the entire SLD with the barrel and endcap shown together. During data taking the two endcap assemblies are pushed into the ends of the barrel assembly which provides a radiation-tight hermetic seal and a radiation free environment in the CEH. This allows the data acquisition electronics, high-voltage and low-voltage supplies and the various gas and plumbing elements to be conveniently located on and around the SLD for easy access by service and repair personnel during SLC operations. It also allows for tours of the general public at any time.

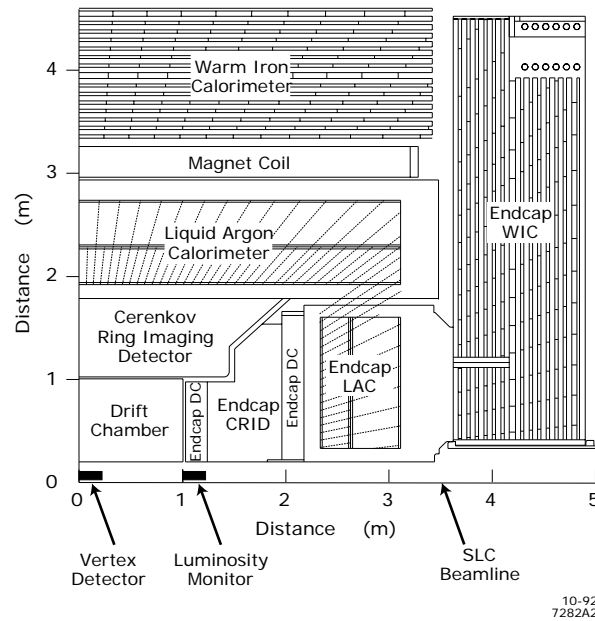


Figure 4-7 Quadrant view of the SLD showing the radial and longitudinal symmetry of the barrel and endcap subsystems.

The following sections describe the operational principles of each detector subsystem, beginning with the innermost detectors and working outward. The calorimeter subsystems will be described in greater detail since they are used exclusively for the analysis of this dissertation. The coordinate system used in the descriptions and figures that follow is a right-handed coordinate system with the z -axis along the e^+ beam direction and the y -axis along the vertical pointing towards the sky.

4.2.1 Vertex Detector

The SLD uses a Vertex Detector (VXD) wrapped snugly around the interaction point to measure secondary vertices from heavy quark and tau lepton decays. The VXD measures tracks from the passage of charged particles and is one of SLD's two tracking

systems. It is built out of a large collection of Charge Coupled Device (CCD) chips that allow precise three dimensional imaging of the interaction point. Charged particles ionize the silicon as they pass through a pixel, and the pixels are continuously read out during data taking. Track and vertex finding algorithms are applied later during offline reconstruction to identify secondary vertices and participate with Drift Chamber reconstruction to identify and measure charged particle tracks.

Two VXD devices were used over the lifetime of the SLD experiment; VXD2[44] was a 120 Mpixel device used for the 1992-1995 runs, while VXD3[45] was a 300 Mpixel device used for the 1996-1998 runs. VXD3 was an ambitious upgrade to VXD2 which provided greater solid angle acceptance, better position resolution and reduced material.

Figure 4-8 shows a schematic view of VXD2, which is constructed of 480 CCDs. The entire device is operated at a temperature of 190 K to suppress dark currents in the silicon. The CCDs are mounted on *ladders*, with 4 CCDs per ladder. The ladders are mounted into four concentric cylindrical layers, with the innermost layer at a radius of 3 cm and the outermost layer at a radius of 4.2 cm. Each CCD contains 375×578 pixels, and each pixel has an area of $(22 \mu\text{m})^2$. On average 2.3 pixels are hit for each charged track passing through the detector.

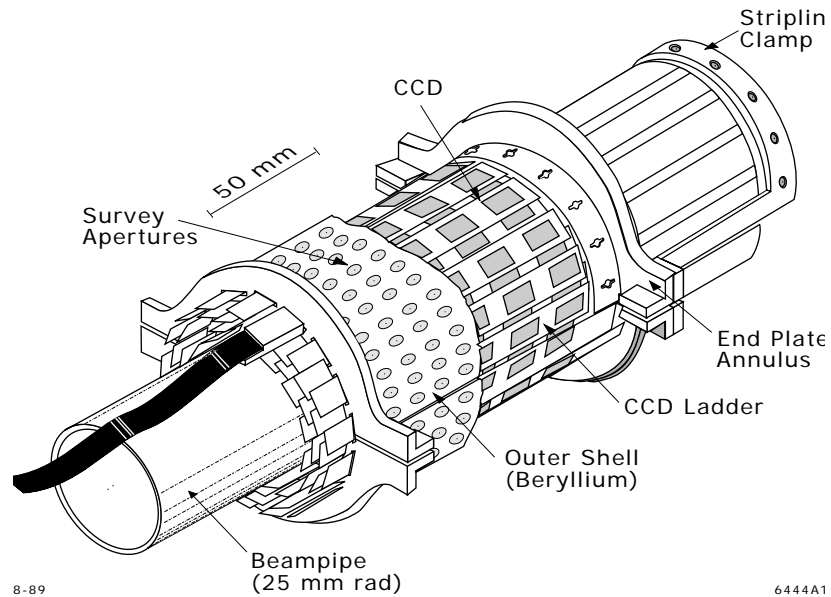


Figure 4-8 Schematic view of VXD2, the original SLD Vertex Detector.

A schematic view of VXD3 is shown in Figure 4-9. Due to advances in CCD technology it is constructed of 96 CCDs which are arrayed into three concentric cylindrical layers. Each CCD has $4,000 \times 800$ pixels, and each pixel has an area of $(20 \mu\text{m})^2$.

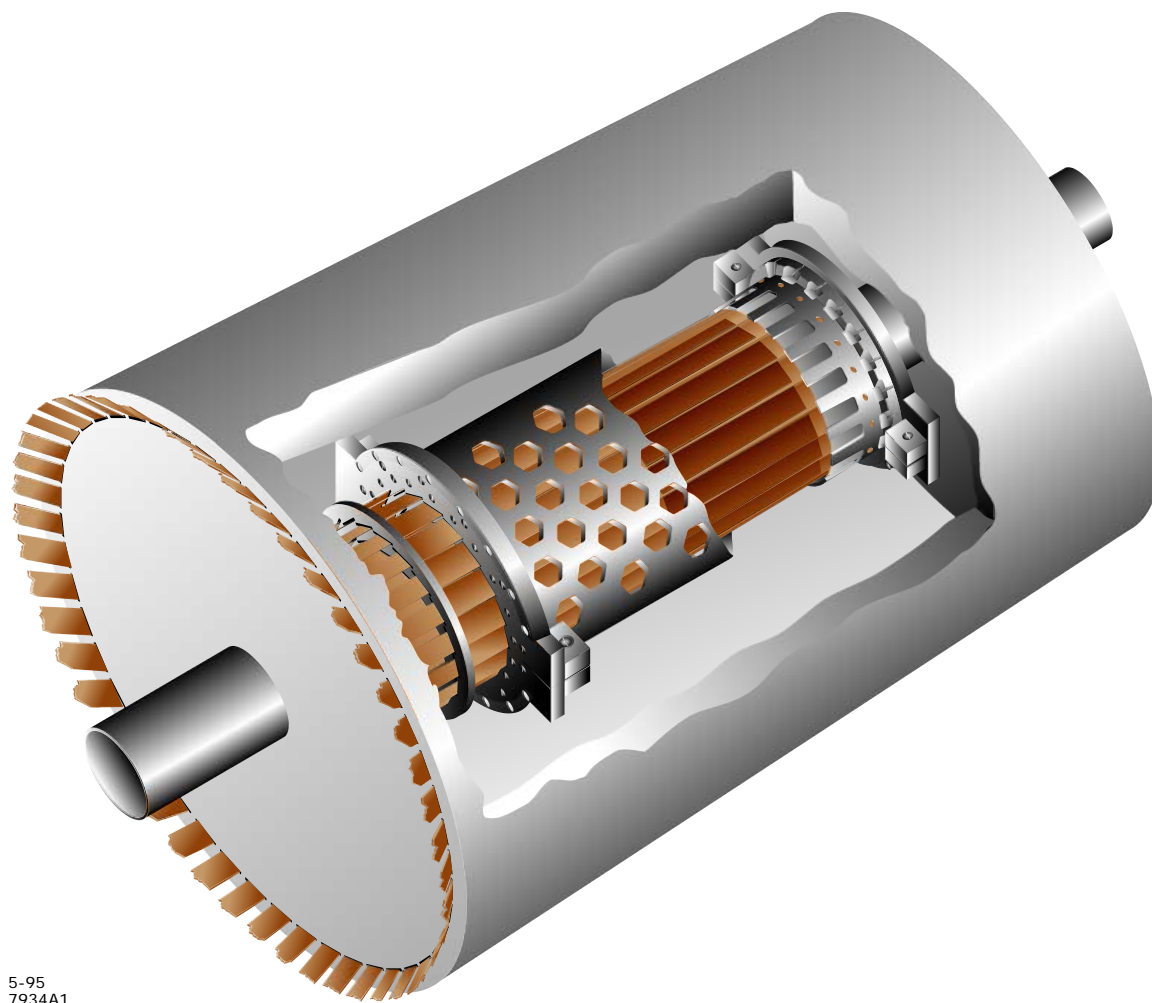
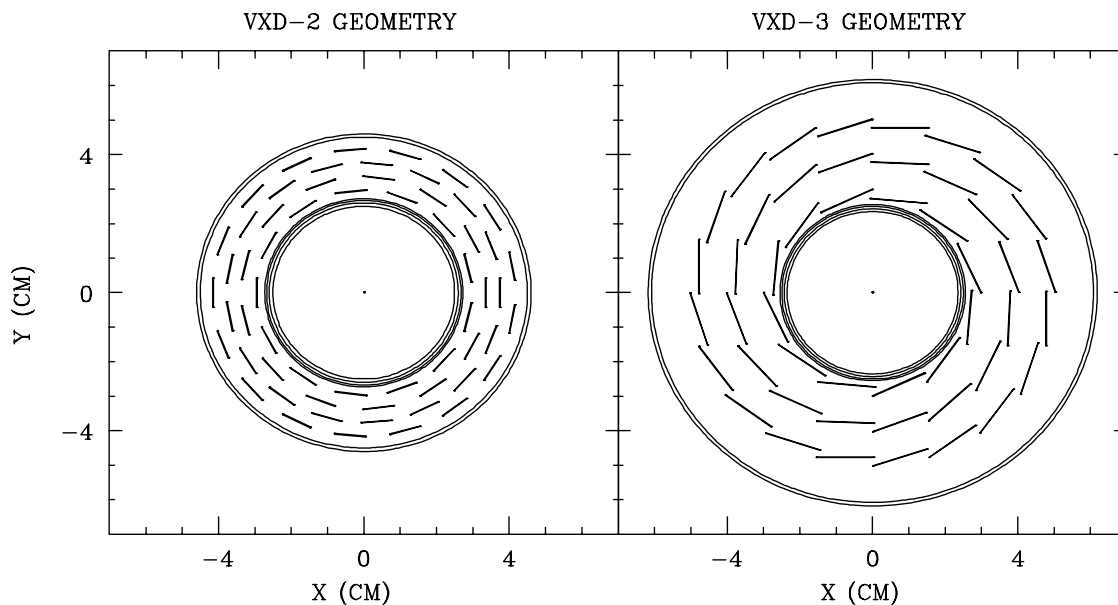


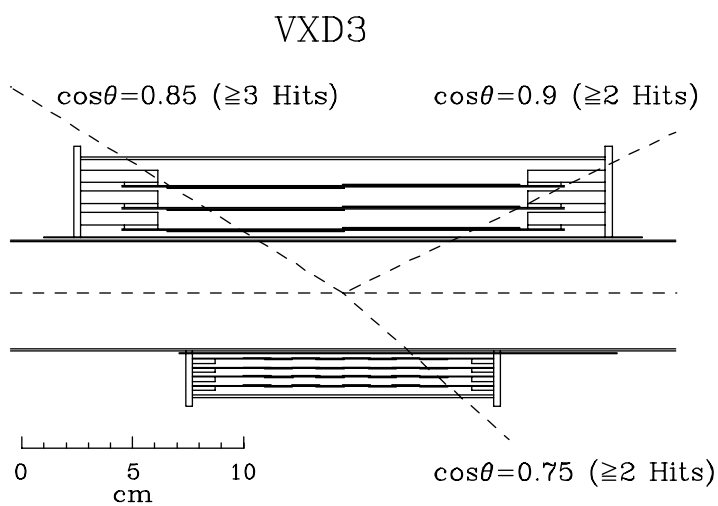
Figure 4-9 Schematic view of VXD3, the upgraded SLD vertex detector.

Views in the r - ϕ plane of VXD2 and VXD3 are shown in Figure 4-10, from which it is seen that the VXD3 ladders overlap completely, while the VXD2 ladders do not. The overlapping ladders of VXD3 allows for full three hit acceptance and therefore standalone track finding capability independent of tracks found in the drift chamber. Figure 4-11 shows views of VXD2 and VXD3 in the r - z plane where it is seen that VXD3's three hit acceptance extends well past the entire acceptance of VXD2.



INDYPAK 14-43-29 4SFP95

Figure 4-10 VXD2 (left) and VXD3 (right) as viewed in the r - ϕ plane.



VXD2

Figure 4-11 VXD2 and VXD3 as viewed in the r - z plane.

4.2.2 Drift Chamber

SLD's primary track finding detector is the Drift Chamber, which is physically split into the Central Drift Chamber (CDC)[46] located in the barrel region of the SLD, and two Endcap Drift Chambers (ECDC) located in each of the two SLD endcaps. The CDC is an annulus with a length of 1.8 m, an inner radius of 20 cm and outer radius of 1 m. As shown in Figure 4-6 the CDC and ECDC sits within the 0.6 T uniform magnetic field provided by the solenoid. The Drift Chambers are filled with a gaseous mixture and instrumented with several thousand wires running the entire length of the chambers. As charged particles traverse the chambers they ionize the gas, and the charge from the liberated electrons is collected and measured along *sense* wires made of 25 μm gold-plated tungsten. Other wires called *guard* and *field* wires are made of 150 μm gold-plated aluminum and produce electrostatic fields which serve to focus and amplify the charge towards the sense wires.

In the CDC the sense, guard and field wires are arranged in a geometry that creates physical cells with a size of about 6 cm wide and 5 cm high. The cells are arrayed into 10 concentric *superlayers*, with four superlayers coaxial to the beam (called the *axial* layers) and the remaining six interleaved in pairs at angles of ± 41 mrad. to the axial layers (called the *stereo* layers). The charge from the sense wires is read from both ends so that charge division can be used to measure the z position of a track. This arrangement allows full three-dimensional imaging of a charged particle's track passing through the chamber.

The CDC employed a gas mixture of CO_2 :argon:isobutane: H_2O in the ratios 75:21:4:0.3. The composition of the gas is chosen empirically to provide low drift velocity (about 8 $\mu\text{m}/\text{ns}$) and low charge diffusion (provided by the CO_2), good spatial resolution (an

average of 82 μm), high gain (provided by the argon), quenching (provided by the isobutane) and negligible wire aging (provided by the H_2O).

The CDC is able to fully reconstruct tracks out to $|\cos\theta| < 0.65$, and provides partial tracking out to $|\cos\theta| < 0.87$. It is 96% efficient at finding tracks with momentum above 4 GeV/c, and falls to 93% efficiency for a track momentum of 100 MeV/c. The momentum resolution was measured to be $\left(\frac{\sigma_{p_\perp}}{p_\perp}\right)^2 = 0.010^2 + (0.0050 p_\perp)^2$ where p_\perp is the track momentum transverse to the beam axis in units of GeV/c[47]. The first term is the uncertainty due to multiple scattering, while the second term is the measurement error.

Track finding using the ECDC proved difficult due to material in front of the detectors and SLC beam related backgrounds, and was therefore never used in SLD physics analysis.

4.2.3 Cerenkov Ring Imaging Detector (CRID)

Identification of charged particles is performed by the Cerenkov Ring Imaging Detector (CRID)[48-50]. The CRID operates on the principle of the Cerenkov effect where the passage of a high velocity charged particle through a dielectric media excites atoms in the dielectric which then emit a coherent wavefront of light at a fixed angle. The effect only happens when the velocity of the charged particle, βc , is greater than the speed of light in the dielectric, c/n , where n is the refractive index of the dielectric. The emission angle of the Cerenkov light relative to the particle trajectory is given by $\cos\theta_c = \frac{1}{\beta n}$. Therefore, measuring θ_c and knowing n determines the particle's velocity. Combining this with a knowledge of the particle's momentum (measured by the CDC) allows the determination of the particle's mass, and hence its identity.

The CRID is split like the Drift Chamber into one barrel section which covers $|\cos \theta| < 0.72$ and two endcap sections to complete the angular coverage. A schematic view of one barrel CRID module is shown in Figure 4-12. The barrel CRID is composed of 40 modules arrayed around the CDC. Each CRID module uses two radiating mediums in order to extend the detectable range of momentum, using a liquid radiator composed of C_6F_{14} and a gaseous radiator composed of C_5F_{12} . The CRID can identify particles with momenta up to 6 GeV/c for e/π and 30 GeV/c for $\pi/K/p$ [48]. The Cerenkov photons from both radiators are detected in a Time Projection Chamber (TPC), which is a volume of ethane drift gas (C_2F_6) mixed with 0.1% of the photosensitive agent tetrakis(dimethylamino)ethylene (TMAE). The photoelectrons are drifted to the ends of each module (much like the CDC) and detected by multi-wire proportional chamber (MWPC) detectors. The photoconversion position of the ring formed by the Cerenkov photons are reconstructed in three dimensions and matched with CDC tracks.

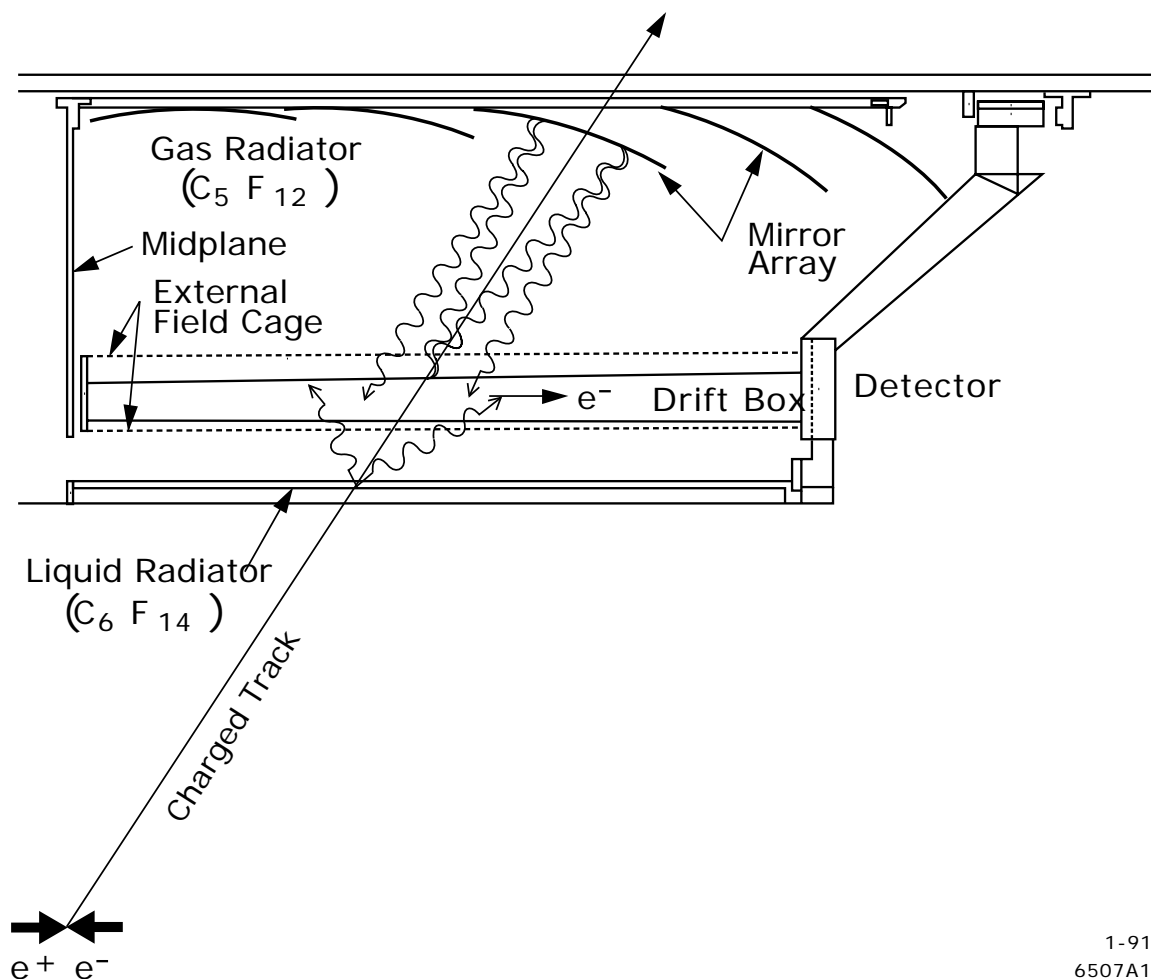


Figure 4-12 Schematic view of a single CRID module.

1-91
6507A1

Although the endcap CRID was operational and took data for much of SLD's running, it was never used for physics analysis because of the lack of ECDC tracks.

4.2.4 Liquid Argon Calorimeter

The primary calorimetry for the SLD is provided by the Liquid Argon Calorimeter (LAC). The original plan for the SLD calorimeter was a compensating uranium/liquid argon

calorimeter[43]. After an intensive study of uranium/liquid argon, including beam tests and detailed Monte Carlo simulations, a new understanding of compensation in calorimetry was developed[51]. It was realized that a liquid argon calorimeter could not easily be made compensating, and the radiator was changed to lead.

The LAC is a non-compensating sampling calorimeter designed to measure the energy of incident electromagnetic and hadronic particles. The operational principle of a sampling calorimeter is that of total absorption of the incident particle. The incident particle passes through alternating layers of a radiating¹⁴ material and an instrumented sampling material until it deposits all of its energy. The signal from the instrumented sampling material then corresponds to some fraction of the total incident energy. The LAC uses slabs of lead for the radiator/absorber material, and liquid argon for the sampling material. As shown in Figure 4-13, stacks of large lead sheets and segmented lead tiles are bathed in a common volume of liquid argon. The lead sheets are grounded while the tiles, separated by plastic spacers, are held at high voltage and serve as charge collecting electrodes. The segmented tiles allow the position of the energy deposition to be measured.

¹⁴ Although the LAC uses only one material, lead, to force the incident particle to interact, the material is called a *radiator* when referring to incident electromagnetic particles and an *absorber* when referring to incident hadronic particles.

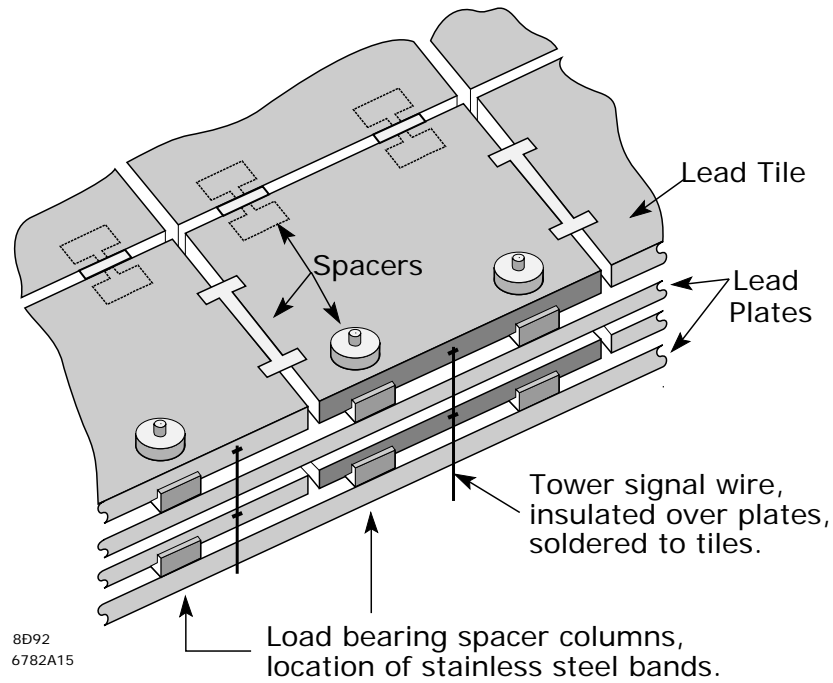


Figure 4-13 The LAC uses stacks of large lead sheets and segmented lead tiles as the radiator/absorber material, which are bathed in a common volume of liquid argon which serves as the sampling material. The lead sheets are grounded while the tiles are held at high voltage and serve as charge collecting electrodes.

The LAC is divided into a barrel section and two endcap sections just like the Drift Chamber and the CRID. The barrel LAC begins at a radius of 1.77 m and extends to a radius of 2.91. m, and is physically constructed from 288 modules. Each module is ~ 30 cm wide and ~ 2 m long and comes in two types, electromagnetic (EM) modules and hadronic (HAD) modules. 48 EM modules are arrayed azimuthally to provide complete 2π coverage in ϕ , and this geometry is repeated three times with the modules stacked end-to-end along the z-axis to expand the coverage in polar angle out to $|\cos\theta| < 0.84$. The HAD modules are stacked behind the EM modules. This arrangement of modules is inserted into one large cryostat which is filled with liquid argon. The entire assembly is show schematically in Figure 4-14.

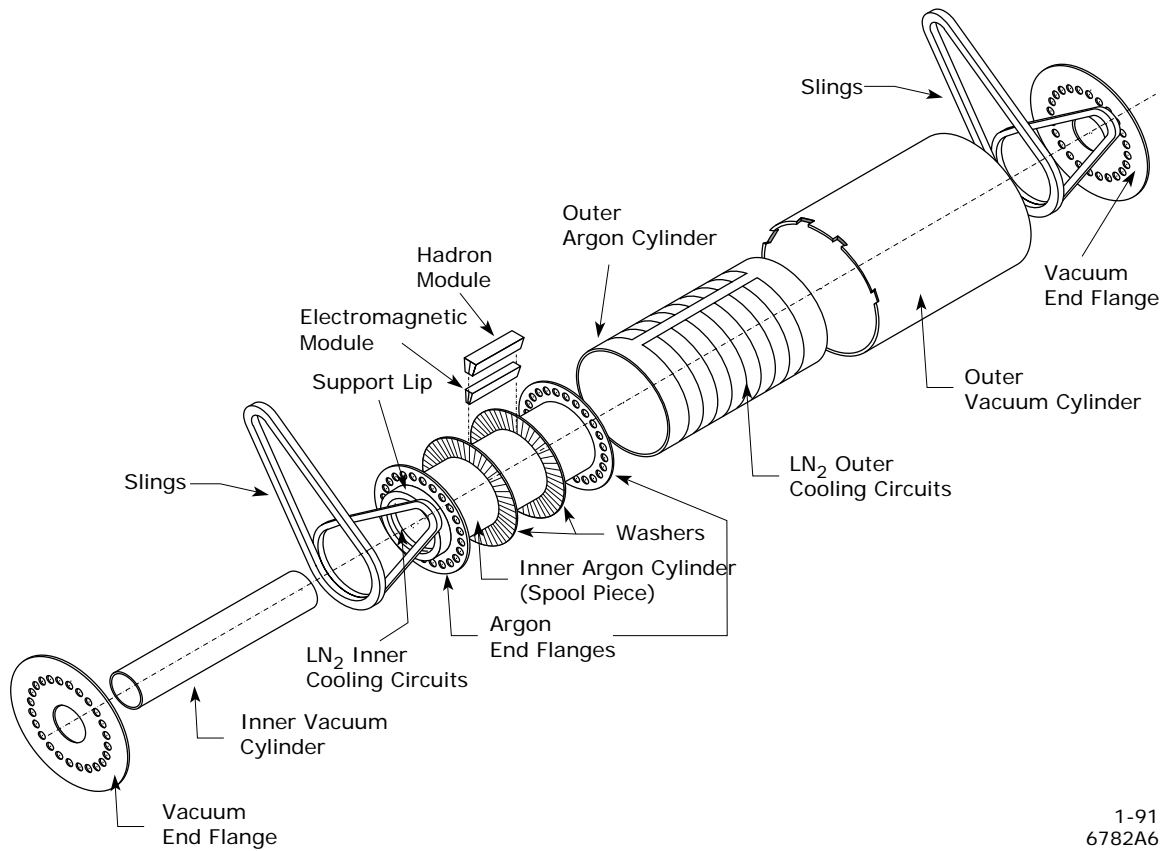
1-91
6782A6

Figure 4-14 LAC barrel assembly. 48 modules are arrayed azimuthally to provide complete 2π coverage in ϕ . Three modules are laid end-to-end along the z-axis to provide polar angle coverage out to $|\cos\theta| < 0.84$, with the modules separated by two washers. The entire assembly is bathed in a common volume of liquid argon and suspended by the slings from the SLD arches.

The lead sheets and segmented tiles in a EM module are 2mm thick and are separated by 2.75 mm liquid argon gaps. The 2mm lead slab, followed by the 2.75 mm of liquid argon followed by the 2mm lead tile forms an EM cell, which is repeated radially 28 times to form an EM tower with a total thickness of $21 X_0$ radiation lengths or 0.8λ nuclear absorption lengths. The EM section contains 98-99% of a 50 GeV electromagnetic shower. The first eight cells of six X_0 are ganged together to form a tower called EM1, and the last 20 cells of 15 X_0 are ganged together to form a tower called EM2. This radial segmentation

allows for e/π separation by providing information on the longitudinal development of electromagnetic showers.

The lead sheets and segmented tiles in a HAD module are 6 mm thick and are separated by 2.75 mm liquid argon gaps. The 6 mm lead slab, followed by the 2.75 mm liquid argon followed by the 6 mm lead tile forms a HAD cell, which is repeated radially 26 times to form a HAD tower with a total thickness of 2λ nuclear absorption lengths. The first 13 cells of 1λ are ganged together to form a tower called HAD1, and the last 13 cells of 1λ are ganged together to form a tower called HAD2. The total thickness of both EM and HAD modules is 2.8λ nuclear absorption lengths, which contains 80-90% of the hadronic shower energy on average. Figure 4-15 shows a schematic view of a HAD module stacked behind an EM module.

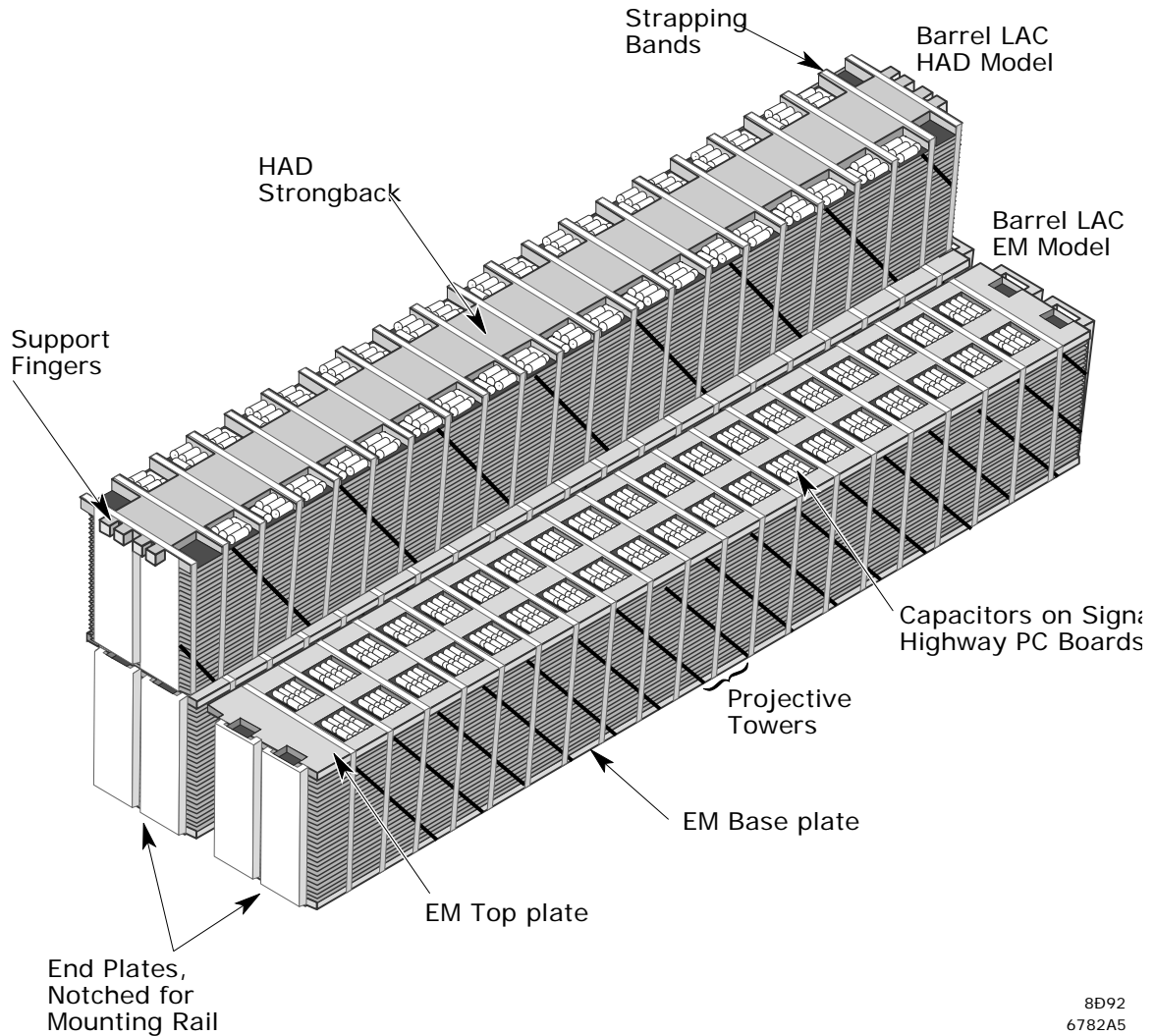


Figure 4-15 Schematic view of two LAC EM modules (shown on the bottom) and 1 HAD module (shown stacked on top). There are 28 lead/argon/lead cells in an EM module (for a total of $21 X_0$ radiation lengths or 0.8λ nuclear absorption lengths) and 26 cells in an HAD module (for a total of 2λ nuclear absorption lengths). Note the projective towers pointing to the IP (towards the lower right of the figure), with the HAD towers twice the size of the EM towers.

The segmented lead tiles, which provide the transverse segmentation of the LAC, are constructed so that the EM and HAD towers maintain a constant projective area as viewed from the IP so that electromagnetic showers are sampled equally. The EM section is divided in azimuth into 192 towers, each with an opening angle of $\delta\phi = 33$ mrad. The polar angle θ

is divided into 68 EM towers (34 on each side of the x-y plane) and decreases from $\delta\theta = 36$ mrad. at $\theta = \pm 90^\circ$ to $\delta\theta = 21$ mrad. at the edges of the barrel. The HAD towers are twice the size as the EM towers in both transverse dimensions. There are a total of 32,448 towers in the LAC barrel.

The polar angle coverage of the endcap LAC overlaps with the barrel LAC and covers $0.82 \text{ mrad.} < |\cos \theta| < 0.99 \text{ mrad.}$ Each endcap LAC is constructed of 16 pie or wedge shaped modules arrayed circularly around the beam pipe behind the Endcap Drift Chambers and Endcap CRID. Unlike the barrel LAC, the EM and HAD sections are contained in the same module. However, the thickness as seen by an incoming particle (in terms of radiation lengths and nuclear absorption lengths) for both the EM1, EM2, HAD1 and HAD2 are identical to those in the barrel modules. One entire endcap assembly is shown in Figure 4-16.

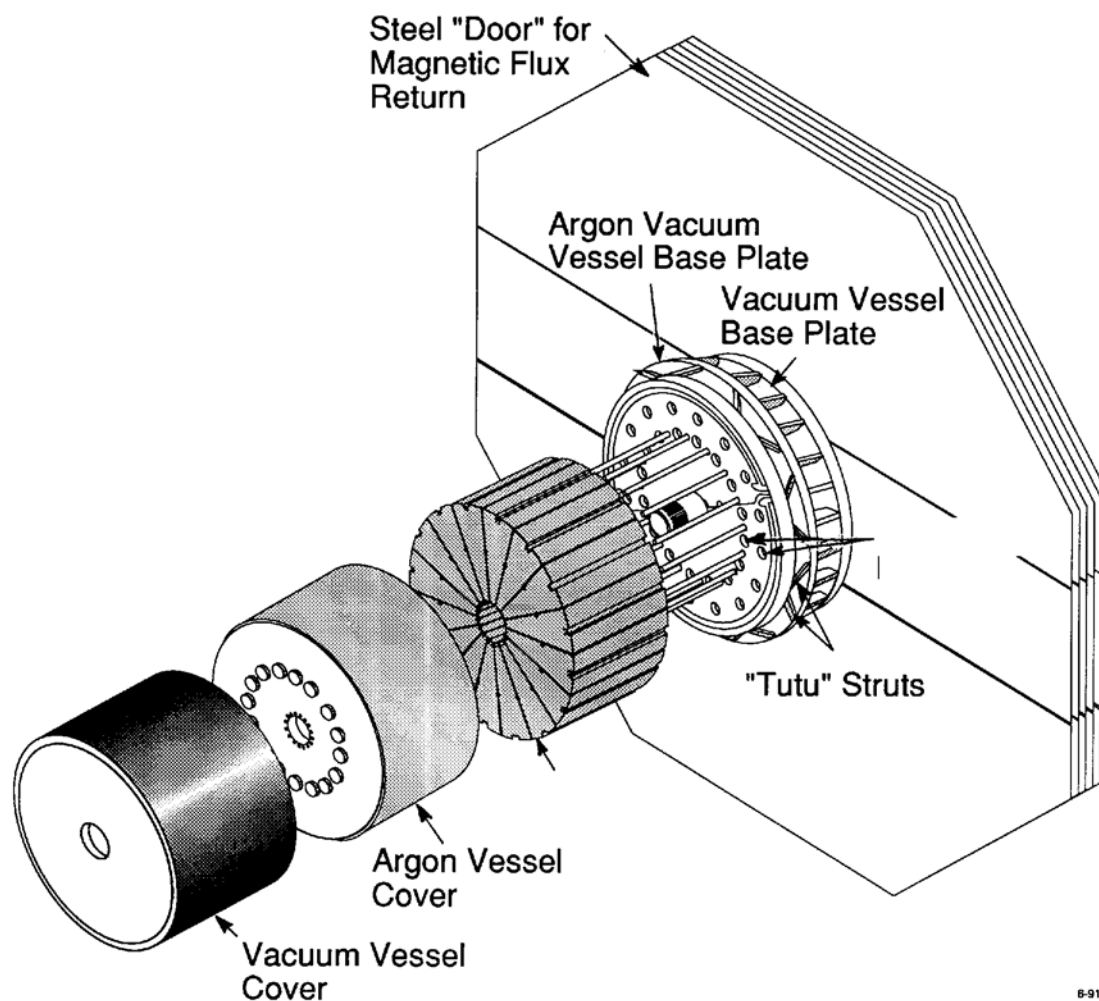


Figure 4-16 LAC Endcap assembly. 16 modules are arrayed azimuthally around the beam pipe to provide complete 2π coverage in ϕ . The entire assembly is bathed in a common volume of liquid argon and fastened to the SLD endplate doors.

To maintain the projective towers of constant area, the endcap is broken into three regions with 192 towers in azimuth at the largest radii, followed by 96 and then 48 towers at the smallest radii. The polar segmentation is broken into 17 segments in the same fashion as the barrel to keep the area perpendicular to a shower constant. The HAD towers are again twice the size of the EM towers in both transverse dimensions, just like in the barrel

modules. There are a total of 8,640 towers in both LAC endcap calorimeters. Figure 4-17 shows a schematic view of one endcap module.

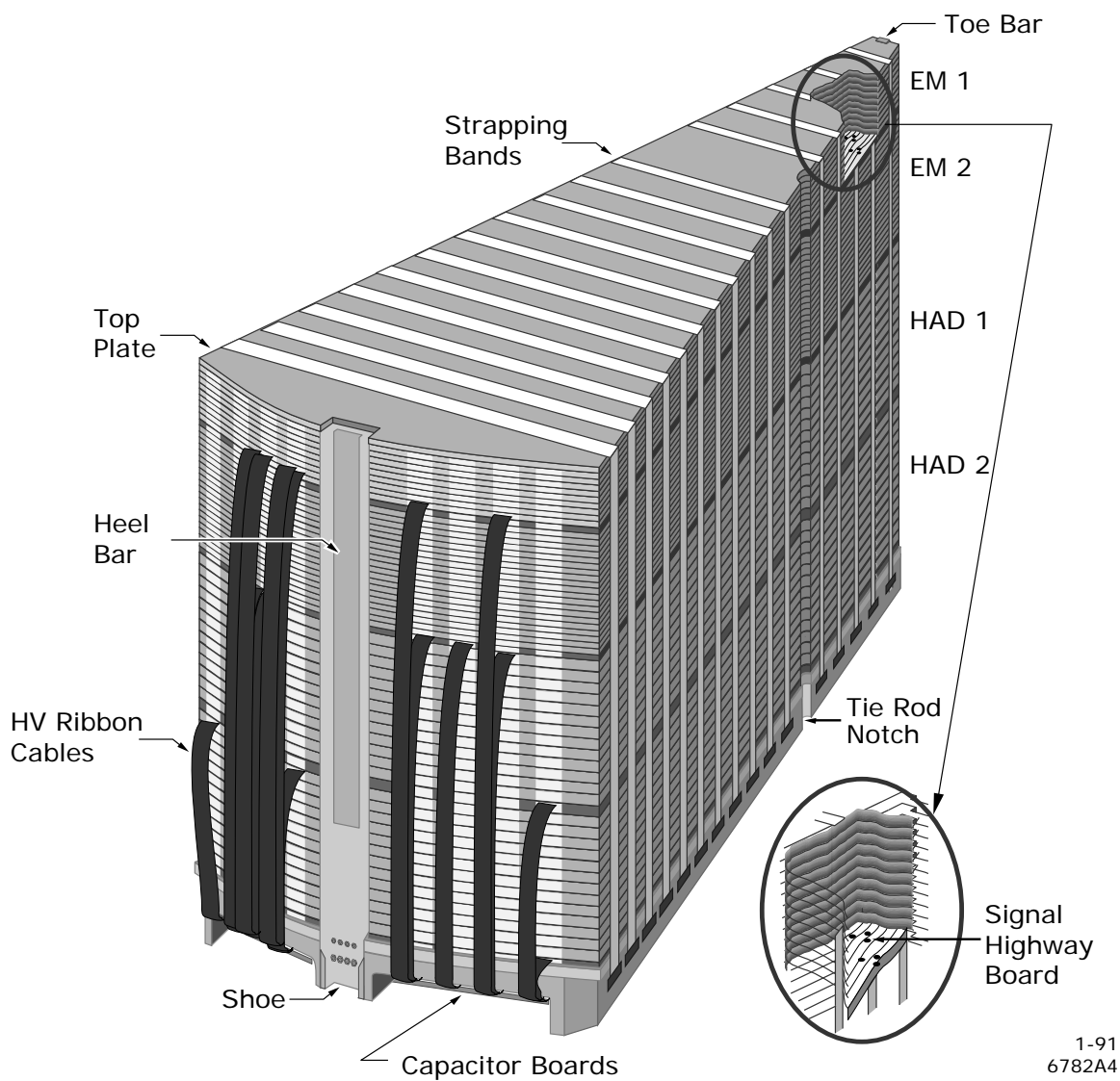


Figure 4-17 Schematic view of one endcap LAC module. Both the EM and HAD sections are in one module, unlike the barrel LAC which has separate EM and HAD modules.

The charge from the EM and HAD towers is collected, digitized and multiplexed onto optical fibers by an array of LAC electronics packages called *tophats*¹⁵, 64 of which are mounted either in a circle around both ends of the exterior LAC barrel cryostat (for the barrel modules) or around the exterior rim of the LAC endcap cryostat (for the endcap modules). The optical fibers are fed into custom FastBUS[52] Calorimeter Data Modules (CDMs) which apply calibration corrections, perform baseline subtractions and calculate trigger quantities.

The LAC has a design energy resolution of $^{10\%-12\%}/\sqrt{E(\text{GeV})}$ for electromagnetic showers and $\sim 60\%/\sqrt{E(\text{GeV})}$ for electromagnetic showers. The wide-angle Bhabha (WAB) cluster energy distributions shown in Figure 6-3 are consistent with this estimate. Shower fluctuations and material in front of the LAC (mainly the aluminum dewar) are the dominate contributors to the size of the energy resolution. However, this is just an average energy resolution, as there are regions of the barrel LAC that have a degraded energy response, such as the region where the two washers separate the barrel modules (see the plots in section 6.4 below, paying attention to the region at $|\cos\theta| \approx 0.45$) as well as the far forward regions in $|\cos\theta|$ where the material from other subsystems (detectors and electronics) cause electromagnetic showers to develop early.

The energy resolution of the endcap LAC is a different story altogether. These detectors are so far forward in $|\cos\theta|$ that particles must pass through more material (between $4 X_0$ and $7 X_0$ depending on $|\cos\theta|$ [53]) before reaching the first endcap liquid argon gap. Techniques have been developed to deal with this, which are presented in section 6.5.1 below.

¹⁵ The term tophat comes from the shape of an individual LAC electronics package, and refers to its resemblance to gentleman's formalwear. The package is composed of a 12" diameter circular backplane with electronic cards mounted vertically and covered in a black anodized cooling can.

4.2.5 Warm Iron Calorimeter (WIC)

The Warm Iron Calorimeter (WIC)[54] is also a sampling calorimeter designed to catch the *tails* of hadronic showers leaking from the LAC as well as to provide muon tracking. It is the only SLD detector subsystem to sit outside of the SLD solenoid, which it must since it sits laminated in the iron which provides the flux return path for the magnetic field.

The WIC is composed of a barrel section and two endcap sections. The barrel is an octagonal cylinder constructed from 14 layers of 5 cm thick steel plates with 3.2 cm gaps between each layer[43]. The two endcaps are octagonal plates constructed of identical material, thickness and separation. The 5cm steel plates act as the absorber, each having a thickness of 0.30λ nuclear absorption lengths. Sandwiched in between the steel plates are planes of rectangular plastic *Iarocci*¹⁶ tubes. These tubes are filled with a gas mixture of 88% CO₂ (the bulk gas), 2.5% argon (the ionizing gas) and 9.5% isobutane (the quench gas), and have a coating of graphite-loaded varnish along the interior and a 100 μ m silver-coated Be-Cu wire running down the center. The tubes are surrounded by Glasteel (similar to the G10 used for printed circuit boards) laminated with copper, which is etched into either pads or strips.

The Be-Cu wire running down the center of the tubes is held at 4.7 KV, which operates the tubes in *limited streamer mode*. As charged particles pass through the gas, the argon ionizes and the liberated electrons accelerate towards the wire, eventually gaining enough energy to cause a limited avalanche or cascade to form a small streamer. The pads and strips act as capacitive electrodes which pick up the signals from the streamers. The pads

¹⁶ So-called because their design is similar to those used by the Iarocci group in Frascati for the Mont Blanc proton decay experiment.

are used for calorimetry and the strips are used for muon track finding. The pads follow the same transverse tower segmentation as that of the HAD sections of the LAC. There are a total of 18 layers of Iarocci tubes in both the barrel and endcap that are mounted in both longitudinal and transverse orientations so that the strips provide for three-dimensional hit information for muon track finding.

The combined barrel and endcap have an acceptance out to $|\cos\theta| < 0.95$. However, there is a large gap between $0.6 < |\cos\theta| < 0.75$ (where the barrel WIC meets the endcap) which happened during construction to adhere to SLAC earthquake safety standard. Muon track finding simulations showed 95% efficiency over the entire WIC acceptance except in this gap, where the efficiency falls to 25%[55].

4.2.6 Luminosity Monitor (LUM)

All e^+e^- colliders measure luminosity by measuring the rate of small-angle Bhabha scattering ($e^+e^- \rightarrow e^+e^-$). SLD pioneered the use of silicon calorimetry when it built the SLD Luminosity Monitor (LUM), a finely-segmented silicon-tungsten sampling calorimeter. Two of the four LEP experiments (OPAL and ALEPH) subsequently replaced their original luminosity monitors with silicon-tungsten calorimeters similar in design to the LUM based on the experience of SLD. The LUM was designed and built at the University of Oregon[56].

The LUM was specifically designed to precisely measure the energy and position of the electron and positron from small-angle Bhabha scattered events¹⁷. The LUM is made out of a layered tungsten radiator structure instrumented with silicon diodes, and is composed of

¹⁷ A real-time energy-sum signal and real-time one-event event displays were also found to be useful by SLC operators when tuning the SLC for collisions.

two modules which are mounted on both ends of the superconducting final focus triplets. The front face of each LUM module is located 101 cm on either side of the Interaction Point.

Another small-angle silicon-tungsten calorimeter called the Medium Angle Silicon Calorimeter (MASC) had a similar design to the LUM and was installed in SLD until the end of the 1995 run when it was removed to make room for the installation of the VXD3 vertex detector. The MASC was mounted on the *R20 module* which held the VXD2 detector and had an acceptance of $68 \text{ mrad.} < \theta < 200 \text{ mrad.}$, which defined the outer acceptance of the LUM and provided overlapping coverage with the endcap LAC. Therefore, while the MASC was installed the SLD had full electromagnetic calorimetry coverage down to 28 mrad. The MASC was not used in the analysis of this dissertation and will not be described further.

The LUM defines an acceptance of $28 \text{ mrad.} < \theta < 68 \text{ mrad.}$, and has a thickness of $21 X_0$ radiation lengths which contains $> 99.5\%$ of a 45 GeV electromagnetic shower.

A schematic view of the r-z plane for one LUM module is shown in Figure 4-18. The LUM silicon-tungsten module is on the far right of the figure beginning at $z = 101 \text{ cm}$ and is labeled LMSAT (for Luminosity Monitor Small Angle Tagger). The cables attached to the silicon diodes drape over the aluminum backplane and attach to the LUM electronics, which are not shown in the figure. Also shown is the MASC on the left side of the diagram beginning at $z = 31 \text{ cm}$.

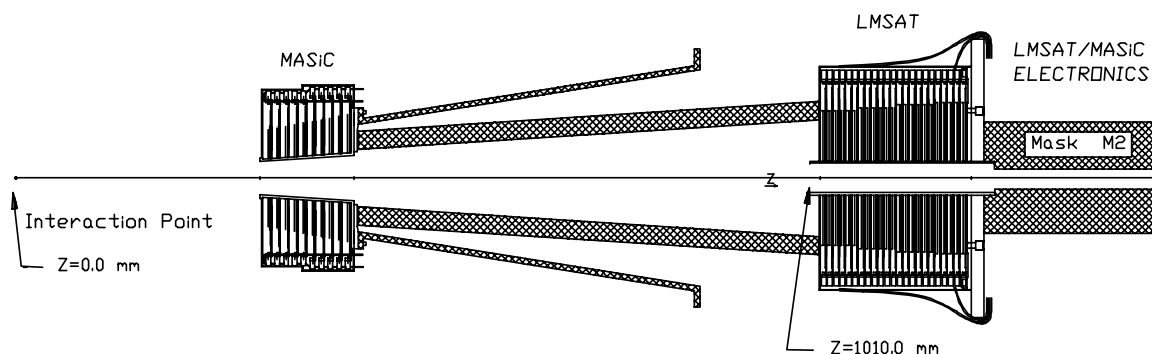


Figure 4-18 One module of the SLD Luminosity Monitor (LUM) viewed in the r - z plane. The LUM silicon-tungsten module is on the far right and begins at $z = 101$ cm. The cables attached to the silicon diodes drape over the aluminum backplane and attach to the LUM electronics (not shown). Also shown is the Medium Angle Silicon Calorimeter (MASC) which is the silicon-tungsten module on the left side of the diagram beginning $z = 31$ cm.

Figure 4-19 is a quadrant view of one LUM module and shows more detail of the alternating tungsten slabs and silicon diodes. The silicon diodes are mounted directly to the tungsten slabs.

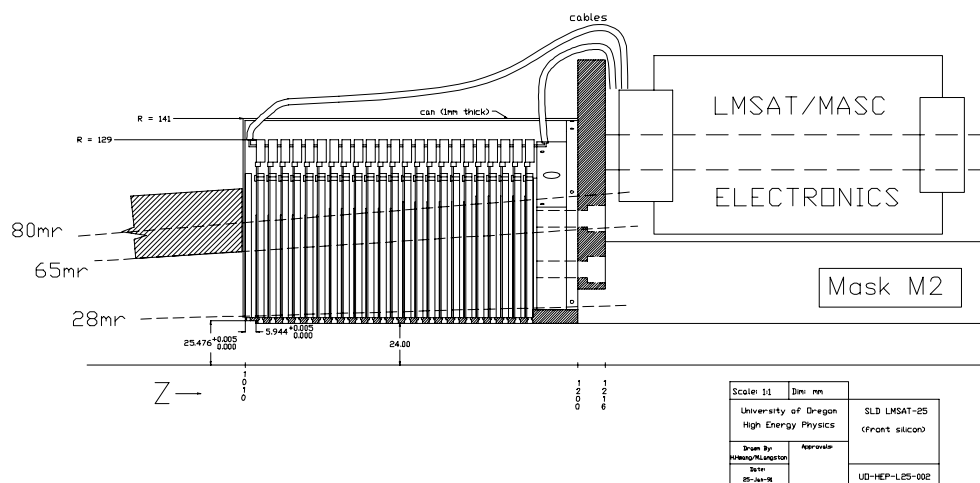


Figure 4-19 LUM quadrant view showing alternating layers of the tungsten slabs and silicon diodes.

Resegmentation From Two To Four Longitudinal Layers

The original LUM cable plant consisted of 50 conductor ribbon cable enclosed in a fine copper-mesh sheath to provide electrical isolation from capacitive crosstalk and other outside electrical interference. The copper-mesh sheath was enclosed in thick plastic insulation which made the entire cable plant difficult to service when access to the tungsten-silicon modules or electronics was required. The cable plant was so *finicky* that it was responsible for the majority of LUM hardware problems where cables would pop off of their daughterboard connectors at the most inopportune time, typically only a few hours after the SLD endcap doors were closed (an all day event requiring the talents of several people). Since the installation of VXD3 into SLD in the fall of 1995 necessitated the permanent removal of the MASC and the temporary removal of the LUM, this provided the opportunity to redesign and replace the cable plant with a more stable and flexible arrangement.

The 384 MASC electronic channels were reassigned to the LUM so that the LUM longitudinal segmentation could be increased from two sections to four sections. The original two sections were divided into the first six silicon-tungsten layers called EM1 and the remaining 17 layers called EM2. The total depth of EM1 and EM2 were $5.5 X_0$ and $15.6 X_0$, respectively. In the new longitudinal segmentation the first six silicon-tungsten layers remained EM1, but the remaining 17 layers were divided into six layers called EM2, the next six layers called EM3 and the last 5 layers called EM4. A detailed simulation using EGS4[57] showed that this configuration would sample the electromagnetic energy from a 45 GeV incident electron in the proportions 19%:55%:21%:5% for EM1:EM2:EM3:EM4, respectively[58].

Due to the limited number of electronics channels, the resegmentation required that the two outer rings in θ ($\theta_{\text{bins}} 51$ and 52) have the four bins in φ ganged together to form two bins in φ identical to the two inner rings ($\theta_{\text{bins}} 55$ and 56). This reduced the effective number of towers per octant from 20 to 18. Because the Bhabha cross section falls so steeply with increasing θ , and since $\theta_{\text{bin}} 52$ is partially masked by inner components already ($\theta_{\text{bin}} 51$ only exists to catch the energy of showers with a centroid in $\theta_{\text{bin}} 52$ as the shower develops in the transverse plane), the impact of this new configuration on measuring small-angle Bhabhas for the luminosity measurement is insignificant. The older 20 tower segmentation is shown in Figure 4-20 and the newer 18 tower segmentation is shown in Figure 4-21.

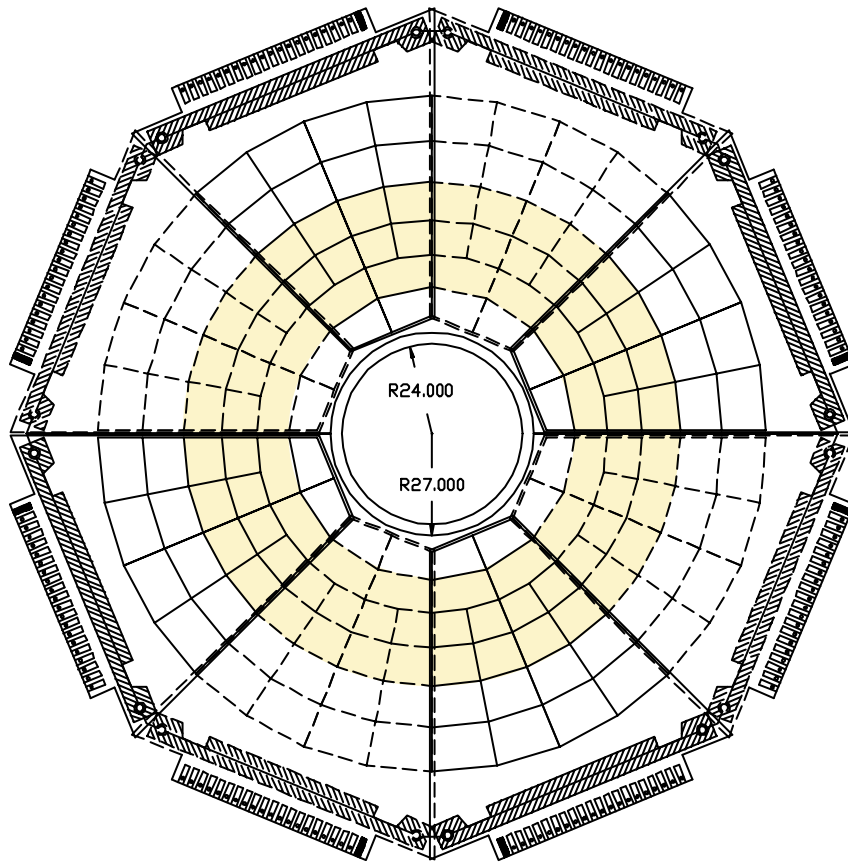


Figure 4-20 Transverse view of LUM before resegmentation. The LUM was in this configuration for all runs prior to 1996 (the so-called VXD2 era). The SLD calorimetry convention numbers towers in units of θ_{bin} . The inner ring of towers are all numbered $\theta_{\text{bin}} = 56$, with each tower decreasing one θ_{bin} unit with increasing polar angle. The outer ring is numbered $\theta_{\text{bin}} = 51$.

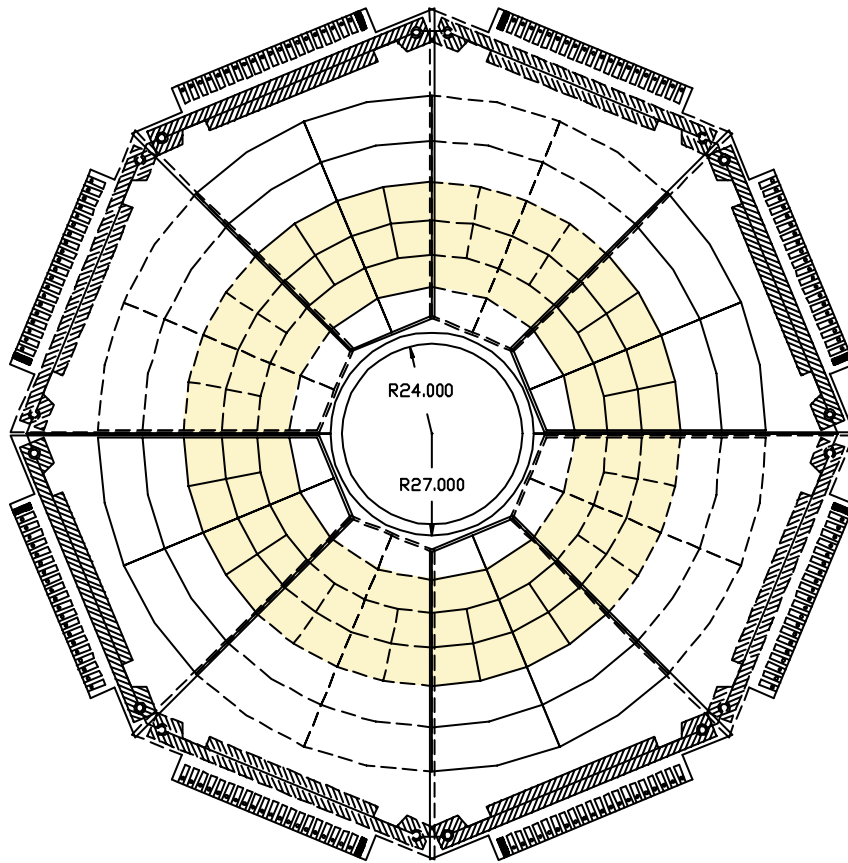


Figure 4-21 Transverse view of LUM after resegmentation. The LUM was in this configuration for the 1996 run and later (the so-called VXD3 era). Notice the double wide towers in the outer ring. The SLD calorimetry convention numbers towers in units of θ_{bin} . The inner ring of towers are all numbered $\theta_{\text{bin}} = 56$, with each tower decreasing one θ_{bin} unit with increasing polar angle. The outer ring is numbered $\theta_{\text{bin}} = 51$.

A typical small-angle Bhabha event from the 1998 run is shown in Figure 4-22. The top plot shows the North LUM module, and the bottom plot shows the South LUM module. The 45 GeV positron enters from the right in the top plot, strikes the upper part of the layer labeled North 0 (this is called layer EM1 in the text) and deposits all of its energy throughout the remaining layers (labeled North 1, North 2 and North 3, which are called respectively layers EM2, EM3 and EM4 in the text). The 45 GeV electron enters from the left in the bottom plot, strikes the lower part of the layer labeled South 0 (this is called layer

EM1 in the text) and deposits all of its energy throughout the remaining layers (labeled South1, South 2 and South 3, which are called respectively layers EM2, EM3 and EM4 in the text). Notice that the majority of the energy is well contained within 1 pad. The diffuse energy throughout the remainder of the detector is typical SLC background.

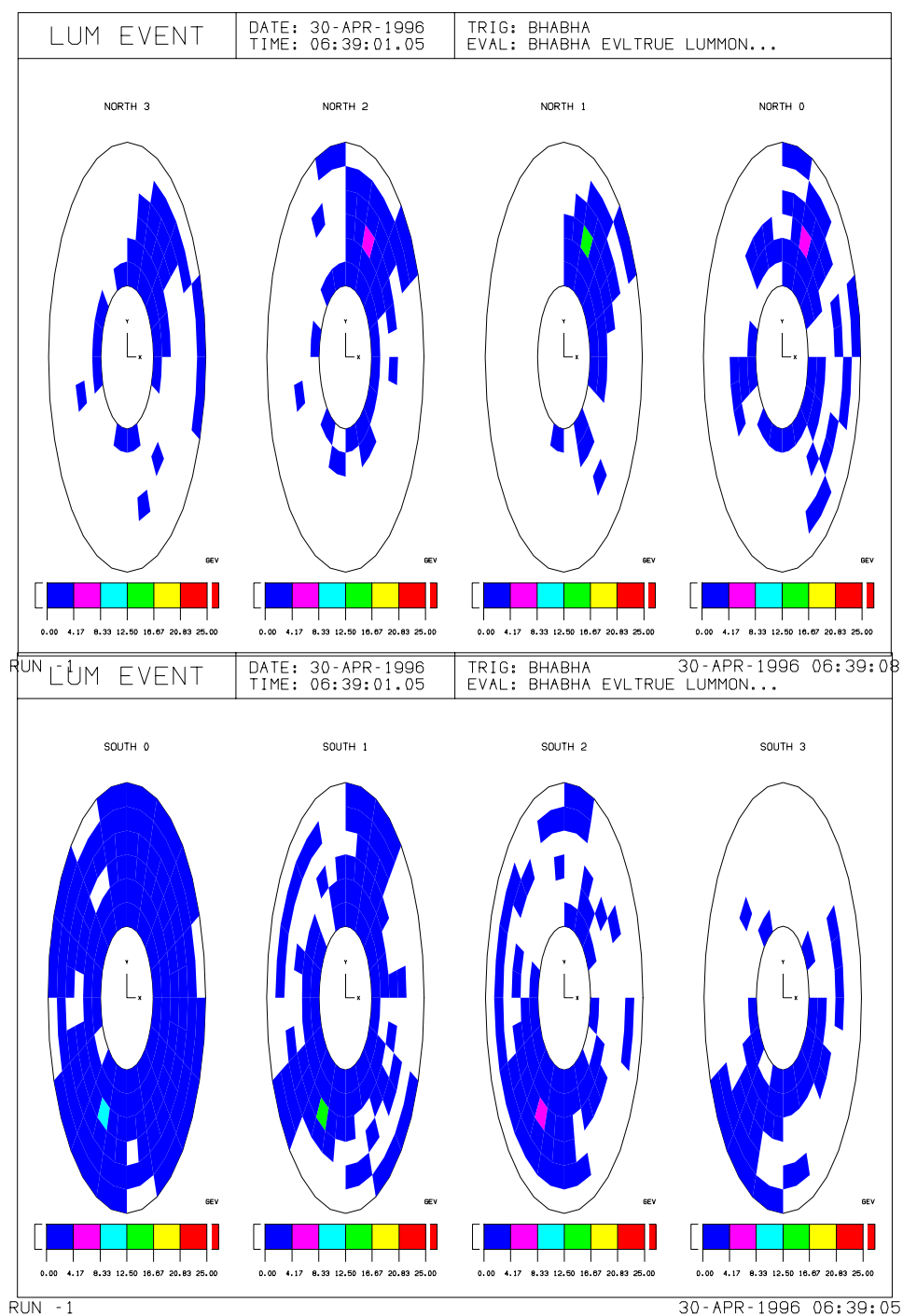


Figure 4-22 A typical small-angle Bhabha event from the 1998 run.

A total of 80 custom Kapton (polyimide) flex circuits were manufactured by Dynaflex Technology of San Jose, CA. Each flex circuit was a 9 layer design, incorporating 2 shield layers of silver ink which surrounded the 21 conductor signal layer. The conductors were 1 oz. copper, 8 mil traces on 16 mil centers. Each flex circuit was 50 cm in length and 1.7 cm wide except at the ends where connectors were soldered into place.

The only concern of the new Kapton flex circuits was the potential of capacitive crosstalk among nearest neighbor and next-to-nearest neighbor conductors. A detailed study showed that the crosstalk of the Kapton flex circuits was two orders of magnitude smaller than for the older ribbon cables[59].

An minor but unforeseen problem occurred during the initial installation of the Kapton flex circuits where a few of the cables would tear due to their transverse stiffness. These torn cables were easy to identify and replace with spares. Overall the Kapton flex circuits performed well and allowed known electronics problems (i.e. dead channels) to be associated with areas of the silicon-tungsten pads where their influence on measured quantities was minimized.

Electronics

Although the new Kapton cable plant offered the potential for measurement improvements for the luminosity analysis due to the greater information on shower depth, the primary motivation was to increase the robustness and reliability of the LUM electronics. The new Kapton cable plant had a much smaller footprint, better shielding and fewer connectors. The reliability was immediately obvious during the ensuing 1996 run when there were no new LUM problems during five SLD endcap door openings and closings of nearly

two years of running. There were four known dead channels out of the 1,024 total, which are listed in Table 4-3.

Table 4-3 Dead electronics channels in LUM before the CDC wire break (run 1996 through September 1997)

Side	Daughterboard	Channel	Layer	θ_{bin}	ϕ_{bin}
North	1	0	EM4	56	168
North	3	1	EM4	55	156
South	11	8	EM4	54	36
South	13	21	EM4	54	60

The new longitudinal segmentation allowed for all of these dead channels to be assigned to EM4 where their impact on measuring Bhabha events was insignificant since EM4 measures only 5% of the shower energy on average. The situation changed slightly in September of 1997 when the CDC suffered a wire break which forced SLD/SLC into an extended down period. During this time two cold solder joints on 1 CDU of South Daughterboard 14 were fixed, but this introduced two new dead channels, which made for a total of six dead channels. Because of the new Kapton cabling scheme it was again possible to move these two new dead channels to EM4. These six dead channels, which are listed in Table 4-4, persisted until the end of the 1998 run when the SLD data acquisition program officially ended.

Table 4-4 Dead electronics channels in LUM after CDC wire break (September 1997).

Side	Daughterboard	Channel	Layer	θ_{bin}	ϕ_{bin}
North	1	0	EM4	56	168
North	3	1	EM4	55	156
South	10	8	EM1	54	36
South	11	8	EM3	54	36
South	13	23	EM4	51	60
South	13	28	EM4	54	48

CHAPTER 5 LUMINOSITY MEASUREMENT

This chapter will describe the method of measuring luminosity at SLD, and will present the measurements for the 1993-1998 SLD datasets. Luminosity at SLD is measured with the LUM, which was described in section 4.2.6 above. We employ the same luminosity measurement procedure as described in [53], so a detailed description will not be repeated here. However, the important features of the general method will be described in this chapter in addition to detailed descriptions of those parts of the method which were unique or were improved in our analysis. In particular, several sources of systematic error from the earlier analysis were identified and improved. The LUM had an original design goal for a 3% relative systematic error [43], but through the previous analysis as well as our own it has been reduced to 0.76%.

5.1 Measuring Luminosity With Bhabha Scattering

All e^+e^- colliders measure luminosity using equation (4.1) by measuring the rate of small-angle Bhabha scattering ($e^+e^- \rightarrow e^+e^-$) for three main reasons:

1. The method is simple and straightforward. For any physics process $\nu = \mathcal{L}_{\text{Integrated}} \sigma$, where ν is the number of events, $\mathcal{L}_{\text{Integrated}} = \int \mathcal{L} dt$ is the integrated luminosity and σ is the cross section. By calculating the Bhabha scattering cross section σ for a detector and counting the number of events seen in the detector, the integrated luminosity is easily calculated. Therefore, measuring luminosity is in principle a

simple measurement relying only on identifying and counting electrons and positrons within a well-defined region.

2. The physics of small-angle Bhabha scattering is extremely well understood since it is almost entirely a QED process dominated by t-channel photon exchange, which means that the cross section σ can be calculated to extremely high precision.
3. The Bhabha scattering cross section increases rapidly as $\sim \frac{1}{\theta^3}$ for small polar angles near the beam line, making this cross section the dominate physics process in e^+e^- collisions. Therefore, Bhabha scattering allows for high-statistic measurements.

The SLD LUM was designed specifically to identify small-angle Bhabha scattered events and to provide precision energy and position measurements of the outgoing electron and positron. This process involves triggering on all Bhabha event candidates, identifying the Bhabha events from background and classifying the events for counting purposes. These will be covered in the following sections

5.2 Trigger

Since small-angle Bhabha scattering is dominated by t-channel photon exchange, the outgoing electron and positron from the elastic collision will each carry the full beam energy of 45 GeV and will be back-to-back with an acolinearity near zero. Initial and final state radiation modify this picture slightly, but the effects are small and easily accounted for in both the trigger and subsequent event selection criteria.

Since the LUM was designed to fully absorb the energy from an incident 45 GeV electron, the LUM trigger is in principle trivial. During the 1991 through 1993 SLD runs the

LUM trigger consisted of simple threshold suppressed energy sums for the total energy in each module. Experience in the earliest runs found that summing only EM2 towers above 1.25 GeV, and requiring a minimum of 12.5 GeV of energy in both the North and South module provided a trigger that was 99.6% efficient[60]. This trigger was calculated at 120 Hz on every SLC beam crossing, and was therefore dead-timeless.

Although this was an ideal physics trigger for finding Bhabha events and could run at the full SLC repetition rate, bad SLC beam conditions would occasionally blast the LUM with enough beam-related background that satisfied the trigger at a high enough repetition rate that the internal data acquisition buffers would fill and begin to drop events.

To Protect against this, a new trigger was implemented in 1994 with the same 1.25 GeV tower threshold, but the energy sums were formed only over ϕ wedges in EM2 that spanned $1/16^{\text{th}}$ (or 22.5° , which is two single-wide towers in ϕ as seen in Figure 4-20) of the transverse plane of the detector. The energy in each pair of adjacent wedges was summed to form an overlapping octant energy sum. The trigger would evaluate true if the sum of any octant energy sum in the North with the diametrically opposed octant in the South was above 12.5 GeV. This arrangement effectively imposed an acolinearity cut into the trigger, which was loose enough to accept all Bhabha events but stringent enough to reject most SLC beam related background since the background is uncorrelated in ϕ . The new trigger lead to a dramatic increase in purity with no loss in efficiency.

5.3 Event Selection

The Bhabha event selection criteria is basically a tightening of the trigger since the Bhabha events are very well separated from the background. The size of a typical

electromagnetic shower in the LUM is about 1cm^2 , which is about the size of a LUM tower in the transverse plane. Therefore, simple clusters are formed in each EM layer by combining the tower with the most energy with all of its nearest neighbors. Detailed studies with GEANT[61] and EGS4[57] showed that clusters of this size contained 90% of the electromagnetic shower energy on average.

Data for runs prior to 1996 used the two-layer LUM, which was comprised of layers EM1 and EM2. For the 1996 run and beyond the four-layer LUM was used which was comprised of layers EM1, EM2, EM3 and EM4. Because there was no overwhelming advantage in incorporating the extra information from the four layers, and since the Bhabha analysis technique and software package was mature and stable, the EM2, EM3 and EM4 layers were combined into an effective layer that mimicked the old EM2 layer. This allowed the Bhabha analysis for the entire SLD dataset to be treated in a consistent and simple way. In the following discussion, when we refer to EM2 we mean the effective EM2 which is comprised of EM2+EM3+EM4, and there will be no further mention of the physical EM2, EM3 and EM4 layers.

For each event there are four clusters, one in each layer (EM1 and EM2) in each module (North and South). The average positions $\bar{\theta}$ and $\bar{\phi}$ of the incident particle are calculated using simple energy weighted means. Both the EM1 and EM2 clusters are used to calculate these average positions unless they are separated by more than 6 towers in azimuth (or 67.5°), in which case only the EM2 cluster is used. This requirement simply requires that the EM1 and EM2 clusters form one logical cluster, since 6 towers in azimuth would represent a physically distinct cluster since clusters have a fixed shape that are 3×3 towers in size. Although it is possible to calculate more precise positions using detailed Monte Carlo simulations[62], it is unnecessary for our purposes as long as all pertinent cuts are placed

along tower boundaries where the position resolution is best (which is about 300 μm). Our intent is not to measure the Bhabha differential cross section $\partial_\theta\sigma$, it is simply to count Bhabha events within a well defined region.

The primary source of LUM background comes from a continuous profile of SLC electromagnetic radiation falling rapidly with radius from the beam line. To insure a highly pure Bhabha sample, clusters are rejected for EM1 clusters below 1.25 GeV and EM2 clusters below 2.50 GeV. Clusters which pass these cuts are then required to satisfy the following criteria

$$\begin{aligned} 20 \text{ GeV} < E_{\text{EM1+EM2}} < 125 \text{ GeV} \\ \left| \pi - (\varphi_{\text{North}} - \varphi_{\text{South}}) \right| < 0.5 \text{ rad.} \end{aligned} \tag{5.1}$$

Notice that there is no cut on the observable θ . The θ observable is used to classify events for the luminosity measurement technique to be presented next.

5.4 Classification

Since the Bhabha cross section is such a rapidly varying function of θ , small misalignments can have a large impact on the parts of the Bhabha cross section sampled by the two LUM modules. Therefore, to reduce the sensitivity of the luminosity measurement on calorimeter alignment we make use of the gross-precise method[63-66]. This method logically divides each LUM module into a tight *precise* region and a looser *gross* region. The regions are defined along tower boundaries where the position resolution is best. Referring to Figure 4-21, the innermost ring ($\theta_{\text{bin}} = 56$) and the two outermost rings ($\theta_{\text{bin}} = 52, 51$) define the gross region. The central shaded rings with $\theta_{\text{bin}} = 55, 54, 53$ define the precise

region. Events where both the North and South cluster are in the precise region are classified as precise events. Events where one cluster is in the precise region and the other is in the gross region are labeled gross events. Other events where both clusters are in the gross region are not used for the luminosity analysis, but this does not mean the event is not a Bhabha.

Using this classification scheme, precise events are given a weight of 1 and gross events are given a weight of $\frac{1}{2}$, and an effective number of events is defined as

$$n_{\text{eff}} = n_{\text{precise}} + \frac{1}{2} n_{\text{gross}} \quad (5.2)$$

The power of the gross-precise method is that the number of effective Bhabhas given by equation (5.2) is a constant for small displacements. For the LUM this means transverse displacements as much as 2 mm and displacements along the z-axis as much as several centimeters are possible while still keeping n_{eff} constant. This can be understood qualitatively by observing that any misalignment causes a net loss of precise events and a net gain of gross events.

5.5 Accounting

The number of precise and gross Bhabhas for the various SLD run periods are listed in Table 5-1. The accounting is broken down into consecutive blocks of runs that were treated separately due to potentially significant changes in running conditions and LUM configurations where the Bhabha cross section sampled by the LUM may be different. The accounting is also broken down according to the polarization of the electron beam, which is important for measuring the left and right-handed luminosity used in the measurement of

\bar{g}_V^e and \bar{g}_A^e presented in Chapter 7 below. The number of effective Bhabha events, n_{eff} for each SLD run period are listed in Table 5-2.

Table 5-1 Number of precise and gross Bhabha events for each SLD run period as measured by the LUM. The number of events are listed separately according to the polarization of the electron beam for the event; Left means left-handed polarization, Right means right-handed polarization.

Name	Description	Precise Left	Gross Left	Precise Right	Gross Right
1993 Run		54,875	9,169	55,406	9,115
1994 Run	pre-September	17,369	3,237	17,367	3,188
1994 Run	Fall: before LUM noise period	26,177	4,571	26,191	4,768
1994 Run	Fall: during LUM noise period	1,898	321	1,918	316
1994 Run	Fall: after LUM noise period	27,694	4,725	28,102	4,651
1995 Run		35,057	6,452	35,273	6,488
1996 Run	before R20 translation #1	1,919	351	1,806	362
1996 Run	during R20 translation #1	14,077	2,775	14,034	2,723
1996 Run	during R20 translation #2	32,888	6,692	32,486	6,573
1996 Run	during R20 rotation #1	7,821	1,570	7,751	1,651
1997 Run		113,543	24,620	114,968	24,725
1998 Run	before off-energy Z-peak scans	171,890	36,115	171,393	36,401
1998 Run	after Z-peak scan	78,814	16,912	78,747	16,634

Table 5-2 Number of effective Bhabhas for each SLD run period for left-handed beams and right-handed beams.

Year	Effective LUM Bhabhas	
	Left	Right
1993	59,459.5	59,963.5
1994	79,565.0	80,039.5
1995	38,283.0	38,517.0
1996	62,399.0	61,731.5
1997	125,853.0	127,330.5
1998	277,217.5	276,657.5

5.6 Cross Section Calculation

The cross section for small-angle Bhabha scattering into the LUM is calculated from simulating electromagnetic showers from Monte Carlo event generators which model the small-angle Bhabha scattering process. Although small-angle Bhabha scattering is based on the well known physics of QED, radiative corrections modify the tree level differential cross section by a few percent. Therefore, special precision Monte Carlo generators which take into account these higher order corrections have been written specifically for the cross section calculations required to measure luminosity at e^+e^- colliders. We use two Monte Carlo generators for consistency cross checks, BHLUMI[67, 68] and BABAMC[69]. The BABAMC generator includes only single photon Bremsstrahlung in the initial and final state. Two versions of BHLUMI were used, version 2.01[67] uses the Yennie-Frautschi-Saura (YFS) $O(\alpha)$ exponentiation, and version 4.04[68] which improves on version 2.01 by including missing second-order leading-logarithmic (LL) corrections and QED corrections to the Z^0 contribution. BHLUMI 2.01 quotes an overall precision of 0.25% and BHLUMI 4.04 quotes an overall precision of 0.11%.

The BABAMC generator was used simply for a consistency cross check of BHLUMI 2.01, and we found the two generators to agree within 0.1%. BHLUMI 2.01 was used to calculate the cross section for the 1993-1995 run periods and BHLUMI 4.04 was used to calculate the cross sections for the 1996-1998 run periods.

Events from the Monte Carlo generators are simulated with GEANT[61] using parameterized electromagnetic showers based on GFLASH[70]. Parameterization of electromagnetic showers is necessary because of the time consuming nature of full shower simulations, which took about an hour per event at the time this dissertation was written.

Everything that is known about the configuration of the real LUM and the running conditions are put into the simulation, including actual beam energies, beam energy uncertainties, beam energy widths, position and variation of the interaction point, known dead channels in the LUM electronics and masking of the LUM by inner beam line components.

The simulated Monte Carlo events are passed through the same Bhabha filter used for the data, the number of precise and gross events are tabulated and the effective number of events n_{eff} is calculated according to equation (5.2). An effective cross section is then defined according to the formula

$$\sigma_{\text{eff}} \equiv \frac{n_{\text{eff}}}{n} \sigma_{\text{MC}} \quad (5.3)$$

where n is the number of events generated by the Monte Carlo generator and σ_{MC} is the cross section calculation of the event generator. The quantity σ_{eff} is the cross section for small-angle Bhabha scattering into the two LUM modules, and will be used in section 5.7 below for calculating integrated luminosity.

During the course of SLD's data acquisition history careful records were kept of changes in running conditions and LUM periods which could have affected the luminosity measurement. These run blocks are listed in Table 5-3, which list the beginning and ending run numbers for each block and the effective cross section σ_{eff} for small-angle Bhabha scattering into the LUM.

Table 5-3 SLD Run blocks of significant note throughout SLD's data acquisition history. Listed are the beginning and ending run numbers for each block and the effective cross section σ_{eff} for small-angle Bhabha scattering into the LUM.

Name	Description	Begin Run Number	End Run Number	Cross Section
1993 Run		15807	23700	66.748
1994 Run	pre-September	26844	28187	60.42544
1994 Run	Fall: before LUM noise period	28518	29407	66.748
1994 Run	Fall: during LUM noise period	29455	29494	66.748
1994 Run	Fall: after LUM noise period	29518	30077	66.748
1995 Run		30320	31226	66.748
1996 Run	before R20 translation #1	33383	33445	67.307
1996 Run	during R20 translation #1	33446	34267	67.307
1996 Run	during R20 translation #2	34268	35253	67.307
1996 Run	during R20 rotation #1	35254	35522	67.307
1997 Run		37418	40724	67.307
1998 Run	before off-energy Z-peak scans	41098	43153	67.307
Z-peak scan	on peak	42786	43153	67.307
Z-peak scan	high energy point	43166	43202	
Z-peak scan	low energy point	43203	43258	
1998 Run	after Z-peak scan	43269	43934	67.307

5.7 Integrated Luminosity Measurement

Actually calculating the integrated luminosity is a straightforward process once the Bhabha events are properly identified and counted and the cross section for Bhabha scattering into the LUM σ_{eff} is calculated. The formula for calculating integrated luminosity is given by

$$\mathcal{L}_{\text{Integrated}} \equiv \int \mathcal{L} dt = \frac{n_{\text{eff}}}{\sigma_{\text{eff}}} \quad (5.4)$$

Using this formula, the total integrated luminosity for all run periods is measured by calculating the effective number of Bhabha events n_{eff} for each run block listed in Table 5-3

using equation (5.2) and the precise and gross event counts in Table 5-1, and the effective cross sections σ_{eff} listed in Table 5-3. The total integrated luminosity for all run periods is given in Table 5-4. The total systematic error for the luminosity measurement is 0.76%, and the various contributions to this error will be presented in section 5.8.

Table 5-4 Total integrated luminosity measurements for each SLD run period for left-handed electron beams, right-handed electron beams, and the total integrated luminosity (the sum of the two previous columns). The error on each measurement is the combined statistical error and systematic error. The systematic error is fixed at 0.76% for each run period and helicity except for a small part of the 1994 run which is treated separately in the text..

Run Period	Integrated Luminosity (inverse nanobarns)		
	Left	Right	Total
1993	891 \pm 8	898 \pm 8	1,789 \pm 15
1994	1,222 \pm 10	1,229 \pm 10	2,451 \pm 20
1995	574 \pm 5	577 \pm 5	1,151 \pm 10
1996	927 \pm 8	917 \pm 8	1,844 \pm 15
1997	1,870 \pm 15	1,892 \pm 15	3,762 \pm 30
1998	4,130 \pm 32	4,121 \pm 32	8,251 \pm 64
Total	9,613 \pm 74	9,634 \pm 74	19,247 \pm 147

5.8 Systematic Errors

A detailed study and description of the LUM systematic errors appears in [53, p. 81-97] and will not be repeated here. However, since the aforementioned study of systematic errors was performed only for the early 1992 SLD data, we identified those sources of systematic error that we believed either would have changed for the later data presented in this dissertation, or that could be improved. The complete list of LUM systematic errors appears in Table 5-5; the first column lists the original systematic error

measurements from[53], while the second column lists the systematic errors used in this dissertation, some of which were reanalyzed and updated.

As can be seen in Table 5-5 below, the major source of LUM signal contamination comes from SLC beam related background in the form of electromagnetic radiation. To measure this effect, events were selected which passed all LUM Bhabha cuts except for the cut on the opening angle between the North and South clusters, and of these events only those which have an opening angle near zero radians (instead of π radians) are tagged as beam related contamination. As noted in[53], this method of estimating the SLC beam background is actually an overestimate of the effect since the background events are correlated. We ran the LUM Bhabha filter MBHFLT[71] with its default set of cuts, but with the modified opening angle cut as described above, on the entire 1993 SLD raw triggers and found 14 precise-precise events and 214 gross-precise events that passed the LUM Bhabha cuts, which corresponds to 121 effective LUM Bhabhas. Since there were 119,488 actual LUM Bhabhas in this dataset¹⁸, we estimate the beam background to be $121/119,488 = 0.101\%$. The same exercise was run on smaller samples of the SLD raw triggers for later runs which found similar results. For simplicity we take the 0.101% as the size of the systematic error due to beam related background. It should be noted that applying the 0.101% as a correction to the data instead of assigning it as the systematic error is another possibility which would potentially lower the error due to beam related background. However, this would have required running the modified Bhabha filter on all SLD raw data tapes which was unfeasible due to the large number of raw data tapes.

¹⁸ The 119,488 LUM Bhabha events for the 1993 run period differs from 119,423 as listed in Table 5-2 because the so-called *default cuts* were used instead of the *analysis cuts*. The default cuts are a looser set of cuts from the original MBHFLT Bhabha filter software package[71] The analysis cuts are a slightly tighter set of cuts used for the precision luminosity measurement.

The theoretical uncertainty for the small-angle Bhabha event generator BABMC, written by Berends, Hollik and Kleiss[72], is 0.5%. As already noted the BHLUMI small-angle Bhabha event generators had theoretical uncertainties of 0.25% and 0.11% for version 2.01 and version 4.04, respectively, and the BABAMC event generator was found to agree with the BHLUMI 2.01 generator to within 0.1%. For the simplicity of having one global systematic error for the LUM measurement, we conservatively estimate the theoretical uncertainty of the Monte Carlo event generators as the simple average of the individual theoretical uncertainties, which is 0.3%.

Finally, the smallest dataset of simulated Monte Carlo events passed through the LUM Bhabha filter found 226,082 precise events and 33,492 gross events, which corresponds to 242,828 effective LUM Bhabhas. The statistical error for this dataset is therefore 0.196%. All of these improvements are listed in column 2 of Table 5-5 below.

Table 5-5 Luminosity measurement systematic error contributions. The first column lists the systematic errors originally calculated in [53] for the 1992 SLD run periods. The right column lists the systematic errors for the later SLD run periods, 1993-1998.

Systematic Error Source	Systematic Error	
	Original	Updated
contamination from $e^+e^- \rightarrow e^+e^-X$	0.010%	0.010%
contamination from $e^+e^- \rightarrow \gamma\gamma$	0.050%	0.050%
contamination from $e^+e_{L,R}^- \rightarrow Z^0 \rightarrow e^+e^-$	0.001%	0.001%
contamination SLC background	0.320%	0.101%
energy scale uncertainty	0.170%	0.170%
125 GeV upper energy cut	0.020%	0.020%
tower-to-tower calibration effects	0.220%	0.220%
dead towers between calibrations	0.050%	0.050%
E_{cm} uncertainty and E_{cm} spread.	0.080%	0.080%
e^+ energy asymmetry	0.060%	0.060%
IP position uncertainty	0.030%	0.030%
finite beam crossing angle	0.060%	0.060%
Monte Carlo generator technical precision	0.100%	0.100%
Mote Carlo theoretical uncertainty	0.500%	0.300%
Monte Carlo statistics	0.500%	0.196%
GEANT/GFLASH simulation accuracy	0.430%	0.430%
snout modeling uncertainty	0.004%	0.004%
uncertainty in not modeling pseudo-projective towers	0.190%	0.190%
1mm IP offset due to θ cut uncertainty	0.080%	0.080%
LUM module misalignment in transverse plane	0.085%	0.085%
uncertainty in distance between triplets	0.300%	0.300%
Total	1.019%	0.759%

CHAPTER 6 WIDE-ANGLE BHABHA EVENT SELECTION

The wide-angle Bhabha (WAB) events used in this analysis are measured solely by the SLD LAC calorimeter subsystem. We begin the chapter by describing the entire SLD data-flow starting from an individual beam crossing and follow the data through the LAC digitization and readout process, the Energy Trigger and other downstream filter processes, and the reconstruction of the raw data into physical observables suitable for interactive data analysis. Next, the selection criteria that separate wide-angle Bhabha events from other physics processes and sources of background are described. Finally, the procedure to correct the final selection of WAB events for effects such as detector inefficiencies and contamination by other physics processes is described. The pseudo-event method is presented and described in some detail, which we use to overcome the limitations of the GEANT[61] software simulation of the SLD detector.

6.1 The Data Acquisition Phase

The data-flow of the SLD experiment is logically and physically broken into two steps; the data acquisition on a per beam-crossing basis handled by the Below Line¹⁹ subsystem, followed by an event reconstruction and post-analysis process handled by the

¹⁹ The so-called Below Line is really the SLD Data Acquisition subsystem that is responsible for directly reading out digitized data from the entire SLD detector, calculating trigger quantities, acting on this trigger information, and finally handing the data off to the so-called Online subsystem for writing the data to magnetic tape. Most experiments have just a single Online subsystem that subsumes all of these responsibilities, but the SLD physicists responsible for the data acquisition drew a clear line of distinction between their domain, which was electronics focused, and the rest of the Online subsystem, which was software focused, and coined the term “Below Line” to make explicit this subversive distinction[73]

Offline subsystem. Although the entire SLD Data Acquisition Subsystem is a fascinating topic in and of itself, the current chapter will describe only those parts of the data acquisition that pertains to the SLD LAC calorimeter.

The analog signal of each LAC Tower is digitized on every SLC beam crossing (120 Hz) and the resulting ADC values are stored by a set of custom FastBUS[52] modules, named Calorimeter Data Modules or CDMs[74] for short. The CDMs store the entire KAL data in memory while also calculating the quantities used by the SLD Energy Trigger. If the criteria of the Energy Trigger are satisfied, the CDMs forward their ADC data to a robotic tape silo where the data is written to magnetic tape.

The design of any trigger should be as efficient as possible for capturing any relevant physics information while rejecting as much as possible all forms of background noise. The SLD Energy Trigger is no different, and its sole purpose is to reject bad beam pulses and SLC muon background showers in order to reduce the amount of data written to tape to as low a value as possible while maintaining the full fidelity of any potential physics information which the SLD detector was designed to measure.

The CDMs form two energy sums named E_{LO} and E_{HI} , which are simple sums over all LAC towers subject to two simple threshold values,

$$\begin{aligned} E_{LO} &= \sum_{i=1}^{n_{LO}} E_i^{layer} > E_{\text{electronics noise}} = 8 \text{ ADC for EM, } 12 \text{ ADC for HAD} \\ E_{HI} &= \sum_{i=1}^{n_{HI}} E_i^{layer} > E_{\text{mip}} = 60 \text{ ADC for EM, } 120 \text{ ADC for HAD} \end{aligned} \quad (6.1)$$

Here n_{LO} and n_{HI} are the number of towers with energy above $E_{\text{electronics noise}}$ and E_{mip} , respectively. The value $E_{\text{electronics noise}}$ is set just above the ambient electronic noise and is

therefore chosen empirically, although it is clear that it will depend on the size of a KAL tower because electronics noise is proportional to capacitance, and capacitance is proportional to a tower's area, as defined by the lead tiles, divided by the gap distance between the lead tiles and lead plates. This is why $E_{\text{electronics noise}}$ has different values for the EM and HAD sections of the LAC, with the value for the HAD sections being larger. The value of E_{mip} is chosen to be just above the energy of a minimum ionizing particle, and is designed to reject the background muons generated by the SLC beams scraping beamline components on their way to the IP.

The conversion from ADC to energy for the LAC is 524 MeV/128 ADC for the EM1 and EM2 sections, and 1384 MeV/128 ADC for the HAD1 and HAD2 sections, and is the energy scale for a minimum ionizing particle (mip). The mip energy scale is used consistently throughout this dissertation, meaning that no e/μ correction factor is applied. All quoted energies, and all plots involving energy, use the mip energy scale. For example, any plot that involves energy on an axis will appear “low” compared to an absolute energy scale.

The SLD Energy Trigger is designed to be a general-purpose physics trigger, and is implemented using a simple energy threshold requiring $E_{\text{HI}} > 12 \text{ GeV}$ and $n_{\text{LO}} < 1000$. These two thresholds simply require that there be enough energy in the calorimeter in not too many towers so that the energy is somewhat localized to specific regions of the detector and not so diffuse as to be SLC beam related noise. When this trigger condition is satisfied all towers above 2 ADC in EM1, 3 ADC in EM2 and 6 ADC in HAD1 or HAD2 are written to tape. For WAB events the trigger is nearly 100% efficient, since a WAB event contains no invisible energy and will deposit nearly the entire center-of-mass energy into a few localized regions of the LAC.

6.2 The Pass 1 Filter

The entire reconstruction phase is broken up into a pipeline of several independent passes that collectively reads the raw ADC values from magnetic tape and performs several filtering and data reduction passes to reduce the raw data into a manageable form more convenient for interactive data analysis. These passes are not unique to the WAB events, and are simply general-purpose physics filters designed to reduce the amount of data that is attributable to background noise.

The first of these filters is called Pass 1, and is simply a more restrictive application of the ideas behind the Energy Trigger. The real-time nature of the data-acquisition environment where the Energy Trigger is applied demands a very loose set of requirements since there will not be an opportunity to revisit an event again if it is not written to tape. During offline processing we can be more discriminating, since if we later discover that our filtering procedures are wrong, we can simply fix the problem and rescan the raw data tapes. The energy and tower count thresholds used for the Pass 1 filter are given in equation (6.2).

$$\begin{aligned}
 E_{\text{LO}} &< \begin{cases} \frac{2}{3}E_{\text{HI}} + 70 \text{ GeV} \\ 140 \text{ GeV} \end{cases} \quad \text{whichever quantity is less} \\
 E_{\text{HI}} &> 15 \text{ GeV} \\
 n_{\text{HI}}^{\text{EM layers}} &> 10
 \end{aligned} \tag{6.2}$$

The new ideas here beyond the requirements of the Energy Trigger are that the energy is even more localized to specific regions of the calorimeter (as specified by the threshold on E_{LO}), and at least some of the energy must come from electromagnetic particles (which is specified by the threshold on $n_{\text{HI}}^{\text{EM layers}}$).

6.3 The Pass 2 Filter

Events that satisfy the Pass 1 filter are pipelined to the Pass 2 filter where the raw data is reconstructed into physics observables. It is in this filter that derived quantities are calculated and pattern recognition algorithms come into play. As a particle enters the LAC it will begin to interact and create secondary particles, which in turn cascades into yet more particles. This process is called showering, of which there are two types; electromagnetic showers caused by radiating electromagnetic particles, and hadronic showers caused by interacting hadrons. In our case we are concerned only with electromagnetic showers, since Bhabha scattering only involves electrons and positrons in the final state. The dimensions of these electromagnetic showers are extremely well contained, being almost pencil-like in shape and size.

Collections of LAC towers with energy above the thresholds given in Table 6-1 and physically adjacent to one another are grouped together and identified as a cluster. These clusters are three-dimensional entities that span adjacent towers in each layer and extend over each of the four calorimeter layers EM1, EM2, HAD1 and HAD2. The idea is to associate each cluster with a single incident particle, although due to fluctuations within each shower and the inherent energy resolution of the LAC it is sometimes necessary to merge clusters in order to associate the properties of a cluster with a specific incident particle. For example, tracking information can be used to associate a group of clusters as belonging to a single track.

As show in Table 6-1, the LAC tower ADC thresholds were lowered for the 1996-1998 run period compared to the 1994-1995 run period. The reason was to increase the efficiency of associating CDC tracks with LAC clusters, since the lower ADC thresholds

allowed more LAC clusters to be identified. Although tracking information is not used in this analysis, the lower tower thresholds produce an explosion in the number of clusters per event compared to the 1994-1995 run period that could potentially affect a WAB analysis. As will be show in section 6.4 below, the WAB selection criteria are designed to take this increased number of clusters into account.

Table 6-1 LAC tower thresholds for readout by the CDMs.
LAC towers below these ADC values are completely ignored by the Pass 2 filter and any further processing.

Run Year	ADC Thresholds			
	EM1	EM2	HAD1	HAD2
1994 - 1995	7	7	7	9
1996 - 1998	2	3	6	6

Each cluster is assigned six derived quantities: two angular coordinates $\cos\theta$ and ϕ , and the energy sums in each of the four LAC layers of the towers comprising the cluster. For simplicity, the two angular coordinates, $\cos\theta$ and ϕ are calculated as simple energy-weighted mean values of the absolute positions of the LAC towers.

6.4 Wide-Angle Bhabha Event Selection Criteria

At this stage in the processing, we have, for each event, a collection of calorimeter clusters which we need to analyze to determine if the event was due to Bhabha scattering. The method for identifying WAB events makes use of the fact that all of the final state particles for each event are electromagnetic, and therefore deposit the majority of the center-of-mass energy into the electromagnetic section of the calorimeter. Additionally, there will

be exactly one electron, one positron, and relatively few photons²⁰, if any, in the final state. Since this analysis uses only calorimeter information, it is not known which particle is associated with which cluster²¹. However, the order α^2 Monte Carlo we use in this analysis shows that the electron and positron will be the two most energetic clusters in the event more than 99% of the time, and that these two clusters will have an acolinearity near zero, meaning that they are nearly back-to-back. It is this last observation that makes the identification of WAB events easily separable from non-Bhabha physics processes and other sources of background.

Briefly, the selection criteria that follow identify events with relatively few clusters (but at least two) which deposit most of their energy in the electromagnetic section of the calorimeter, and where the two highest energy clusters are nearly back-to-back and contain the majority of the center-of-mass energy.

6.4.1 Cluster Quality Cuts

First, a subset of the original cluster list is selected by imposing the following cluster quality cuts:

$$\begin{aligned} E_{\text{EM1+EM2}} &> 0 \text{ GeV} \\ E_{\text{Total}} &> 1 \text{ GeV} \end{aligned} \tag{6.3}$$

²⁰ As will be shown in the following sections, the order α^2 Bhabha Monte Carlo we use in this analysis shows that 92% of the time there are only two clusters in the final state that pass all of our selection criteria.

²¹ It may be possible to determine whether a cluster is associated with the electron or positron from the curvature of the CDC track(s) associated with the cluster, since each particle's transverse component of momentum to the magnetic field will cause them to bend in opposite directions due to their opposite electric charges.

These very loose energy requirements simply reject clusters that are due to known background sources with negligible impact on the WAB signal. The benefit of the cluster quality cuts is that the number of clusters per event is greatly reduced, as well as outright rejecting anywhere between 15% and 30% (depending on the beam conditions of a given run) of the original set of events due to their being less than two clusters in the event.

Figure 6-1 and Figure 6-2 show the distribution of clusters before (above) and after (below) imposing the cluster quality cuts given in equation (6.3) on the raw data for the 1994 through 1995 runs (the VXD2 era) and the 1996 through 1998 runs (the VXD3 era). No other selection criteria have been applied other than there are at least two clusters in the event. Notice that the cluster quality cuts make no difference when the higher tower thresholds were used in the 1994 through 1995 era (see Figure 6-1), but that the cuts make a tremendous difference for the later runs (see Figure 6-2). Following the cluster quality cuts, the data samples for each era are similar, and therefore the same cuts can be applied in the subsequent analysis.

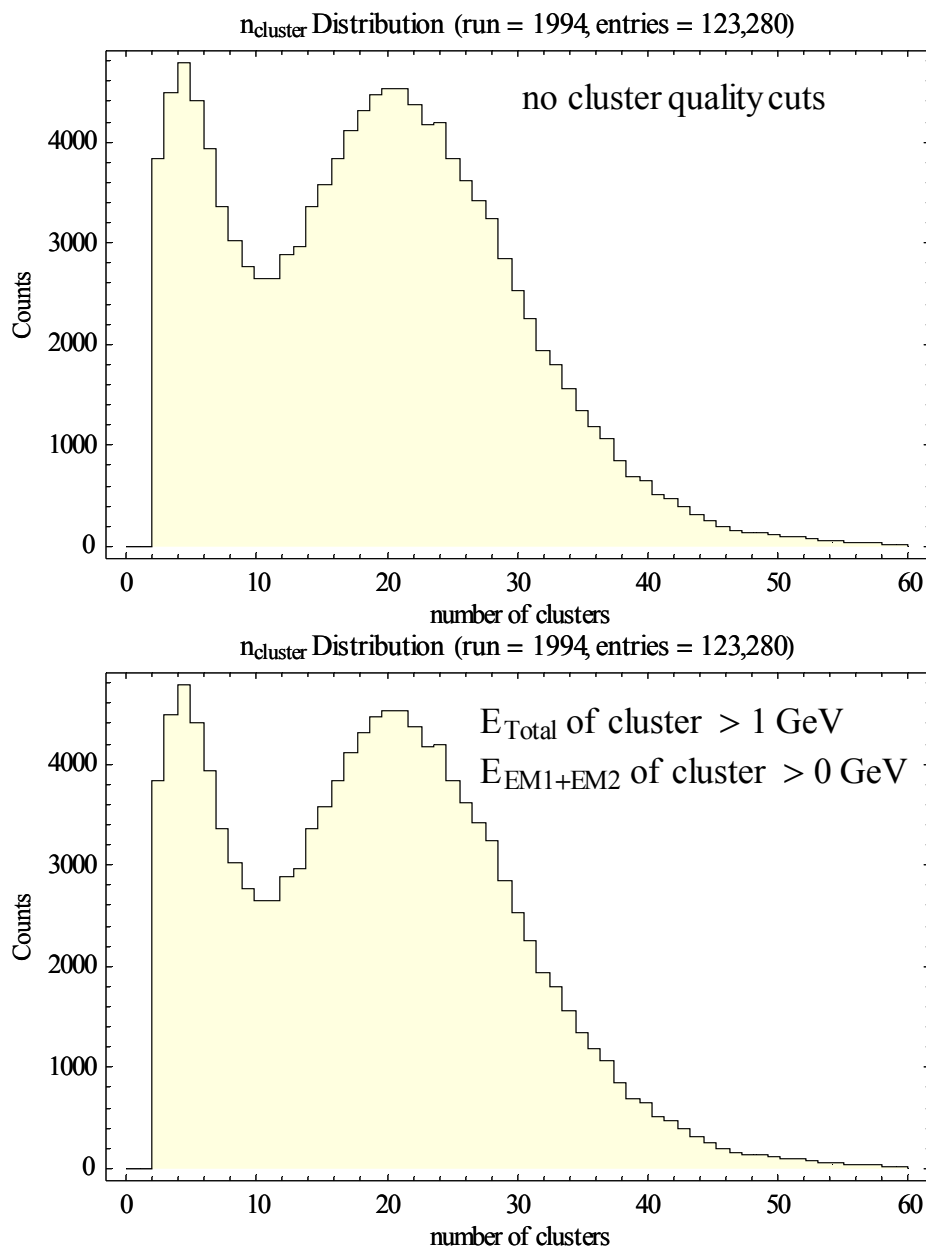


Figure 6-1 Number of clusters present before (above) and after (below) the cluster quality cuts in equation (6.3) for the 1994 run, which is representative of all 1994-1995 data (this is the VXD2 era). No other criteria have been applied other than there are at least two clusters in the event. There are no differences between the two plots, as expected.

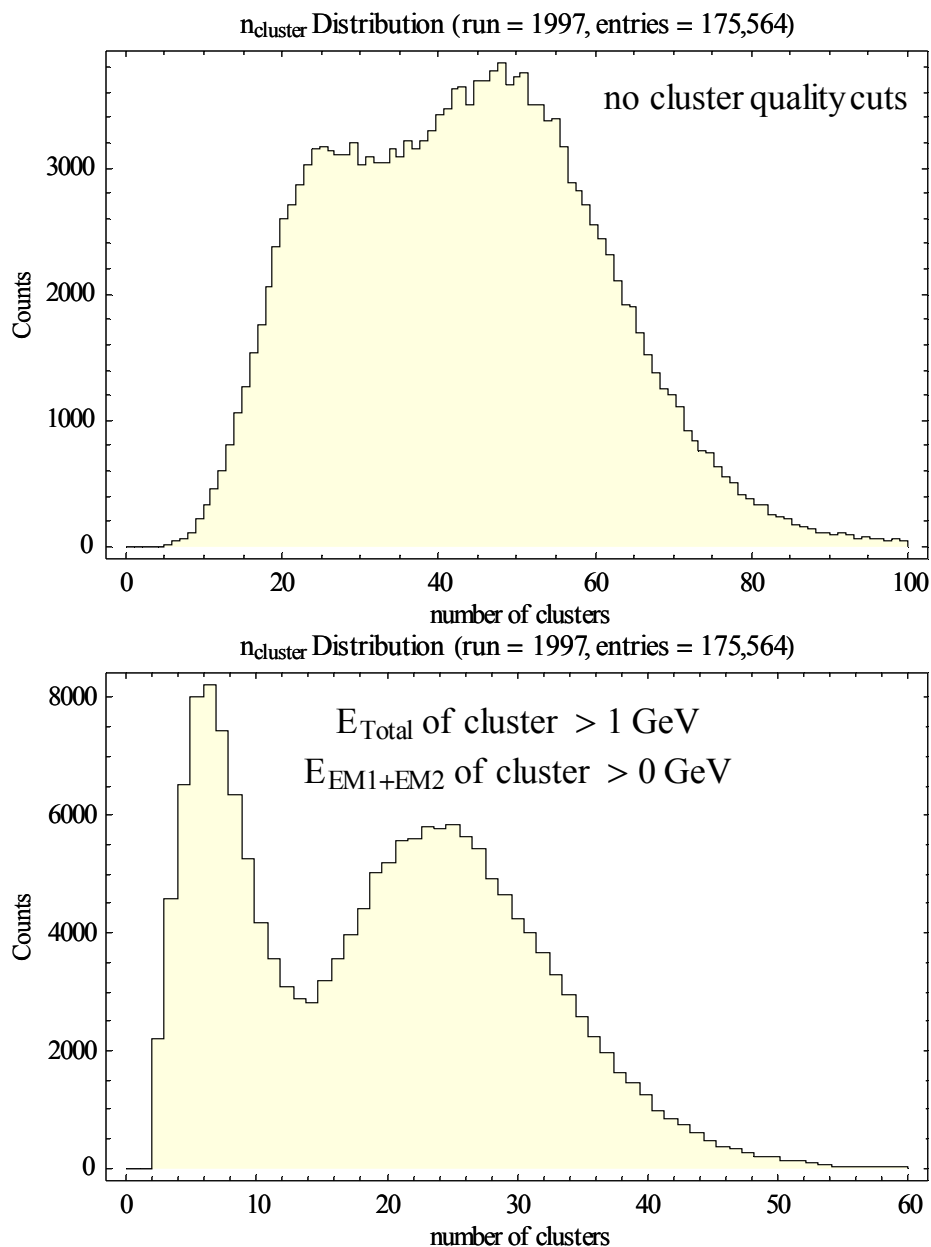


Figure 6-2 Number of clusters present before (above) and after (below) the cluster quality cuts in equation (6.3) for the 1997 data, which is representative of all 1996-1998 data (this is the VXD3 era). No other criteria have been applied other than there are at least two clusters in the event. Comparing the bottom plot to the plots in Figure 6-1 shows that the cluster quality cuts establish distributions which are similar for the two eras.

6.4.2 Cluster Energy Cuts

From the Unibab Monte Carlo[19] generator we know that over 99% of the time the two highest energy clusters will be the final state electron and positron. We therefore place the following stringent energy requirements on these two clusters:

$$\begin{array}{ll}
 E_{\text{EM1+EM2}}^{\text{cluster 1}} > 10 \text{ GeV} & E_{\text{EM1+EM2}}^{\text{cluster 2}} > 10 \text{ GeV} \\
 E_{\text{HAD1}}^{\text{cluster 1}} < 3 \text{ GeV} & E_{\text{HAD1}}^{\text{cluster 2}} < 3 \text{ GeV} \\
 E_{\text{HAD2}}^{\text{cluster 1}} < 0.5 \text{ GeV} & E_{\text{HAD2}}^{\text{cluster 2}} < 0.5 \text{ GeV}
 \end{array} \tag{6.4}$$

These selection criteria demand that these two highest energy clusters deposit the majority of their energy into the EM sections of the LAC, with any energy leaking into the HAD sections falling off rapidly with depth.

The distributions for this set of selection criteria are shown in Figure 6-3 (for the highest energy cluster) and Figure 6-4 (for the second highest energy cluster). For each plot, the selection criterion for the plotted quantity has not been applied. For example, the plot of the EM energy for cluster 1 (the top plot of Figure 6-3) does not include the requirement that $E_{\text{EM1+EM2}} > 10 \text{ GeV}$, but it does include the requirements of the other five selection criteria listed in equation (6.4).

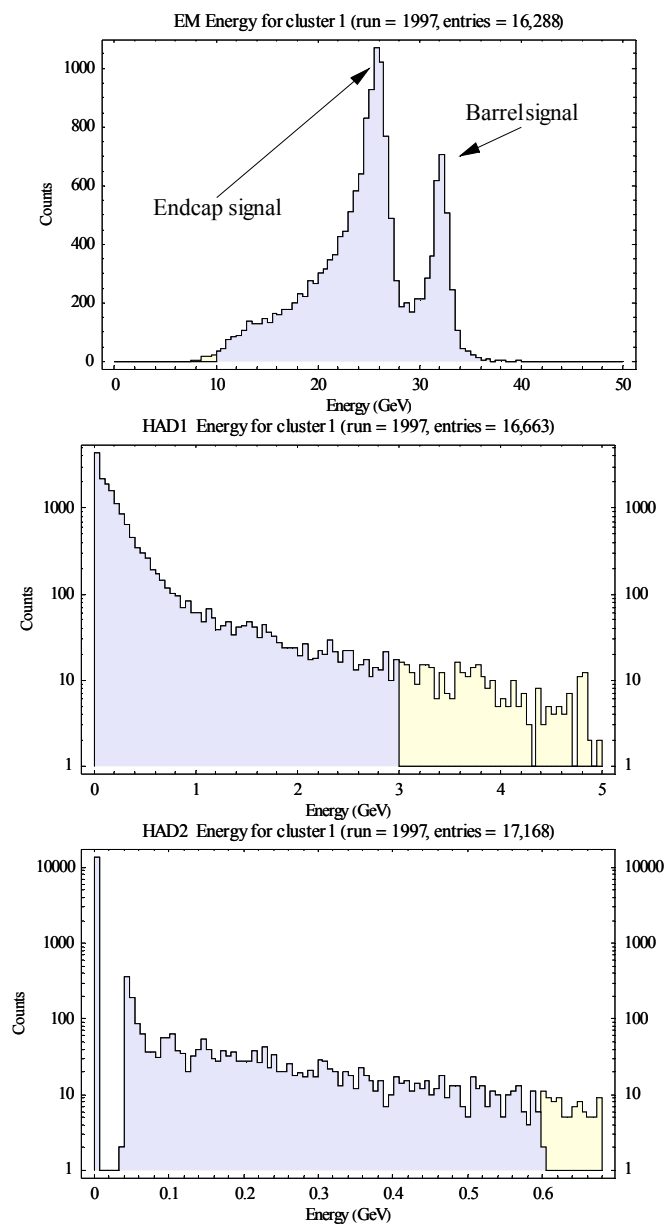


Figure 6-3 Cluster energy cuts for the highest energy cluster. The only criteria applied to select events in each plot are the cluster quality cuts of equation (6.3) and five of the six criteria in equation (6.4), the missing criterion being the quantity actually plotted so that it is clear which events are being discarded by the cut (accepted events appear in the darker shaded region). Data is from the 1997 run and is representative of the entire SLD dataset.

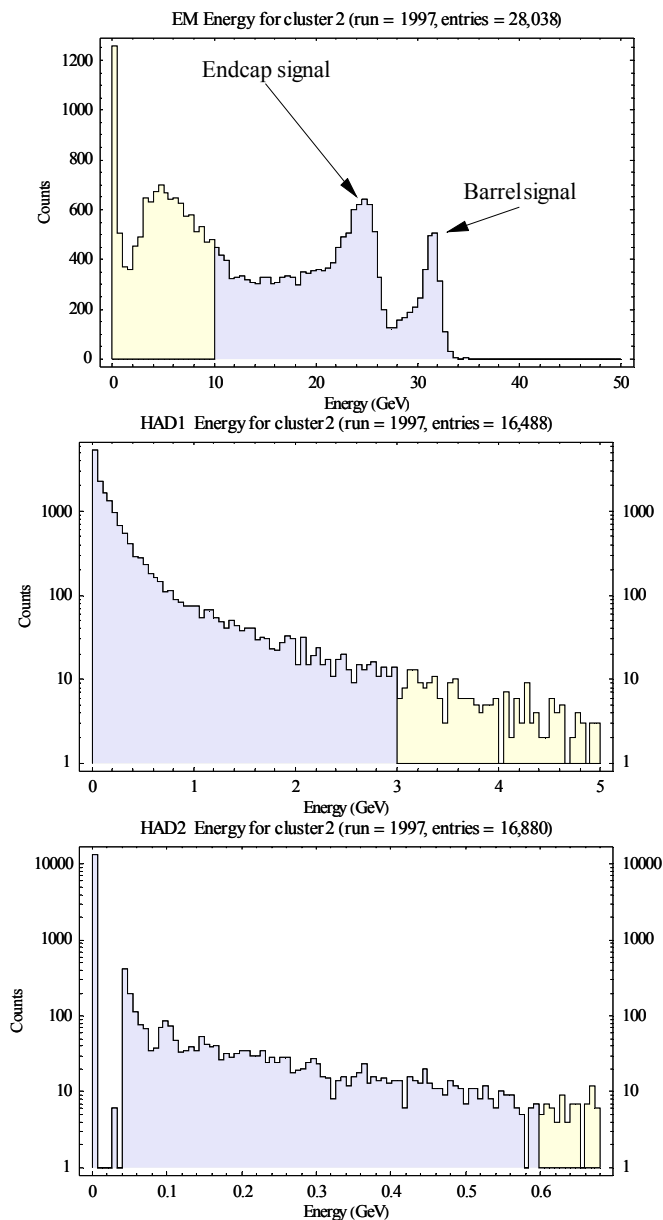


Figure 6-4 Cluster energy cuts for the second highest energy cluster. The only criteria applied to select events in each plot are the cluster quality cuts of equation (6.3) and five of the six criteria in equation (6.4), the missing criterion being the quantity actually plotted so that it is clear which events are being discarded by the cut (accepted events appear in the darker shaded region). Data is from the 1997 run and is representative of the entire SLD dataset.

Recall from section 6.1 that the energy scale used is that for a minimum ionizing particle, and therefore the true energies of the electron and positron are greater than represented in the plots.

Notice that the top plots in Figure 6-3 and Figure 6-4. both show two identical peaks, one at 32 GeV and one at 25 GeV. These two peaks are really just the single energy distribution of the WAB events, but they appear as two peaks due to two regions of the LAC which have different energy responses; the peak at 32 GeV are events contained in the barrel region ($|\cos \theta| < 0.7$), while the peak at 25 GeV are events confined to the endcap region ($|\cos \theta| > 0.7$). Again, as described in section 6.1, these energies are calibrated to the response of a minimum ionizing particle, and are therefore lower than the true electron or positron energy. The peak at 5 GeV in the top plot of Figure 6-4 is from background events, which are removed by the selection criterion $E_{EM1+EM2} > 10$ GeV for cluster 2. It is this last cut that is the most effective cut out of all of the selection criteria, as only about 17% of all Pass 2 events pass this one cut.

6.4.3 Angle Dependent Energy Cut

The next most effective cut is an angle dependent energy cut on the two highest energy clusters that addresses the different energy responses of the barrel and endcap regions of the LAC noted earlier. The values of the selection criteria are given in equation (6.5) and are displayed visually in Figure 6-5. As can be seen in this figure, the cut at 55 GeV in the barrel region is placed well below the band of WAB events at 65 GeV. As we enter the endcap region beginning at $|\cos \theta| \approx 0.68$ the amount of material in front of the LAC increases which causes the energy response of the LAC to decrease.

$$\begin{aligned}
0 &\leq |\cos \theta| < 0.68 & E_{\text{Total}}^{\text{cluster 1}} + E_{\text{Total}}^{\text{cluster 2}} > 55 \text{ GeV} \\
0.68 &\leq |\cos \theta| < 0.80 & E_{\text{Total}}^{\text{cluster 1}} + E_{\text{Total}}^{\text{cluster 2}} > 168.3 - 166.7 |\cos \theta_{\text{thrust}}| \\
0.80 &< |\cos \theta| & E_{\text{Total}}^{\text{cluster 1}} + E_{\text{Total}}^{\text{cluster 2}} > 20 \text{ GeV}
\end{aligned} \tag{6.5}$$

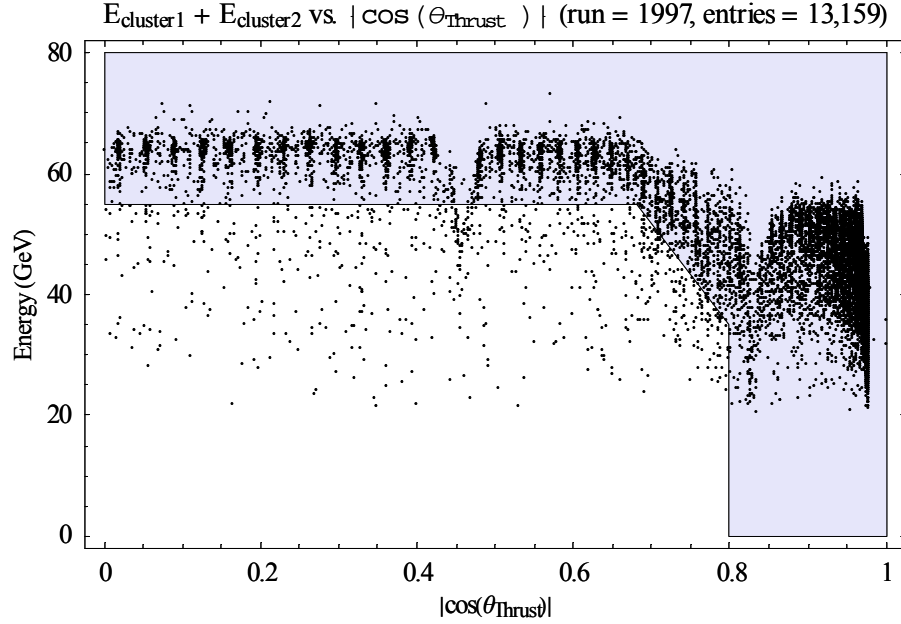


Figure 6-5 Angle dependent energy cut given in equation (6.5) for the sum of the energy of the two highest energy clusters. The band at 64 GeV are the WAB events. Material in front of the LAC begins degrading the energy response at $|\cos \theta| \approx 0.68$, which the cuts take into account. All cuts have been applied except for the angle dependent energy cut, which is shown in the shaded region. The data is from the 1997 run and is representative of the entire SLD dataset.

6.4.4 Global Event Cuts: Total Energy and Energy Imbalance

Thus far, all of the selection criteria have focused on selecting events with at least two high-energy clusters, but we have not applied any criteria to the event as a whole. Since all of the final state particles of a WAB event are electromagnetic, all of the particles within the acceptance of the LAC will deposit nearly all of their energy into the LAC. We therefore

place two requirements on the total energy of the event; the event must have a certain minimum energy, and this energy must be symmetrically distributed. To quantify these two requirements, we define the quantity E_{Total} as the sum of the total energy of all clusters satisfying the cluster quality cuts of equation (6.3), and $E_{\text{Imbalance}}$ as the magnitude of the vector sum of these clusters:

$$\begin{aligned}
 \vec{\nu} &\equiv (E_{\text{cluster}}, \theta_{\text{cluster}}, \phi_{\text{cluster}}) \\
 E_{\text{Total}} &= \sum |\vec{\nu}| \\
 E_{\text{Imbalance}} &= \frac{|\sum \vec{\nu}|}{E_{\text{Total}}}
 \end{aligned} \tag{6.6}$$

Clearly, for events with final state particles of negligible mass, those events with no invisible energy will have $E_{\text{Imbalance}} = 0$ since conservation of momentum will balance the energy symmetrically. However, events with missing or invisible energy (e.g. events with neutrinos in the final state) will have $E_{\text{Imbalance}} > 0$. In the limiting case where an event has just one particle with visible energy in the final state (as can occur with beam background) then $E_{\text{Imbalance}} = 1$.

Since the final state particles of WAB events all have negligible mass and have no invisible energy (they deposit nearly all of their energy into the EM section of the LAC), we require events to satisfy the following criteria, which has a negligible impact on WAB event selection efficiency while greatly reducing hadronic events, tau events and beam related background:

$$\begin{aligned}
 E_{\text{Total}} &> 15 \text{ GeV} \\
 E_{\text{Imbalance}} &< 0.6
 \end{aligned} \tag{6.7}$$

The distribution of E_{Total} is shown in Figure 6-6 for all Pass 2 events satisfying the cluster quality cuts of equation (6.3) for the 1997 Data. Notice the peaks at 65 GeV in the barrel region and 52 GeV in the endcap region, which are exactly twice the value of the two peaks in the top plots of Figure 6-3 and Figure 6-4, demonstrating that the events in these peaks carry the majority of their energy almost entirely in the two highest energy clusters. The 65 GeV peak are due to events in the barrel region of the LAC ($|\cos\theta| \leq 0.82$), while the 52 GeV peak are due to events in the endcap region of the LAC ($|\cos\theta| > 0.82$). The other peaks at lower energies in the plots are various kinds of background²² to the WAB signal, and are removed by cuts presented in later sections.

²² These background events come from both physics processes as well as beam related sources.

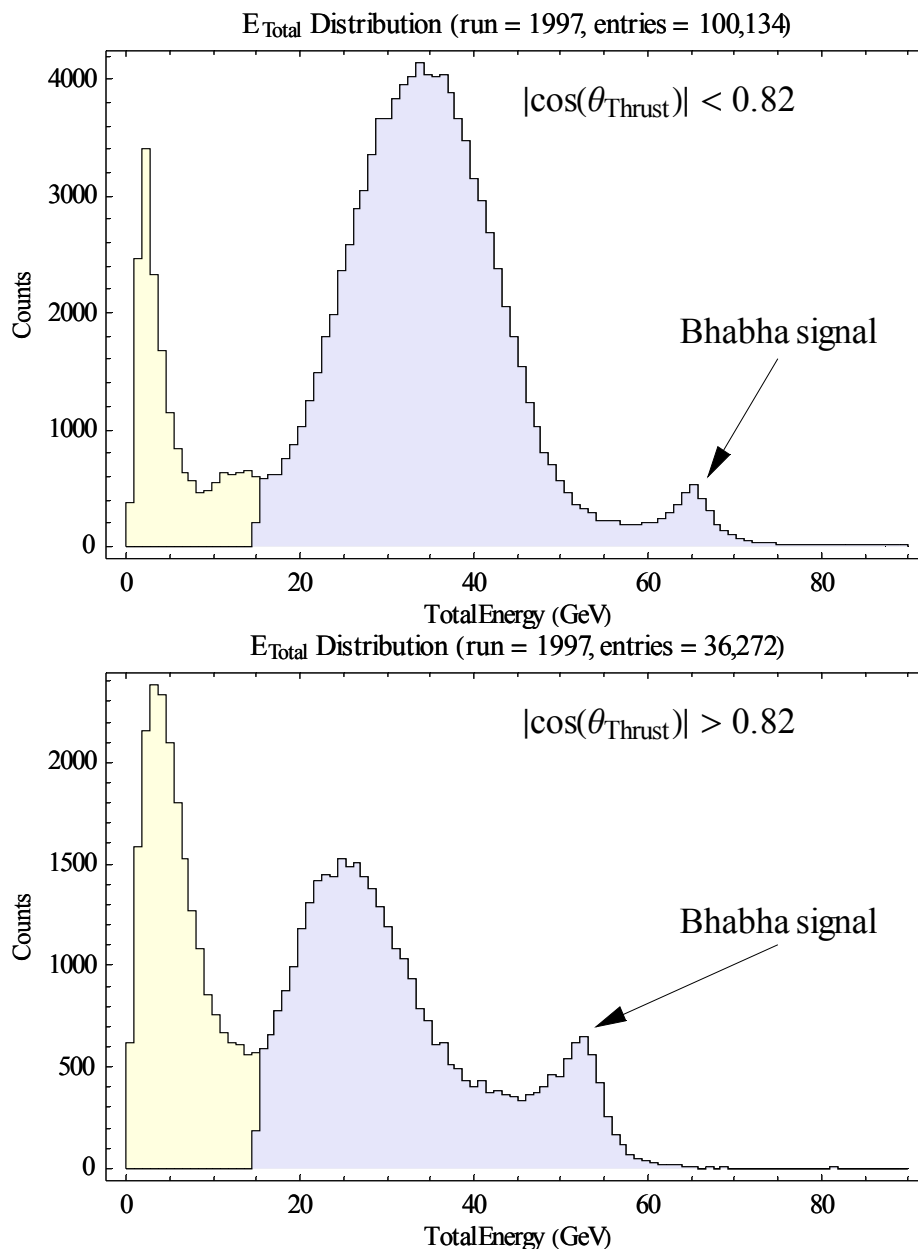


Figure 6-6 Total energy distribution of all Pass 2 events satisfying only the cluster quality cuts of equation (6.3). No other criteria have been applied other than there are at least two clusters in the event. The top plot shows events in the barrel region of the LAC ($|\cos \theta| < 0.82$) while the bottom plots show events in the endcap region of the LAC ($|\cos \theta| > 0.82$). The peak at 65 GeV in the barrel region and the peak at 52 GeV in the endcap region are the WAB events. The darker shaded region shows events satisfying the cut on total energy. Data is from the 1997 run and is representative of the entire SLD dataset.

The distribution of $E_{\text{Imbalance}}$ for the same subset of events is shown in Figure 6-7, and is plotted against E_{Total} in Figure 6-8. Notice the two clusters of events in this last figure at 65 GeV and 52 GeV with $E_{\text{Imbalance}}$ near 0 corresponding to the two peaks pointed out earlier in the top plots of Figure 6-3 and Figure 6-4, which is again consistent with the hypothesis that these are indeed WAB events.

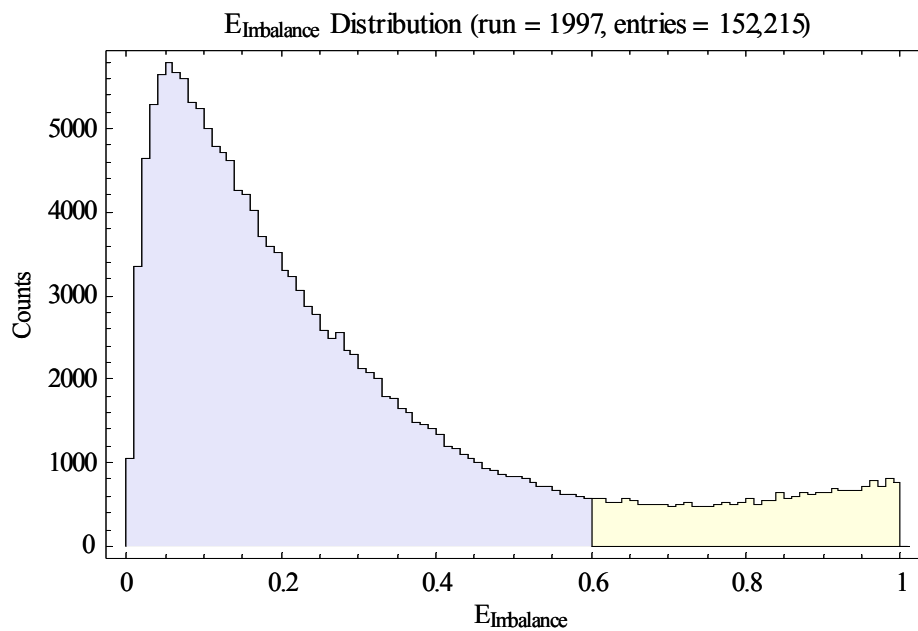


Figure 6-7 Energy imbalance of all Pass 2 events satisfying only the cluster quality cuts of equation (6.3). No other criteria have been applied other than there are at least two clusters in the event. The darker shaded region shows events satisfying the cut on energy imbalance. Data is from the 1997 run and is representative of the entire SLD dataset.

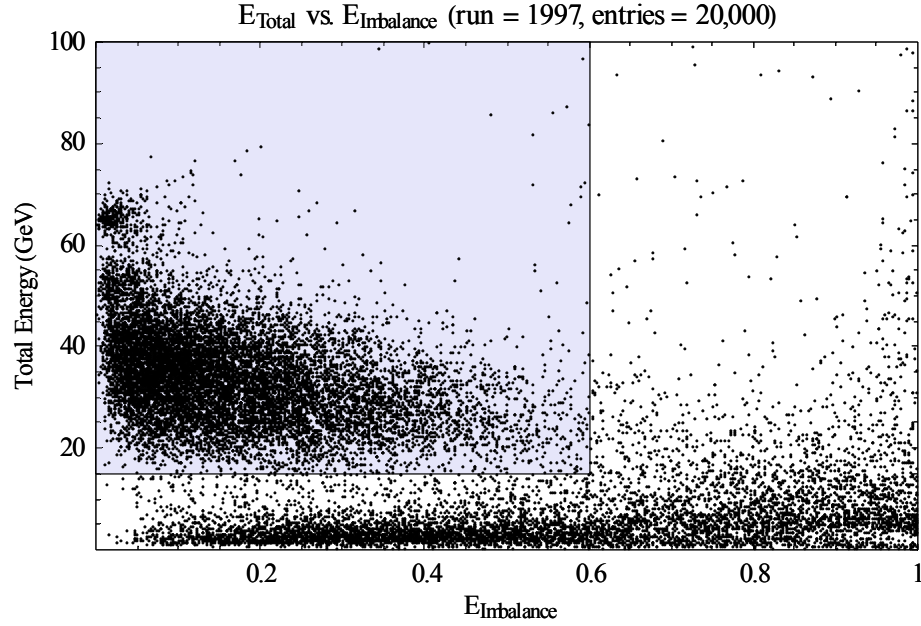


Figure 6-8 Total Energy vs. Energy Imbalance for Pass 2 events satisfying only the cluster quality cuts of equation (6.3). No other criteria have been applied other than there are at least two clusters in the event. The cluster of events at 65 GeV are events in the barrel region of the LAC ($|\cos\theta| < 0.82$), while the cluster of events at 52 GeV are events in the endcap region of the LAC ($|\cos\theta| > 0.82$). Both peaks are almost entirely WAB events. The darker shaded region shows events which satisfy the total energy and energy imbalance cuts in equation (6.7). Only 20,000 events are plotted from the 1997 SLD dataset in order to make the plot legible, although the data is representative of the entire SLD dataset.

6.4.5 Multiplicity Cut

The multiplicity of an event is defined as the number of calorimeter clusters in the event. The multiplicity of WAB events will be small since they have only an electron and positron in the final state, and so will have a typical value near two. Hadronic decays of the Z^0 , on the other hand, will have larger multiplicity values because of the much larger number of particles in the final state due to effects such as hadronization. The multiplicity distribution is shown in Figure 6-9 where these features can clearly be seen. The narrow distribution which peaks at 6 clusters are primarily the low multiplicity WABs, while the

broad distribution which peaks at 25 clusters are primarily the hadronic events. We therefore require WAB candidate events to lie within the following small event multiplicity range:

$$2 \leq n_{\text{clus}} \leq 11 \quad (6.8)$$

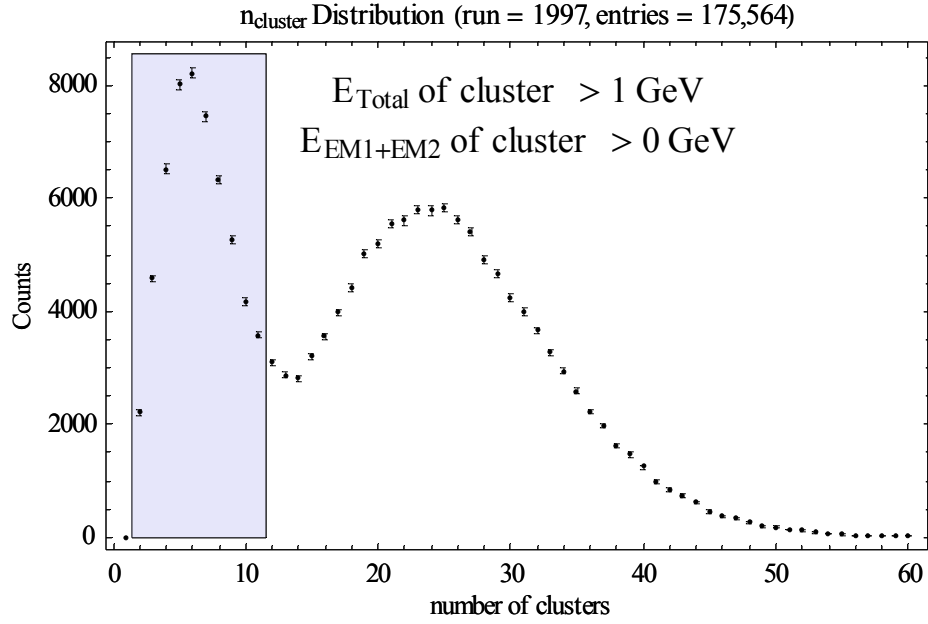


Figure 6-9 The number of clusters in the event (event multiplicity) for Pass 2 events satisfying only the cluster quality cuts of equation (6.3). No other criteria have been applied other than there are at least two clusters in the event. The narrow distribution which peaks at 6 clusters are primarily WAB events, while the broad distribution which peaks at 25 clusters are primarily hadronic events. The darker shaded region shows events satisfying the multiplicity cut in equation (6.8). Data is from the 1997 run and is representative of the entire SLD dataset.

6.4.6 Rapidity Cut

Finally, the last criterion imposed to select the final WAB event sample is the de-facto signature of a WAB event, namely that the two final state leptons are back to back, or nearly so, in the center-of-mass (or CMS) frame of reference. In the absence of radiative

corrections there will be no initial state radiation and the CMS frame will be the same as the LAB frame (i.e. the SLD LAC calorimeter in our case). In this scenario the clusters corresponding to these two leptons will always be back to back in the LAB frame and a simple hard cut on the acolinearity of the two highest energy clusters would suffice.

In the real world, however, radiative corrections are a fact of life and constitute large corrections of about 30% to the WAB cross section[75]. The effect of radiation on the kinematics of the event can be understood using the collinear radiation approximation[76] in which the differential cross section is convolved with two electron structure functions which give the probability for the incoming leptons to radiate away a fraction of their energy into photons which are collinear to the incoming leptons[77, 78]. In this approximation, the Bhabha scattering process is viewed as occurring in three steps:

1. Emission of collinear photons from the incoming electron and positron, known as Initial State Radiation or ISR. When there is initial state radiation there will typically be only one photon since this is a purely QED process²³. Before radiation, each incoming lepton has energy E_{beam} , and therefore the center-of-mass energy is $\sqrt{s} = 2 E_{\text{beam}}$. After initial state radiation, but before the hard scattering process (step 2. below), the electron (positron) has a fraction $x_- (x_+)$ of E_{beam} , such that $0 \leq x_{\pm} \leq 1$.
2. The actual hard scattering process $e^+e^- \rightarrow (Z^0, \gamma) \rightarrow e^+e^-$ occurring at a fractionally reduced collision-frame invariant energy squared $s' = s \cdot x_- \cdot x_+$.

²³ The probability of a QED vertex goes like α , where $\alpha = 1/137.035\,999\,76$ at $Q^2 = 0$. Therefore, the probability to emit more than one photon is small.

3. Emission of mostly collinear photons from the final state electron and positron, known as Final State Radiation or FSR. Most of the time the FSR photons are so close to the outgoing final state leptons as to be indistinguishable from them²⁴.

The problem, therefore, is how to identify the back-to-back nature of WAB events measured in the SLD LAB frame without knowing a priori the CMS system of the hard scattering process (step 2. above). We can qualitatively understand the nature of the problem from the preceding description of the collinear radiation approximation. If we assume one of the leptons radiates a photon and the other does not (by far the most probably scenario), then we can immediately see that when the energy of the radiated photon is small, the CMS system isn't boosted very much relative to the LAB frame and therefore the acolinearity between the final state leptons will be small. On the other hand, when the radiated energy of the photon is large then the CMS frame will be highly boosted relative to the LAB frame and the acolinearity between the final state leptons will be large. This situation is shown graphically in Figure 6-10.

²⁴ To quantify this, 1 Million Unibab events were generated and passed through the Bhabha selection criteria presented in this chapter. Of these, 525,053 pass the selection criteria and fall within the acceptance of the LAC, and of these events only 42,109, or 8% of the total, have a third cluster that has > 10 GeV and are separated from the nearest electron or positron by more than 0.02 in $\cos \theta$, the size of a typical LAC tower.

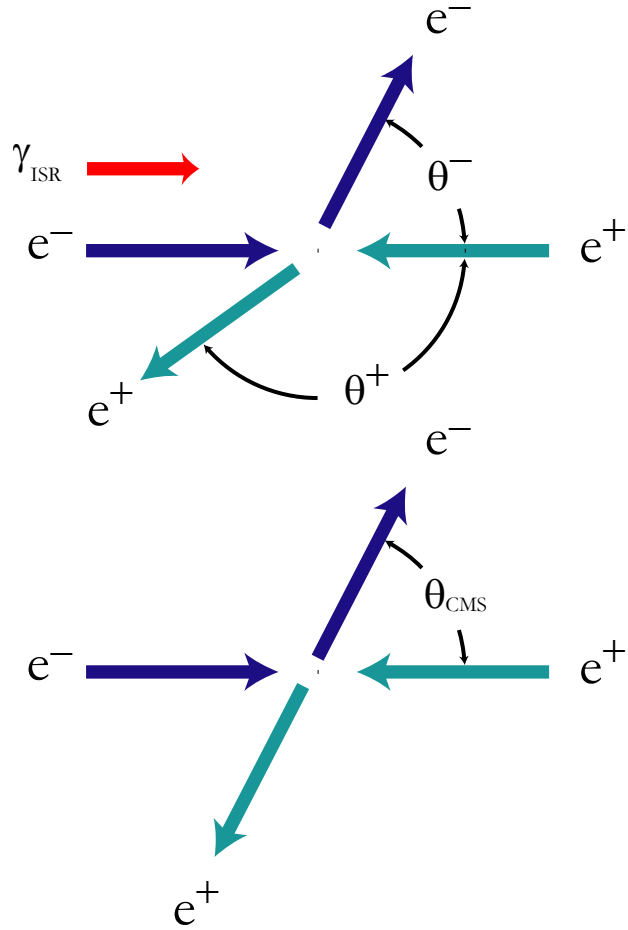


Figure 6-10 Kinematic diagram showing the LAB frame of reference (top diagram) and the center-of-mass (CMS) frame of reference (bottom diagram) when one photon is radiated during initial state radiation, as in the collinear radiation approximation.

From Figure 6-10 we define the acolinearity of the final state electron and positron in the LAB (i.e. LAC calorimeter) frame of reference:

$$\zeta = 180^\circ - (\theta_- + \theta_+) \quad (6.9)$$

Here θ_- and θ_+ are the LAB frame scattering angles of the electron and positron, respectively²⁵. Similarly, we can relate the LAB frame scattering angles to the center-of-mass scattering angle:

$$\cos \theta_{\text{CMS}} = \frac{\sin \frac{\theta_- - \theta_+}{2}}{\sin \frac{\theta_- + \theta_+}{2}} \quad (6.10)$$

We also define the rapidity as a simple relation between the fractional energies left to the electron and positron after initial state radiation:

$$y = \ln \sqrt{\frac{x_+}{x_-}} \quad (6.11)$$

In the limit of the collinear radiation approximation (i.e. assuming only one radiated photon in the initial state) this definition of rapidity is related to the LAB frame scattering angles of the final state particles[79]:

$$y = \sqrt{\frac{E + p_z}{E - p_z}} = \ln \sqrt{\frac{\sin \theta_+ (1 + \cos \theta_-) + \sin \theta_- (1 + \cos \theta_+)}{\sin \theta_+ (1 - \cos \theta_-) + \sin \theta_- (1 - \cos \theta_+)}} \quad (6.12)$$

Here E and p_z are the energy and longitudinal component of momentum, respectively, of the center-of-mass system as measured in the LAB frame.

Figure 6-11 shows the acolinearity as a function of the center-of-mass scattering angle for three values of x_- , the electron's fractional energy after initial state radiation,

²⁵ Although we label the angles separately for the electron and positron, none of the relations actually depend on the particle's type. All that matters are the two angles of the two final state particles independent of their actual type.

assuming that the positron did not radiate ($x_+ = 1$). From this figure it is clear that a cut on rapidity (or equivalently, a cut on the amount of initial state radiation) acts as an angle-dependent acolinearity cut.

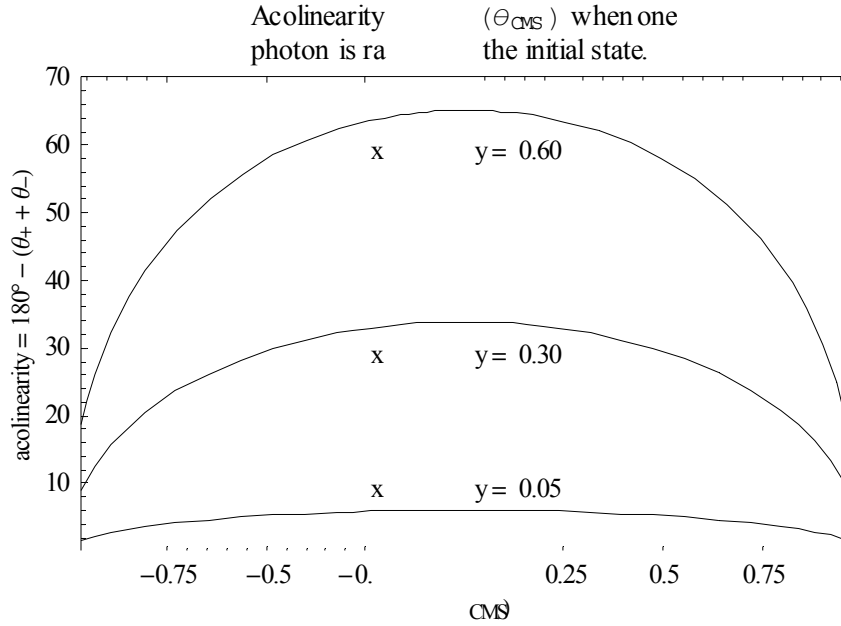


Figure 6-11 Acolinearity vs. $\cos \theta_{\text{CMS}}$ when one photon is radiated in the initial state. We have arbitrarily chosen to vary x_- , the electron's fractional energy after initial state radiation, and assume that the positron does not radiate ($x_+ = 1$). The value of $x_- = 55\%$ corresponds to a rapidity value of $y = 0.30$, the rapidity cut used for the WAB selection criteria.

We chose the following cut on rapidity, which corresponds to limiting a photon from initial state radiation to carry 45% or less of the beam energy down the beam pipe (i.e. $x_- = 55\%$). The distribution of rapidity and the photon's fractional energy are shown in Figure 6-12.

$$|y| < 0.3 \quad (6.13)$$

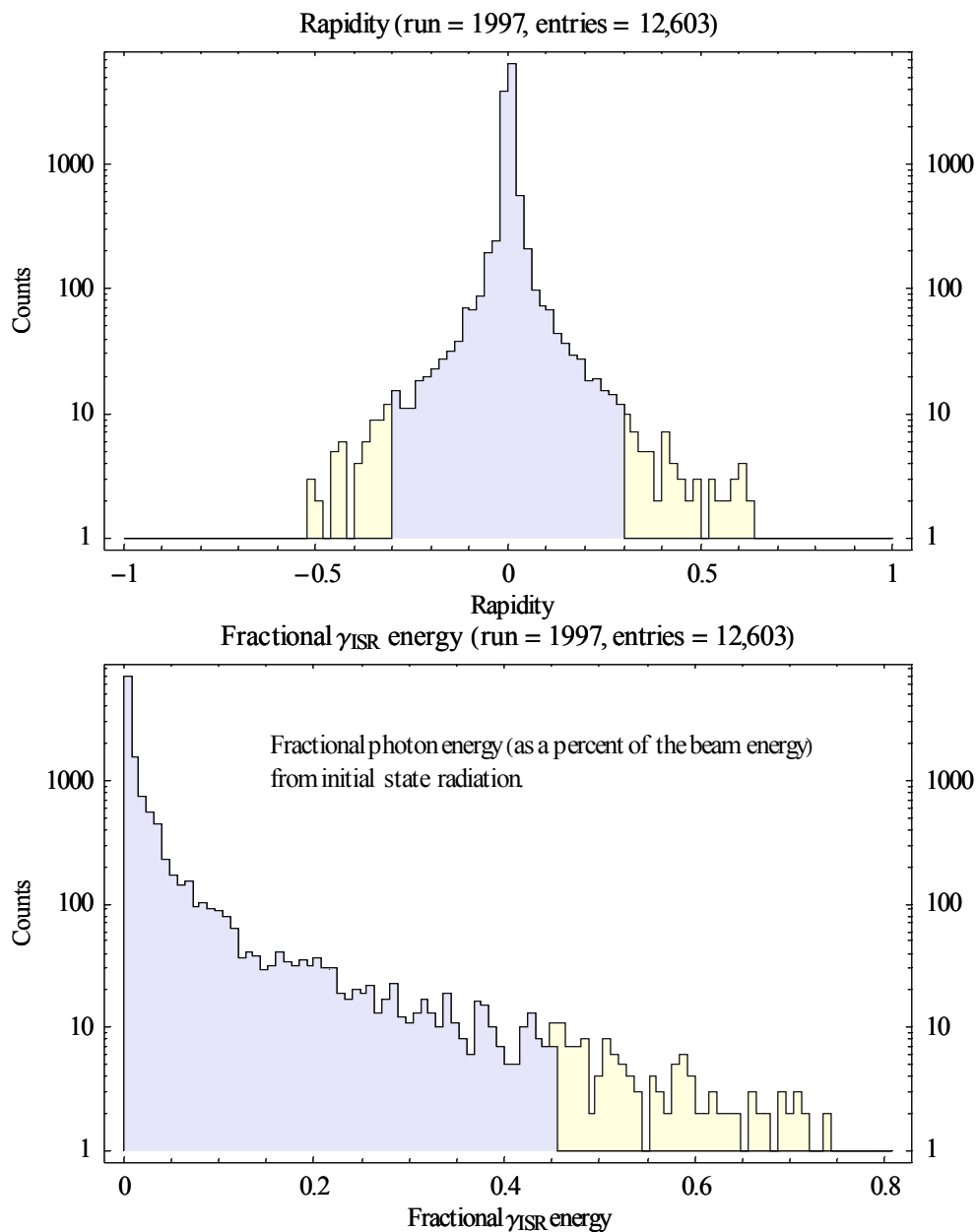


Figure 6-12 Rapidity distribution (top plot) and calculated fractional energy of a single photon from initial state radiation (bottom plot) for events passing all of the selection criteria except for the cut on rapidity. The rapidity cut, placed at $|y| < 0.3$, corresponds to a photon from initial state radiation carrying 45% or less of the beam energy. The darker shaded regions have all of the WAB selection cuts applied. Data is from the 1997 run and is representative of the entire SLD dataset.

6.4.7 Event Selection Summary

The wide-angle Bhabha event selection criteria take advantage of the unique topology of the relatively simple and clean final state particle distribution of Bhabha scattering. The 11 cuts used to select WAB events, and their effectiveness, are summarized below in Table 6-2. This table shows the percentage of events which pass each cut, which is listed separately for each SLD run period.

Table 6-2 Summary of the effectiveness for each cut (named in the first column) for each SLD run period (listed along the top). The numbers in the table specify the percentage of events passing the cut listed in the left-most column. For example, the single most effective cut for every run period is $EM(\text{cluster } 2) > 10 \text{ GeV}$ where only 12%-15% of the entire SLD dataset pass this single cut. The row labeled “Passing All Cuts” is the logical AND of all of the cuts, showing that only 6%-7% of the entire SLD dataset are WAB events. The sum of the individual cuts don’t add to 100% because all of the cuts are correlated with one another. The table is sorted by the column for the 1997 dataset, although the general trend for cut effectiveness is the same for all run periods.

Cut Name	Year				
	1994	1995	1996	1997	1998
Passing All Cuts	7%	6%	6%	7%	8%
$EM(\text{cluster } 2) > 10 \text{ GeV}$	13%	12%	12%	14%	15%
$2 \leq n_{\text{clus}} \leq 11$	29%	29%	43%	32%	32%
$EM(\text{cluster } 1) > 10 \text{ GeV}$	30%	30%	29%	33%	34%
Angle Dependent Energy Cut	36%	36%	44%	37%	39%
$HAD_2(\text{cluster } 1) > 10 \text{ GeV}$	61%	63%	64%	58%	60%
$HAD_2(\text{cluster } 2) > 10 \text{ GeV}$	72%	73%	76%	71%	72%
$HAD_1(\text{cluster } 1) > 10 \text{ GeV}$	75%	77%	78%	74%	75%
$ y < 0.3$	71%	69%	67%	74%	76%
$E_{\text{Total}} > 15$	78%	75%	66%	78%	80%
$HAD_1(\text{cluster } 2) > 10 \text{ GeV}$	87%	88%	89%	87%	87%
$E_{\text{Imbalance}} < 0.6$	86%	86%	79%	87%	88%

It is clear from the table that some cuts are more effective than others. For example, the most effective cut is for the electromagnetic energy of the second most energetic cluster to be $\text{EM}(\text{cluster } 2) > 10 \text{ GeV}$, as this rejects over 85% of all events. This makes perfect sense, since there are not many physics processes of the form $e^+e^- \rightarrow X$ which produce two such high energy electrons or photons in the final state (see section 6.5.2). Also note that the multiplicity cut is the next most effective selection criterion which rejects nearly 70% of all events, which is due to rejecting events from hadronic decays of the Z^0 .

This final tabulation of all events passing the WAB selection criteria are listed in Table 6-3. The last column shows the number of WAB events used in the log-likelihood fits (see Chapter 7) which are within the angular acceptance $|\cos \theta_{\text{Thrust}}| < 0.9655$ and for which a polarization quality cut is applied.

Table 6-3 Number of events in the entire SLD dataset, and the number of events which pass all of the WAB selection criteria described in the preceding sections. The last column is a subset of the “Pass All Cuts” column where the thrust angle is constrained to be within the acceptance used for the log-likelihood fits described in Chapter 7 below.

year	Total SLD Dataset	Pass All Cuts	Pass All Cuts and $ \cos \theta_{\text{Thrust}} < 0.9655$
1994	123,280	8,208	5,478
1995	57,587	3,462	2,497
1996	100,754	6,530	4,812
1997	175,564	12,461	9,126
1998	375,554	29,567	21,309
Total	832,739	60,228	43,222

6.5 Correction Factors

Since we will eventually perform a simultaneous fit of the selected WAB events for both \bar{g}_V^c and \bar{g}_A^c it is important to understand the efficiency of both our detector (e.g. the LAC) and our selection criteria, and possible contamination from other physics processes. The reason this is important is due to \bar{g}_A^c being a sensitive function of the shape of the WAB angular distribution. If any inefficiencies or contamination exist that have an angular dependence (and there is a strong detector inefficiency angular dependence in our case as will be shown below), then the measurement of \bar{g}_A^c (and \bar{g}_V^c through its correlation²⁶ with \bar{g}_A^c) will be affected. Additionally, since we use the luminosity measurement to provide an absolute normalization for the WAB angular distribution, it is important that the WAB inefficiencies be corrected.

6.5.1 Efficiency

For an ideal detector with 100% detection efficiency and with no material between it and the interaction point, the energy response as a function of angle for WAB events would be a perfect band at the center-of-mass energy, about 91 GeV (or in our case about 65 GeV since, as noted in section 6.1, we are using the minimum-ionizing-particle energy scale). However, as can be seen in Figure 6-13 below, the energy response of the LAC as a function of angle for WAB events is anything but uniform. Although there are large regions of the LAC which do have a uniform flat angular dependence (e.g. for $0 \leq |\cos \theta| < 0.42$ and $0.50 \leq |\cos \theta| < 0.65$), other regions do not, and it is these regions which are highly likely to be inefficient which are the most critical to correct the data for, and the most difficult to

²⁶The correlation coefficient between \bar{g}_V^c and \bar{g}_A^c is about 0.25 from our log-likelihood fits.

model. Regions such as $|\cos\theta| \geq 0.65$ are so critical because the LAC inefficiency is changing most rapidly and dramatically as a function of $\cos\theta$, which overlaps the region where the WAB cross section is also changing most rapidly.

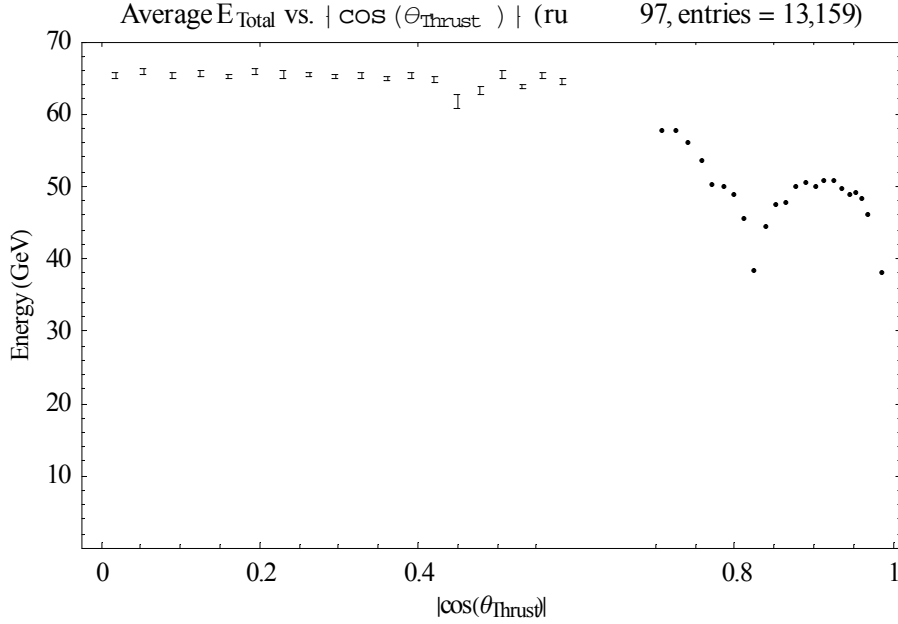


Figure 6-13 Average LAC energy response as a function of $|\cos\theta_{\text{Thrust}}|$. The plot is a profile histogram of selected WAB events showing the total event energy as a function of $|\cos\theta_{\text{Thrust}}|$, where there is one bin in $|\cos\theta_{\text{Thrust}}|$ for each LAC tower. Data is from the 1997 run and is representative of the entire SLD dataset.

A region of the LAC with a non-uniform energy response as a function of $\cos\theta_{\text{Thrust}}$ does not necessarily mean that the region is inefficient, although it is highly likely that detection inefficiencies do exist in the region. The reason for the non-uniform energy response of the LAC is largely due to a non-uniform distribution of material between the interaction point and LAC towers, since other reasons for the degraded energy response such as calibration errors and argon impurity have been accounted for[80]. Since we know there is more material in front of those regions of the LAC with the more degraded energy

response, we know that particles entering those regions will be more likely to begin showering in this material and the LAC will not detect the early energy deposition of these showers. Additionally, longitudinal shower fluctuations will be an even greater effect for these showers.

Many of the inefficient regions of the LAC are understood well enough that they can be correctly modeled with GEANT. For example, the dip in response for the region $0.435 \leq |\cos \theta| < 0.493$ (see Figure 6-13) is due to the washer where the barrel LAC sections are joined together. Since the material and geometry of the washer are well known, the energy loss of particles passing through this region of the SLD is well modeled.

Other inefficient regions of the LAC are qualitatively understood but are more difficult to model. The energy response for the region $0.65 \leq |\cos \theta| < 0.85$ falls off sharply and almost linearly. The material in front of the LAC in this region includes plumbing, electronics and cables for the endcap Drift chamber, barrel CRID and endcap CRID, in addition to the increased amount of aluminum dewar for the LAC. The energy response recovers a bit for the region $0.85 \leq |\cos \theta| \approx 0.9$, but then rapidly falls off again for $|\cos \theta| > 0.9$ as the cryogenics, electronics and cables for the Vertex Detector (and for the 1994-95 runs, the cables and connectors for the MASC) get in the way.

These observations have made modeling the LAC notoriously difficult for SLD physicists, and have limited many SLD physics analyses to the barrel region of the LAC. One possible solution is to try to correctly model all of the extra material in the region $|\cos \theta| \geq 0.65$ by including it as part of the GEANT description of the SLD. This method was used by Pitts[53] (see section 7.5.1) where the author empirically added approximations of material in various configurations until the LAC energy response as a function of angle for the simulated Monte Carlo WAB events matched that of the real data.

We have chosen another, independent method to correct the WAB data for inefficiencies. Our new method, which we call the *Pseudo Event Method*, uses the data itself to measure the LAC inefficiency as a function of $\cos\theta$. This method takes advantage of our knowledge of the unique physics topology of a WAB event. We determined and used a special set of selection criteria which selected a subset of all SLD events which would have passed the WAB selection criteria described in section 6.4 above except for the cluster selection criteria (i.e. we only kept the selection criteria for the global event quantities). In place of the cluster selection criteria, we required only an electron or positron in the final state with energy above an angle dependent hard energy threshold, which are listed in Table 6-4.

Table 6-4 Angle dependent energy thresholds for selecting Pseudo Events. Any SLD event with $|\cos\theta_{\text{Low}}| \leq |\cos\theta_{\text{Thrust}}| < |\cos\theta_{\text{High}}|$ for which $E_{\text{cluster}} \geq$ the energy threshold listed in the table is a candidate for one-half of a Pseudo Event.

$ \cos\theta_{\text{Low}} $	$ \cos\theta_{\text{High}} $	Energy Threshold (GeV)
0	0.435	30.0
0.435	0.464	22.0
0.464	0.493	26.0
0.493	0.6985	30.0
0.6985	0.7335	27.5
0.7335	0.765	25.0
0.765	0.793	22.0
0.793	0.8185	20.0
0.8185	0.8465	18.0
0.8465	0.872	23.0
0.872	0.897	25.0
0.897	0.9655	26.0

The energy thresholds are chosen empirically to select WAB events for an ideal detector with 100% detection efficiency. The idea is to choose a stiff enough energy threshold so that when we find an event with a LAC cluster above this energy threshold (which we call a *Gold Cluster*) we know that if the detector were 100% efficient then there must be another cluster with this much energy, but in the opposite direction, in order to balance energy and momentum for the event. We create two lists of events by dividing the LAC into two hemispheres of North and South. Event information for Gold Clusters that are in the North hemisphere are written to the North Cluster List, and event information for events with a Gold Cluster in the South hemisphere are written to the South Cluster List. Each list contains the four quantities Run Number, Event Number, LAC Tower Index (determined by $\cos \theta_{\text{Cluster}}^{\text{Gold}}$) and $\phi_{\text{Cluster}}^{\text{Gold}}$. With these two lists in hand we create yet a third list which is a combination of the North and South Cluster Lists. This third list contains random permutations of each list's entries with the same LAC Tower Indices, and is called the *Pseudo Event Index Table*.

The Pseudo Event Index Table is a lookup table that allows us to create the pseudo-events. For each entry in this table, we take only the clusters from the South hemisphere for the event tagged with the North Gold Cluster and add these clusters into a new event structure with the clusters from the North hemisphere tagged by the South Gold Cluster. The angle ϕ_{Cluster} for each cluster in these hemispheres is rotated by $\pi - \phi_{\text{Cluster}}^{\text{Gold}}$ so that if the event with the Gold Cluster were a WAB, the clusters would line up in the proper back-to-back fashion. For this rotation, we arbitrarily chose to rotate the South Clusters. This new event structure, which is the combination of clusters from independent events, is appropriately called a Pseudo Event.

Finally, this new set of Pseudo Events is passed through the normal full WAB selection criteria described in section 6.4 above. For a detector with 100% efficiency we would expect all of the Pseudo Events to pass; any Pseudo Events that do not pass must be due to inefficiency. The inefficiencies are independently measured and calculated for each SLD run period and for each KAL tower. The efficiency for each KAL tower for the 1997 data, which is representative of all of the SLD run periods, is shown in Figure 6-14.

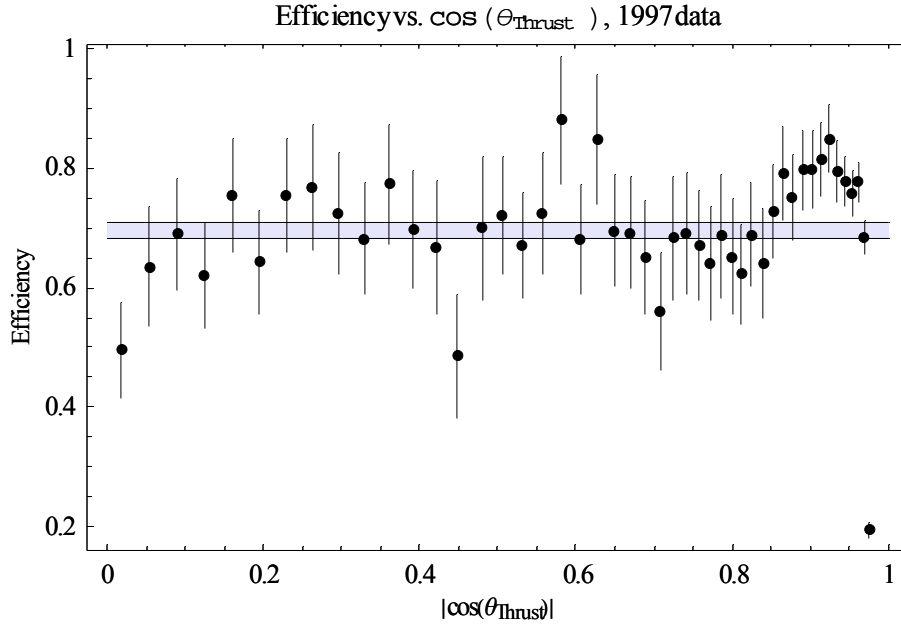


Figure 6-14 Efficiency as a function of $|\cos \theta_{\text{Thrust}}|$ as determined by the Pseudo Event method. Data is from the 1997 run and is representative of the entire SLD dataset.

6.5.2 Contamination

Other non-WAB physics processes could potentially slip through our WAB selection criteria to make our final selection of WAB events impure by some factor. The primary sources are $e^+e^- \rightarrow \gamma\gamma$ and $e^+e^- \rightarrow Z^0 \rightarrow \tau^+\tau^- \rightarrow e^+\nu_e\bar{\nu}_\tau e^-\bar{\nu}_e\nu_\tau$. These processes were

measured by Pitts[53] (see section 7.5.3) and found to be relatively small, with an overall contamination of 1.25% and 0.28% of the WAB yield, respectively. Pitts measured the contamination of these two processes as a function of angle, which is important since the differential cross section angular distributions are both different from the WAB differential cross section angular distribution. Additionally, Pitts performed Monte Carlo studies of the contamination from the hadronic decays of the Z^0 and found the contamination to be $< 1\%$, which is negligible. We simply reuse these small correction factors to correct our WAB data.

6.5.3 Summary of Correction Factors

The correction factors for both efficiency and contamination are used to correct the selected WAB events for each SLD run period on a per LAC tower basis. Plots of all of the data showing the final angular distributions of selected WAB events both before and after all of the correction factors are shown in Figure 6-15 through Figure 6-19. These datasets will be used in the log-likelihood fits in Chapter 7.

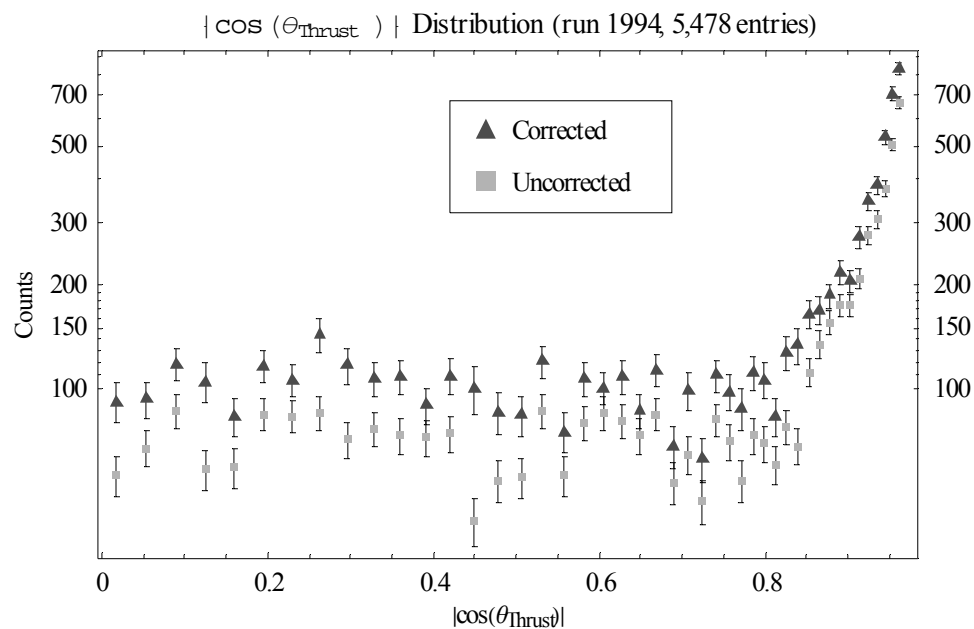


Figure 6-15 Angular distribution of selected WAB events corrected for efficiency and contamination. Data is from the 1994 run.

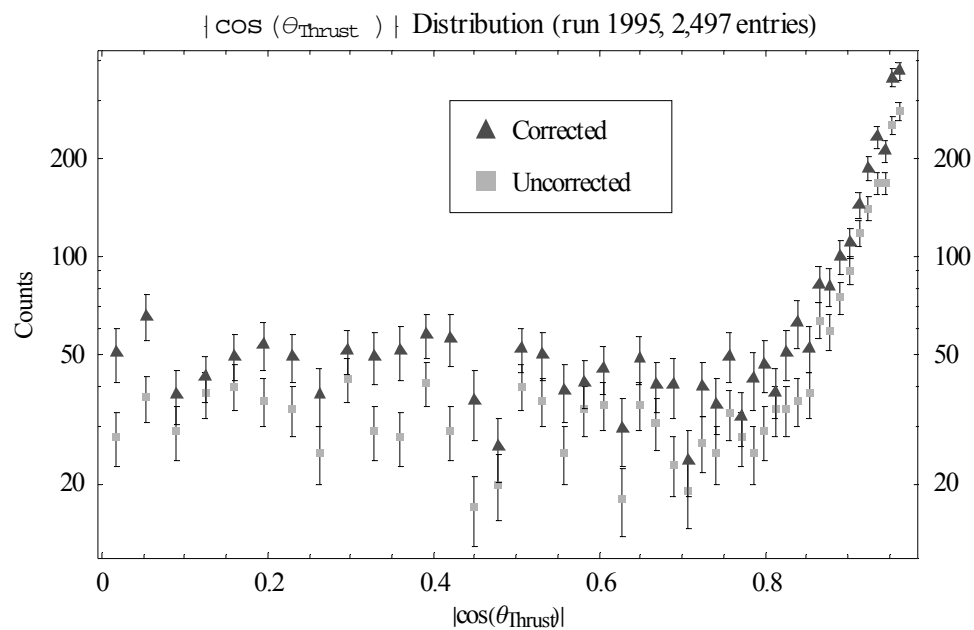


Figure 6-16 Angular distribution of selected WAB events corrected for efficiency and contamination. Data is from the 1995 run.

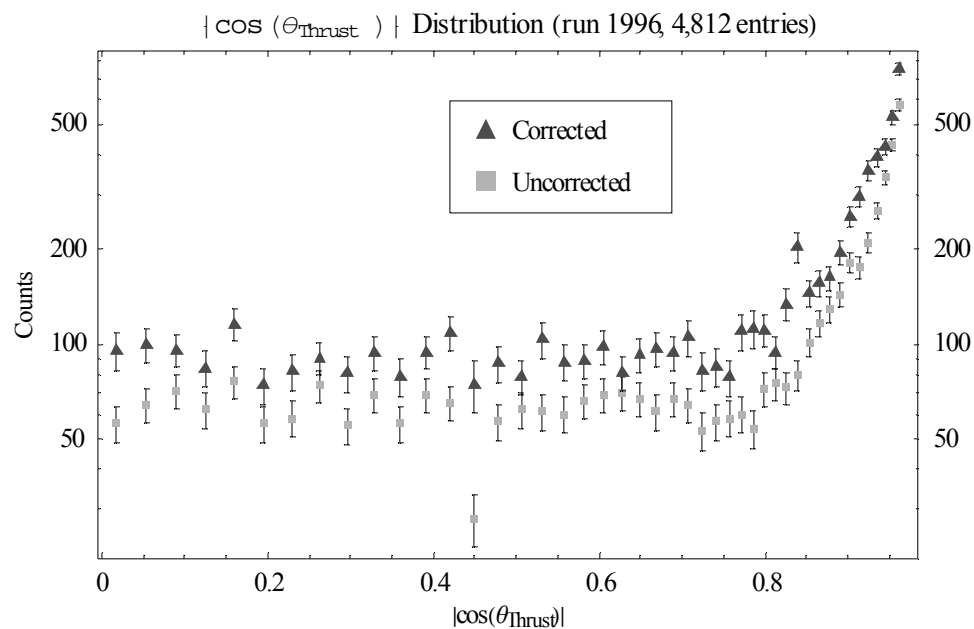


Figure 6-17 Angular distribution of selected WAB events corrected for efficiency and contamination. Data is from the 1996 run.

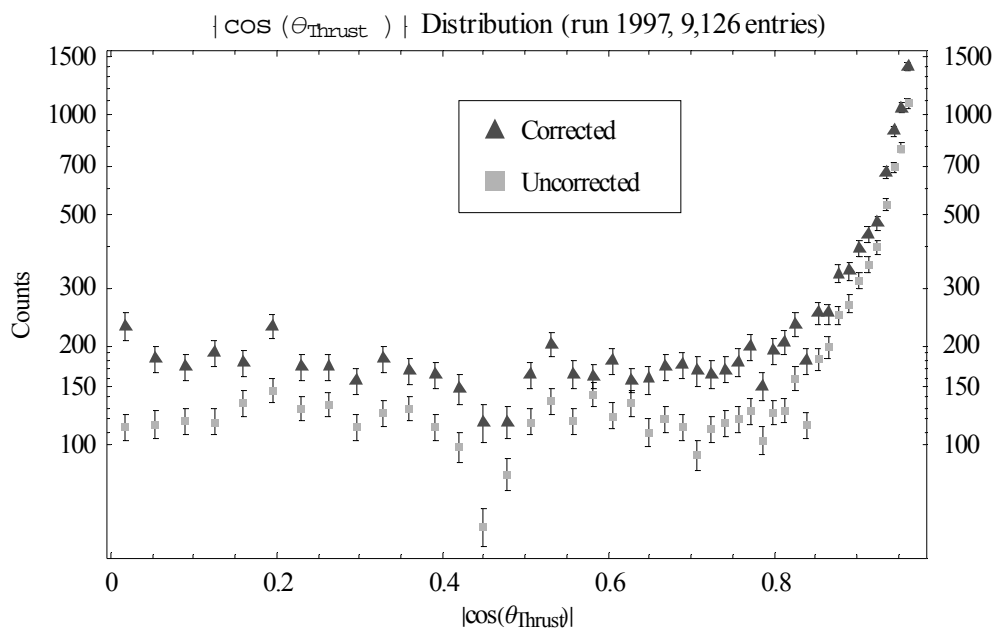


Figure 6-18 Angular distribution of selected WAB events corrected for efficiency and contamination. Data is from the 1997 run.

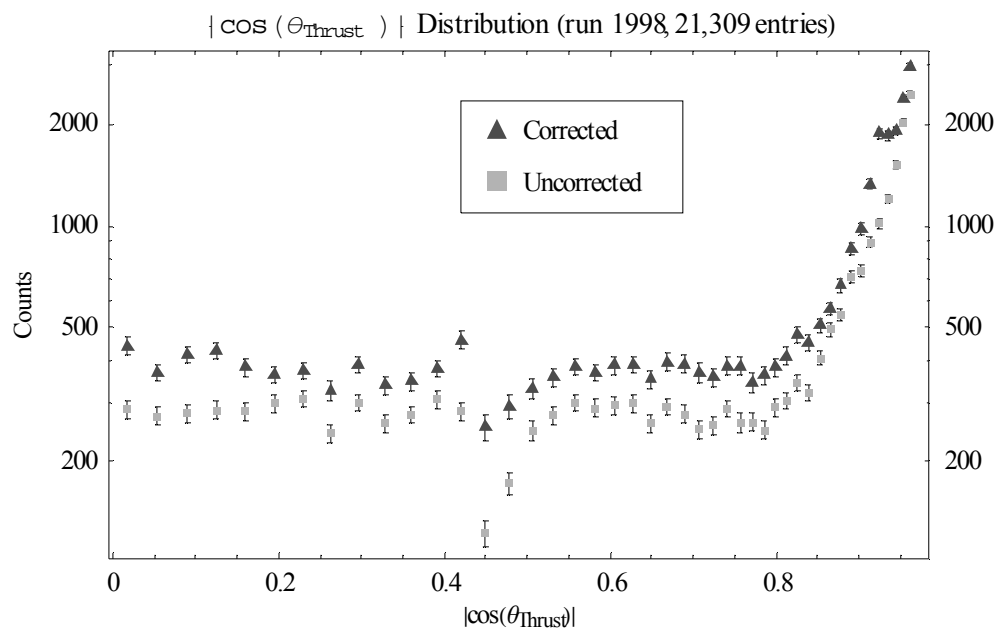


Figure 6-19 Angular distribution of selected WAB events corrected for efficiency and contamination. Data is from the 1998 run.

CHAPTER 7 DATA ANALYSIS AND RESULTS

In this chapter, we present the analysis techniques used to extract the electron coupling parameters \overline{g}_V^e and \overline{g}_A^e from the angular distribution of the polarized wide-angle Bhabha scattered events and the luminosity measurement. First, we describe the Extended Maximum Likelihood method. Next, the function that is minimized is described in some detail, as it is here that careful attention must be paid to incorporating the radiative corrections into the tree-level analytical expression that describes polarized wide-angle Bhabha scattering. Finally, we present the results of the fit, followed by a discussion of the systematic errors.

7.1 The Extended Maximum Likelihood Method

Given a probability distribution function $P(x, \tau)$ (hereafter called the p.d.f.) which describes the distribution of a random variable x for a specified value of a parameter τ , the method of maximum likelihood is used to estimate the best value of the parameter τ for a given finite sample of data. Under the assumption that each measurement x_i is independent of every other measurement, the probability for a set of n measurements of the x_i to occur, where each observation i is measured to be between x_i and $x_i + dx_i$, is given by

$$\prod_{i=1}^n P(x_i, \tau) dx_i \quad (7.1)$$

If the hypothesis $P(x, \tau)$ correctly describes the physics we measure in the laboratory, then one expects a higher probability for values of τ that are closer to its true value than for values of τ that are farther away from its true value. Since the dx_i do not depend on the parameter τ , the same line of reasoning holds for the following function $L(\tau)$, called the likelihood function:

$$L(\tau) = \prod_{i=1}^n P(x_i, \tau) \quad (7.2)$$

Therefore, determining the value of $\tau = \tau_{\text{MAX}}$ for which the likelihood function $L(\tau)$ is a maximum will provide the best estimate of τ for the finite sample of observations x_1, \dots, x_n . Finding the value of τ_{MAX} is straightforward, as it is simply the solution to the equation

$$\partial_{\tau} L(\tau) = 0 \quad (7.3)$$

Therefore, the requirements on $L(\tau)$ are really quite general, requiring only that the function be differentiable w.r.t. the parameter τ . Without loss of generality, we can extend the procedure to allow each measurement of the random variable x_i to be a collection of observables, so that each x_i is a vector of measurements and not just a single measurement. Likewise, there is no reason to limit the hypothesized p.d.f. to be a function of just one parameter, as allowing the p.d.f. to be a function of multiple parameters is straightforward. For the case of m such parameters equation (7.3) generalizes to

$$\partial_{\tau_j} L(\tau_j) = 0 \quad j = 1, \dots, m \quad (7.4)$$

This technique for determining the best estimate of a model's parameters τ_j from a finite sample of data is known as the maximum likelihood method.

Up to now, the size of the data sample n has been fixed. However, in our case we not only have a collection of n polarized wide-angle Bhabha events, but the SLD Luminosity Monitor also tells us how many events we should expect in our polarized wide-angle Bhabha sample by way of the luminosity measurement of small-angle Bhabhas. Recall that

$$\nu = \mathcal{L}_{\text{Integrated}} \sigma \quad (7.5)$$

Where ν is the expected number of polarized wide-angle Bhabha events, $\mathcal{L}_{\text{Integrated}}$ is the integrated luminosity and σ is the integrated wide-angle Bhabha cross section of our polarized wide-angle Bhabha hypothesis. Therefore, the luminosity tells us, within Poisson statistics, what the sample size n of our polarized wide-angle Bhabha events should be. Thus, the procedure is clear: we simply modify equation (7.1) by multiplying it by the probability that n polarized wide-angle Bhabha events are seen for a given luminosity $\mathcal{L}_{\text{Integrated}}$, which is simply given by the well-known Poisson distribution, so that our new likelihood function becomes

$$L(x_i, \tau) = \frac{\nu^n}{n!} e^{-\nu} \prod_{i=1}^n P(x_i, \tau) \quad (7.6)$$

The explicit construction of this likelihood function is the topic of the next section.

7.2 The Likelihood Function for Polarized Bhabha Scattering

For the case of wide-angle Bhabha scattering, the vector of measurements consists of the scattering angle $x = \cos \theta$ and the polarization of the incident electron beam P_e , where the polarization may be negative (for left-handed events) or positive (for right-handed events). Thus, for a set of n independent measurements of these two observables, we have $\{(x_1, P_{e,1}), (x_2, P_{e,2}), \dots, (x_n, P_{e,n})\}$.

The model for the hypothesis of polarized wide-angle Bhabha scattering is simply the polarized differential cross section $\partial_x \sigma(x, P_e; \bar{g}_V^e, \bar{g}_A^e)$ for this set of measurements, and is given by the sum of the analytic expressions in equations (3.1) through (3.10) in Chapter 3 above. Recall that this equation describes the differential cross section for the combined process $e^+ e_{L,R}^- \rightarrow Z^0, \gamma \rightarrow e^+ e^-$, where $e_{L,R}^-$ represents an initial state electron that is either left-handed (meaning its spin is anti-parallel to its momentum vector) or right-handed (meaning its spin is parallel to its momentum vector). Therefore, the differential cross section $\partial_x \sigma(x, P_e; \bar{g}_V^e, \bar{g}_A^e)$ may be written as

$$\partial_x \sigma(x, P_e; \bar{g}_V^e, \bar{g}_A^e) = p_L \partial_x \sigma_L(x; \bar{g}_V^e, \bar{g}_A^e) + p_R \partial_x \sigma_R(x; \bar{g}_V^e, \bar{g}_A^e) \quad (7.7)$$

Where $p_{L,R}$ is the probability that the initial state electron is either left-handed or right-handed, respectively. These two probabilities must be assigned to the initial state electron because the SLC experimental apparatus does not prepare single, individual electrons with a specific energy and helicity for scattering off a single, individually prepared positron with a specific energy. Instead, approximately 10^{10} electrons, known as a bunch, are made to pass through another bunch of positrons in the hope that just one electron will interact with one positron. This process is called a beam crossing and is repeated 120 times

each second. For each beam crossing, the energy distribution is measured for each electron and positron bunch. Additionally, the average polarization P_e is measured for each electron bunch.

Thus, for each event produced by a beam crossing, the exact energy and helicity of the initial state electron and positron are not known, as only the bulk properties of each electron and positron bunch are known. Therefore, only the probabilities are known as to whether the electron or positron had a specific energy, and whether the electron was left or right-handed. Thus, to turn the expression for the cross section into a probability that can be used for a maximum likelihood fit, the average polarization P_e for each electron bunch must be turned into a probability that the interacting electron was either left or right-handed.

To begin, we define the electron bunch polarization to be

$$P_e = \frac{N_L - N_R}{N_L + N_R} \quad (7.8)$$

where N_L and N_R are the number of left-handed and right-handed electrons in a given bunch, respectively.

To calculate the likelihood function for the data $\{(x_1, P_{e,1}), (x_2, P_{e,2}), \dots, (x_n, P_{e,n})\}$ and for a given set of values for \bar{g}_V^e and \bar{g}_A^e , we must know the probability $P(x_i, P_{e,i}; \bar{g}_V^e, \bar{g}_A^e)$ that a given event i scattered at an angle $x_i = \cos \theta_i$ and was produced by an incoming beam of electrons with average polarization P_e . This probability is just the ratio of the differential wide-angle Bhabha cross section to the total wide-angle Bhabha cross section integrated over the acceptance of the SLD calorimeter

$$P(x_i, P_{e,i}; \bar{g}_V^e, \bar{g}_A^e) = p_L \frac{\partial_x \sigma_L(x_i, P_{e,i}; \bar{g}_V^e, \bar{g}_A^e)}{\int_{\text{LAC}} \partial_x \sigma_L(x_i, P_{e,i}; \bar{g}_V^e, \bar{g}_A^e) dx} + p_R \frac{\partial_x \sigma_R(x_i, P_{e,i}; \bar{g}_V^e, \bar{g}_A^e)}{\int_{\text{LAC}} \partial_x \sigma_R(x_i, P_{e,i}; \bar{g}_V^e, \bar{g}_A^e) dx} \quad (7.9)$$

The probabilities $p_{L,R}$ can be determined from P_e , as equation (7.8) can be written as

$$P_e = \frac{N_L - N_R}{N_L + N_R} = \frac{p_L - p_R}{p_L + p_R} \quad (7.10)$$

Since $p_L + p_R = 1$ (as they are probabilities), we can rewrite equation (7.10) as

$$\begin{aligned} P_e &= p_L - (1 - p_R) \\ &= 2p_L - 1 \end{aligned} \quad (7.11)$$

Therefore, we can write p_L and p_R in terms of P_e :

$$\begin{aligned} p_L &= \frac{1}{2}(1 + P_e) \\ p_R &= \frac{1}{2}(1 - P_e) \end{aligned} \quad (7.12)$$

To summarize these definitions and formalism and form the actual log-likelihood function, we substitute the tree-level analytical differential cross section equations (3.1) through (3.10) into equation (3.11) along with the coefficients from Table 3-4 which gives us $\partial_x \sigma$, the differential cross section for polarized wide-angle Bhabha scattering that includes radiative corrections. The expression for $\partial_x \sigma$ includes 10 parameters defined in Table 3-2, and we substitute the values from this table into $\partial_x \sigma$ except for P_e (the initial state electron polarization) and $s = E_{\text{CM}}^2$ (the square of the center-of-mass energy), and the two parameters we fit for, \bar{g}_V^e and \bar{g}_A^e . The average values for $|P_e|$ and E_{cm} are measured experimentally by

SLD for each run period and are given in Table 4-1 and Table 4-2. We substitute the appropriate values from these tables into $\partial_x \sigma$ depending on the SLD dataset we fit for. The sign of P_e is measured on an event-by-event basis and is substituted during the fitting process to be described in the next section. The average values for $|P_e|$ are also used to determine p_L and p_R using equation (7.12). The values for $\partial_x \sigma$, p_L and p_R are then substituted into equation (7.9) to give $P(x_i, P_{e,i}; \bar{g}_V^e, \bar{g}_A^e)$, the probability that a given event has $|\cos \theta| = x_i$ and signed initial state electron polarization $P_{e,i}$. We use $|\cos \theta| < 0.9655$ for the limits of integration for the angular acceptance of the LAC. The polarized luminosity measurements from Table 5-4 and $\int_{LAC} \partial_x \sigma$ are substituted into equation (7.5) to determine ν , the expected number of wide-angle Bhabha events. Finally the likelihood function is formed for each SLD dataset containing n wide-angle Bhabha events by substituting n , ν and $P(x_i, P_{e,i}; \bar{g}_V^e, \bar{g}_A^e)$ into equation (7.6).

7.3 Fitting the Polarized Bhabha Distribution for \bar{g}_V^e and \bar{g}_A^e

To minimize equation (7.6) we use RooFit[81], a C++ class library designed for minimizing and plotting multivariate probability distribution functions. RooFit is itself built on top of ROOT[82], which is also a C++ class library and is designed for large scale data analysis and provides core data analysis services such as histograms, plotting and fast access to large datasets stored in its own proprietary format. The core minimization engine provided by ROOT, and therefore RooFit, is a wrapper around the MINUIT [83] program. The results of the Maximum Likelihood fits coming from RooFit for all SLD run periods are given in Table 7-1. The systematic errors for these results are presented in section 7.4 below.

Table 7-1 Maximum Likelihood fit results for all SLD run periods. The errors are statistical only and derive from $\frac{1}{2}$ a unit of log-likelihood from the point of maximum likelihood.

Run Period	\bar{g}_V^e	\bar{g}_A^e
1994	-0.0337 \pm 0.0064	-0.4901 \pm 0.0026
1995	-0.0498 \pm 0.0097	-0.4803 \pm 0.0039
1996	-0.0539 \pm 0.0070	-0.5245 \pm 0.0028
1997	-0.0527 \pm 0.0053	-0.5038 \pm 0.0020
1998	-0.0467 \pm 0.0036	-0.5054 \pm 0.0014

Table 7-2 lists the number of unweighted, weighted (corrected for efficiency and contamination) and expected wide-angle Bhabha events for each SLD run period. The number of expected events ν is calculated using the polarized luminosities from Table 5-4 and the integrated wide-angle Bhabha cross section used in the likelihood function.

Table 7-2 Number of unweighted, weighted (corrected for efficiency and contamination) and expected wide-angle Bhabha events for each SLD run period. The number of expected events ν is calculated using the polarized luminosities from Table 5-4 and the integrated wide-angle Bhabha cross section used in the likelihood function. The fitted value for \bar{g}_V^e and \bar{g}_A^e from Table 7-1 are used in the cross section calculation.

SLD Run	Unweighted Events		Weighted Events		Expected Events	
	Left	Right	Left	Right	Left	Right
1994	2,885	2,593	3,936	3,544	3,858	3,517
1995	1,338	1,159	1,848	1,599	1,796	1,561
1996	2,603	2,209	3,757	3,192	3,500	2,933
1997	4,837	4,289	6,627	5,822	6,464	5,630
1998	11,294	10,015	15,253	13,478	14,213	12,424

The results of the fit are overlaid with the data in Figure 7-1 through Figure 7-10. The inset figures of the distribution of residuals all show a mean near zero and a standard deviation near one, as expected for a good fit. Figure 7-11 shows the wide-angle Bhabha polarized differential cross section for the data from all SLD run periods, 1994-1998,

overlaid with the analytical expression for the polarized wide-angle differential cross section evaluated using the final fit results for \overline{g}_V^e and \overline{g}_A^e given in section 7.5 below.

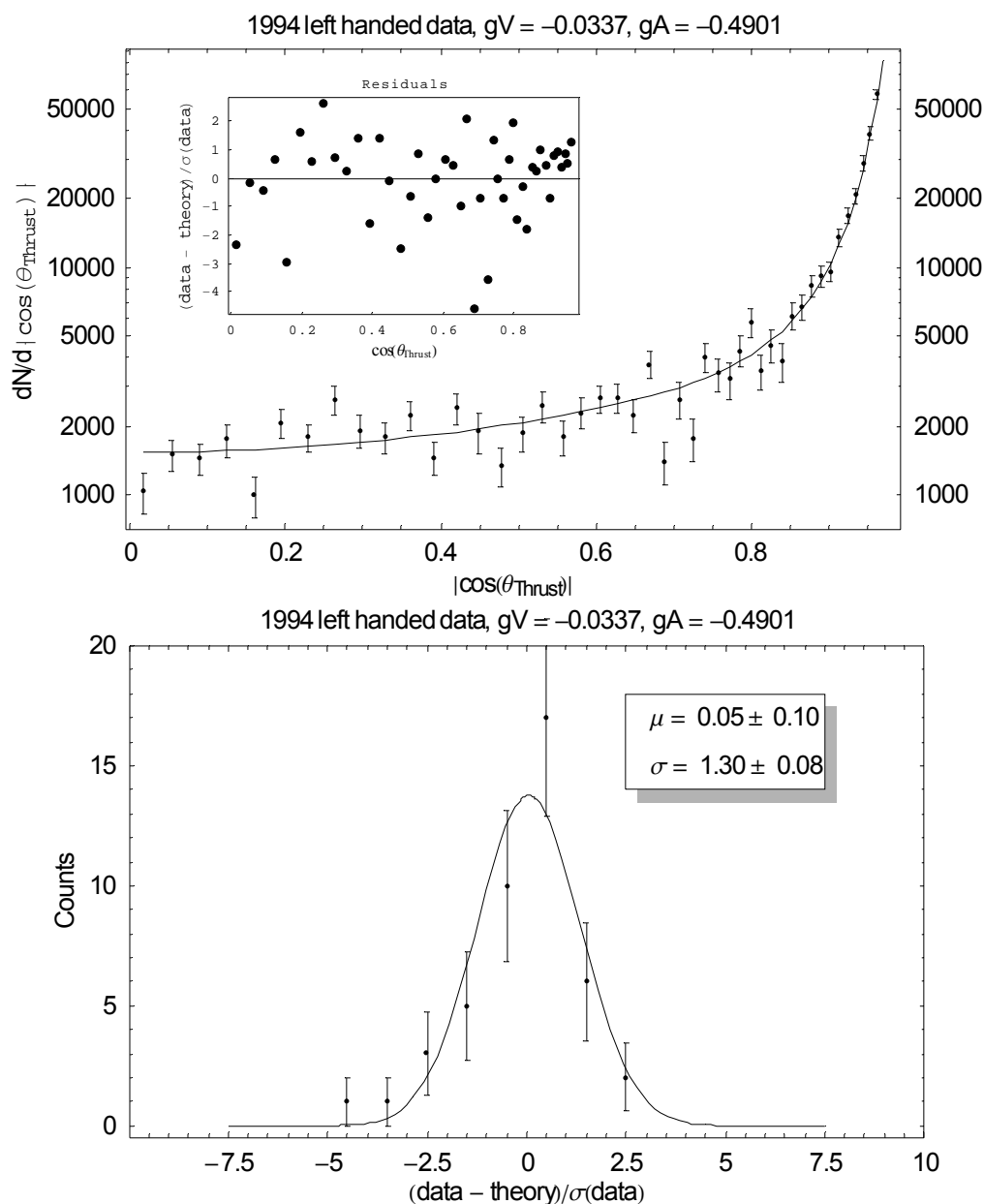


Figure 7-1 1994 left-handed data overlaid with the theoretical model. The top plot shows the binned data with statistical error bars using LAC tower boundaries. The solid line is the analytical expression of the theoretical wide-angle Bhabha differential cross section using the results from the extended log-likelihood fit. The inset shows the residuals as a function of $|\cos \theta_{\text{Thrust}}|$. The bottom plot shows the distribution of residuals as points with associated error bars overlaid with a Gaussian fit (solid line). The results of the Gaussian fit show a mean near zero and a standard deviation near one, as expected.

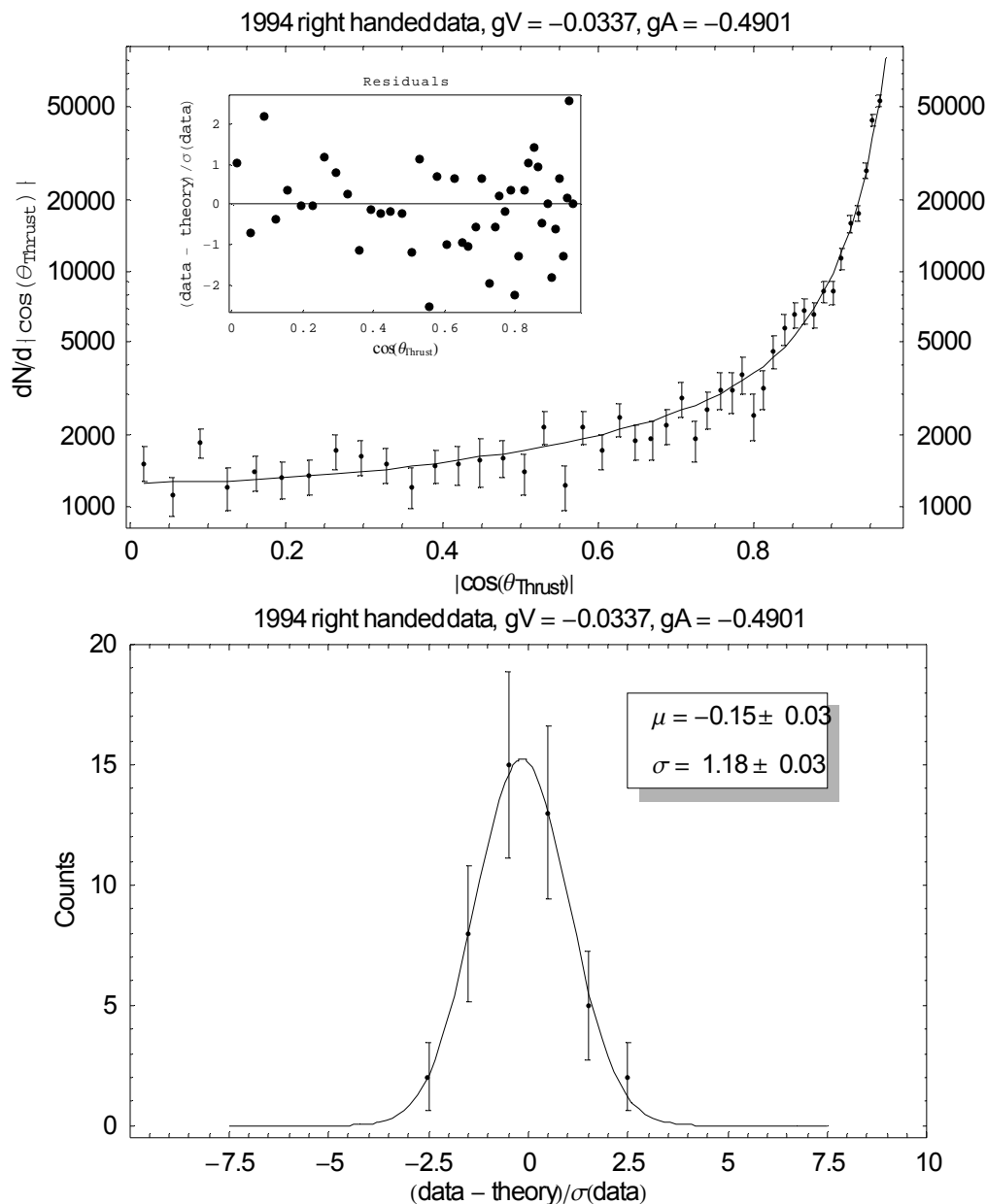


Figure 7-2 1994 right-handed data overlaid with the theoretical model. The top plot shows the binned data with statistical error bars using LAC tower boundaries. The solid line is the analytical expression of the theoretical wide-angle Bhabha differential cross section using the results from the extended log-likelihood fit. The inset shows the residuals as a function of $|\cos \theta_{\text{Thrust}}|$. The bottom plot shows the distribution of residuals as points with associated error bars overlaid with a Gaussian fit (solid line). The results of the Gaussian fit show a mean near zero and a standard deviation near one, as expected.

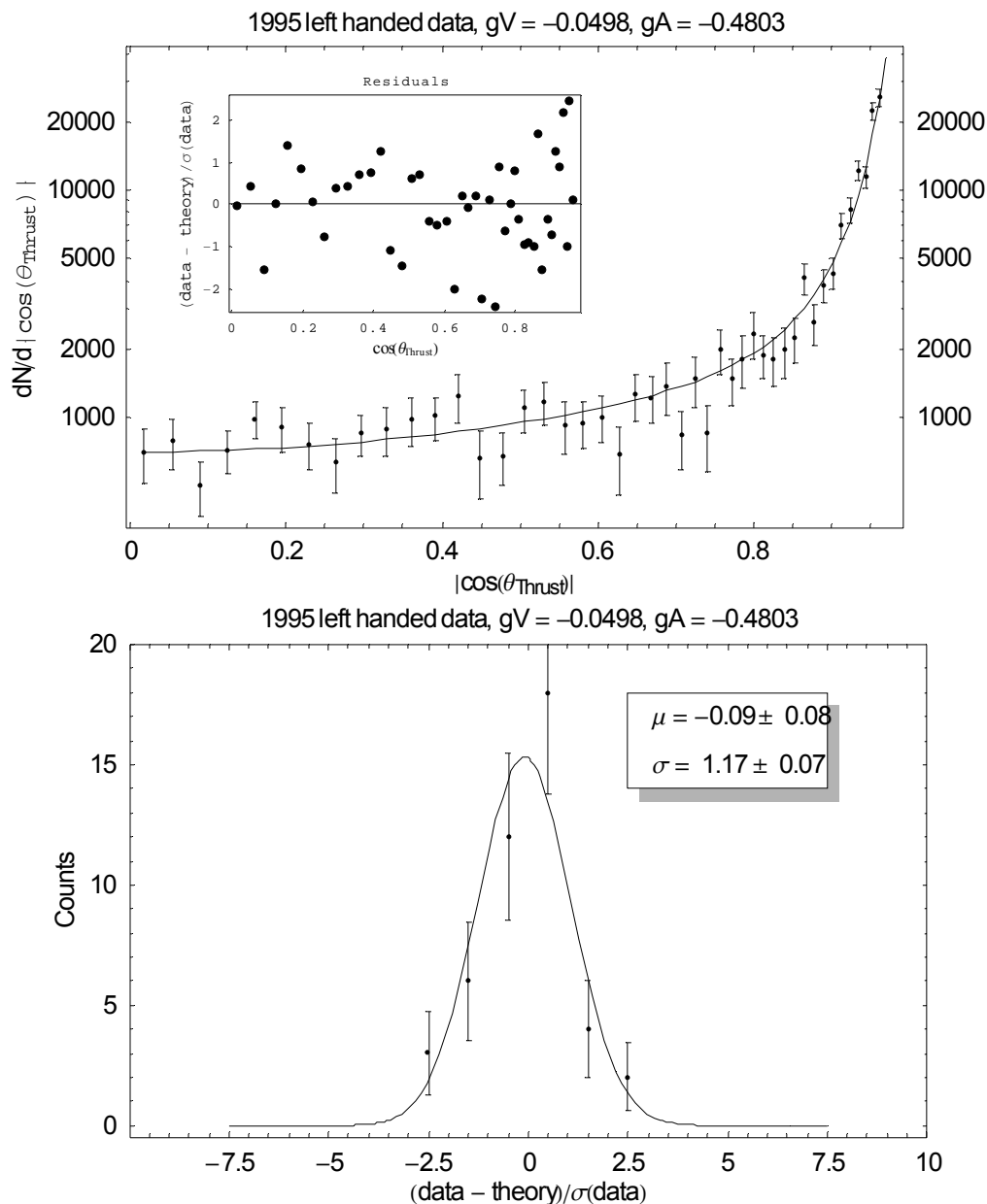


Figure 7-3 1995 left-handed data overlaid with the theoretical model. The top plot shows the binned data with statistical error bars using LAC tower boundaries. The solid line is the analytical expression of the theoretical wide-angle Bhabha differential cross section using the results from the extended log-likelihood fit. The inset shows the residuals as a function of $|\cos \theta_{\text{Thrust}}|$. The bottom plot shows the distribution of residuals as points with associated error bars overlaid with a Gaussian fit (solid line). The results of the Gaussian fit show a mean near zero and a standard deviation near one, as expected.

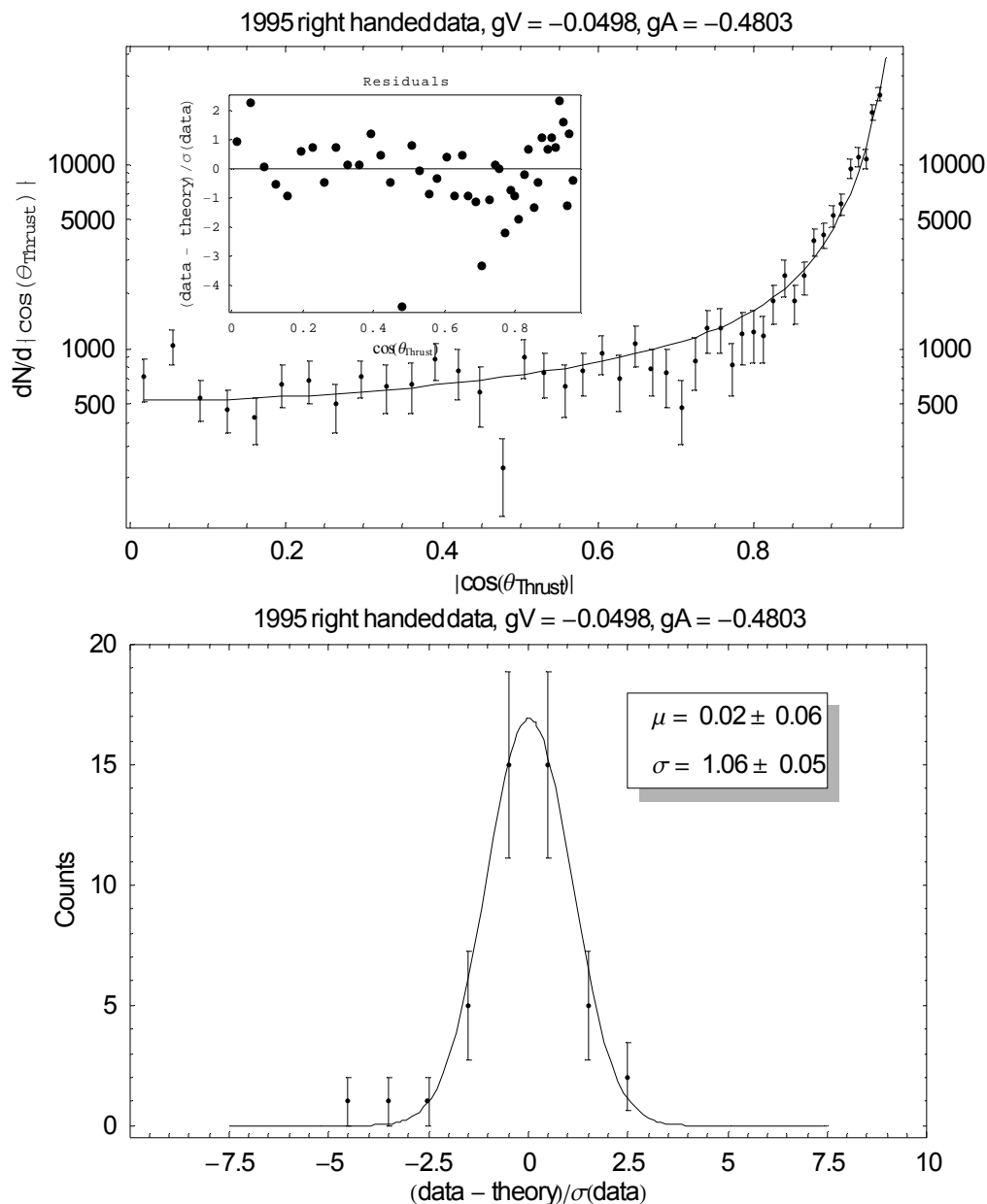


Figure 7-4 1995 right-handed data overlaid with the theoretical model. The top plot shows the binned data with statistical error bars using LAC tower boundaries. The solid line is the analytical expression of the theoretical wide-angle Bhabha differential cross section using the results from the extended log-likelihood fit. The inset shows the residuals as a function of $|\cos \theta_{\text{Thrust}}|$. The bottom plot shows the distribution of residuals as points with associated error bars overlaid with a Gaussian fit (solid line). The results of the Gaussian fit show a mean near zero and a standard deviation near one, as expected.

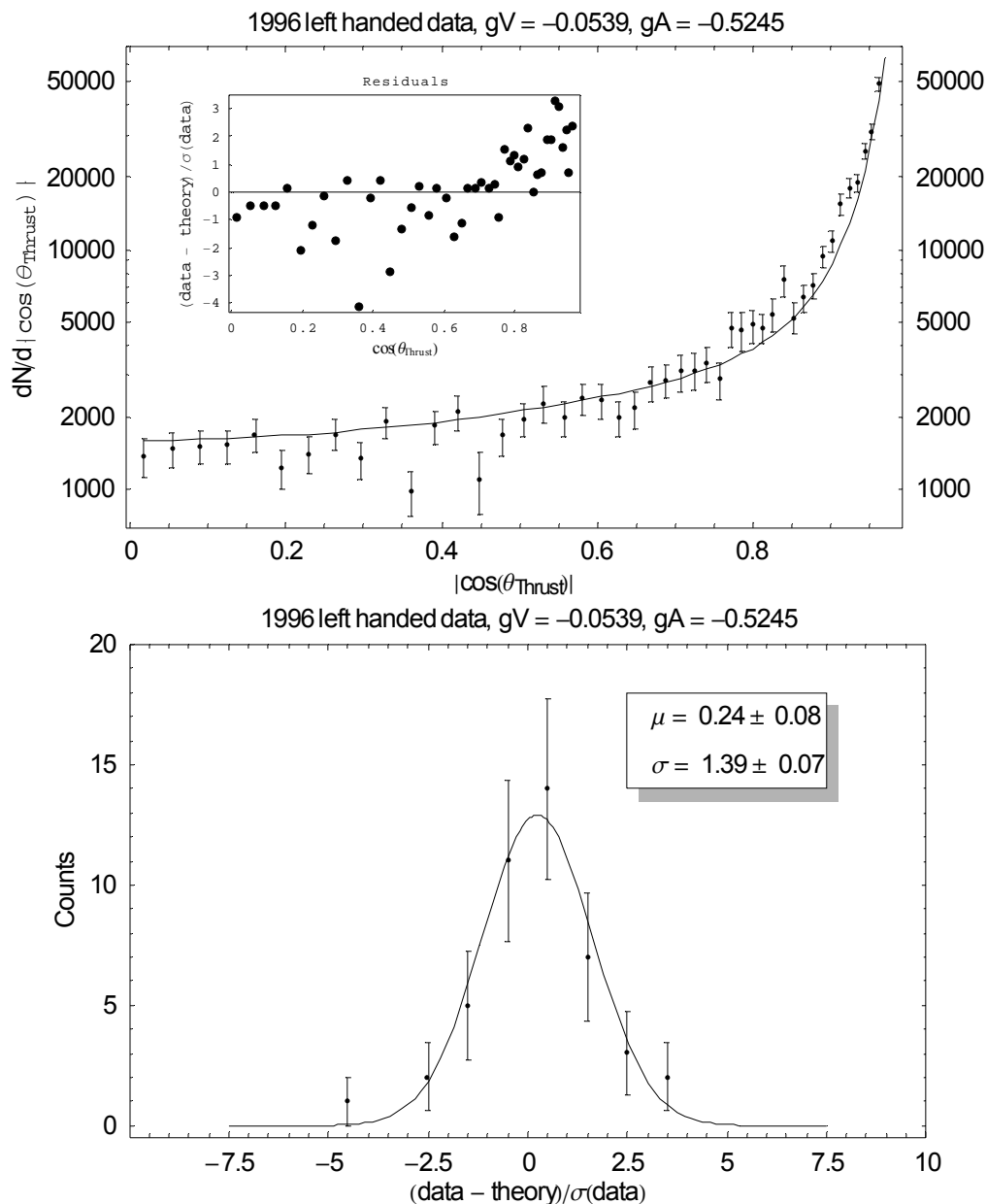


Figure 7-5 1996 left-handed data overlaid with the theoretical model. The top plot shows the binned data with statistical error bars using LAC tower boundaries. The solid line is the analytical expression of the theoretical wide-angle Bhabha differential cross section using the results from the extended log-likelihood fit. The inset shows the residuals as a function of $|\cos \theta_{\text{Thrust}}|$. The bottom plot shows the distribution of residuals as points with associated error bars overlaid with a Gaussian fit (solid line). The results of the Gaussian fit show a mean near zero and a standard deviation near one, as expected.

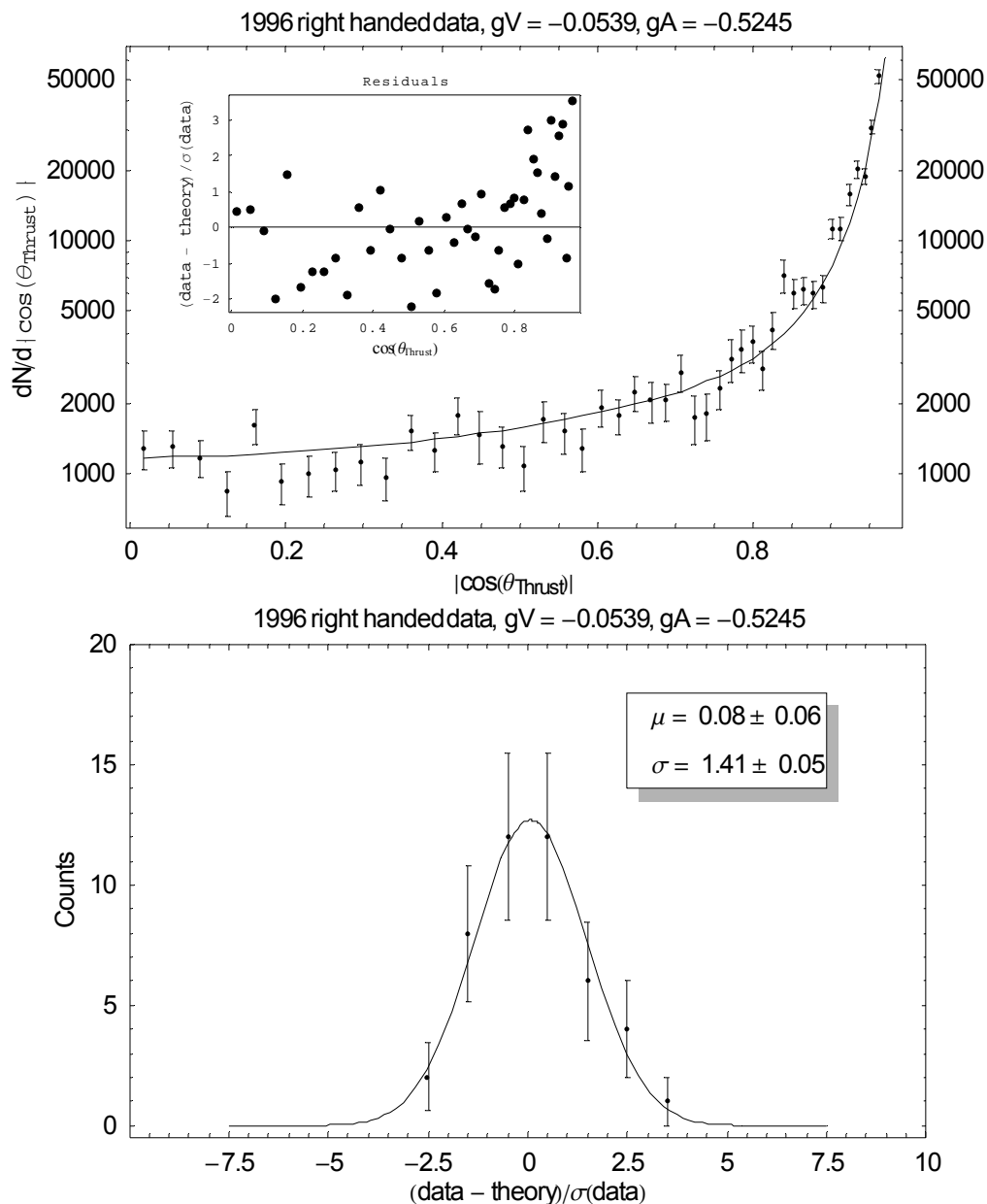


Figure 7-6 1996 right-handed data overlaid with the theoretical model. The top plot shows the binned data with statistical error bars using LAC tower boundaries. The solid line is the analytical expression of the theoretical wide-angle Bhabha differential cross section using the results from the extended log-likelihood fit. The inset shows the residuals as a function of $|\cos \theta_{\text{Thrust}}|$. The bottom plot shows the distribution of residuals as points with associated error bars overlaid with a Gaussian fit (solid line). The results of the Gaussian fit show a mean near zero and a standard deviation near one, as expected.

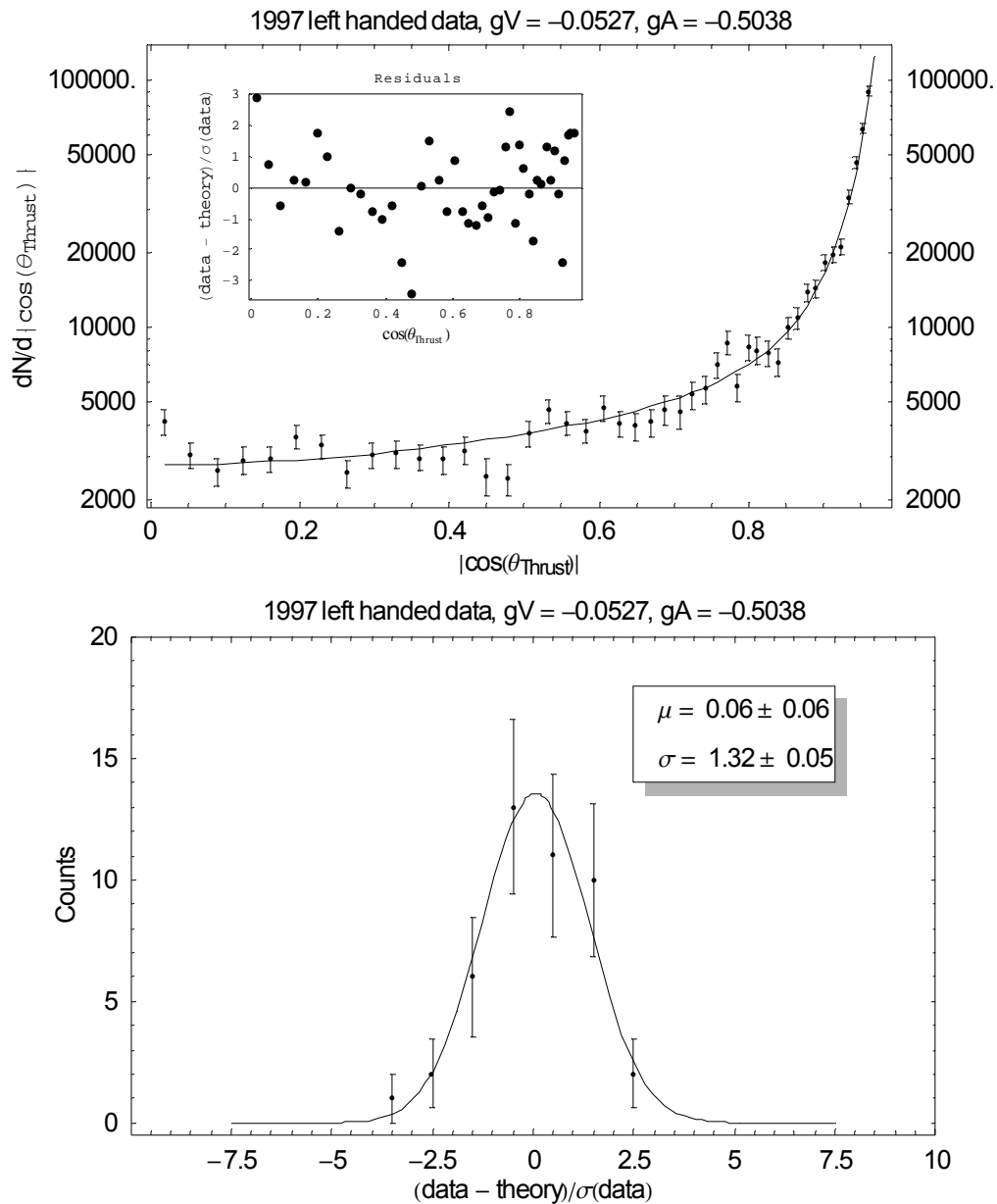


Figure 7-7 1997 left-handed data overlaid with the theoretical model. The top plot shows the binned data with statistical error bars using LAC tower boundaries. The solid line is the analytical expression of the theoretical wide-angle Bhabha differential cross section using the results from the extended log-likelihood fit. The inset shows the residuals as a function of $|\cos \theta_{\text{Thrust}}|$. The bottom plot shows the distribution of residuals as points with associated error bars overlaid with a Gaussian fit (solid line). The results of the Gaussian fit show a mean near zero and a standard deviation near one, as expected.

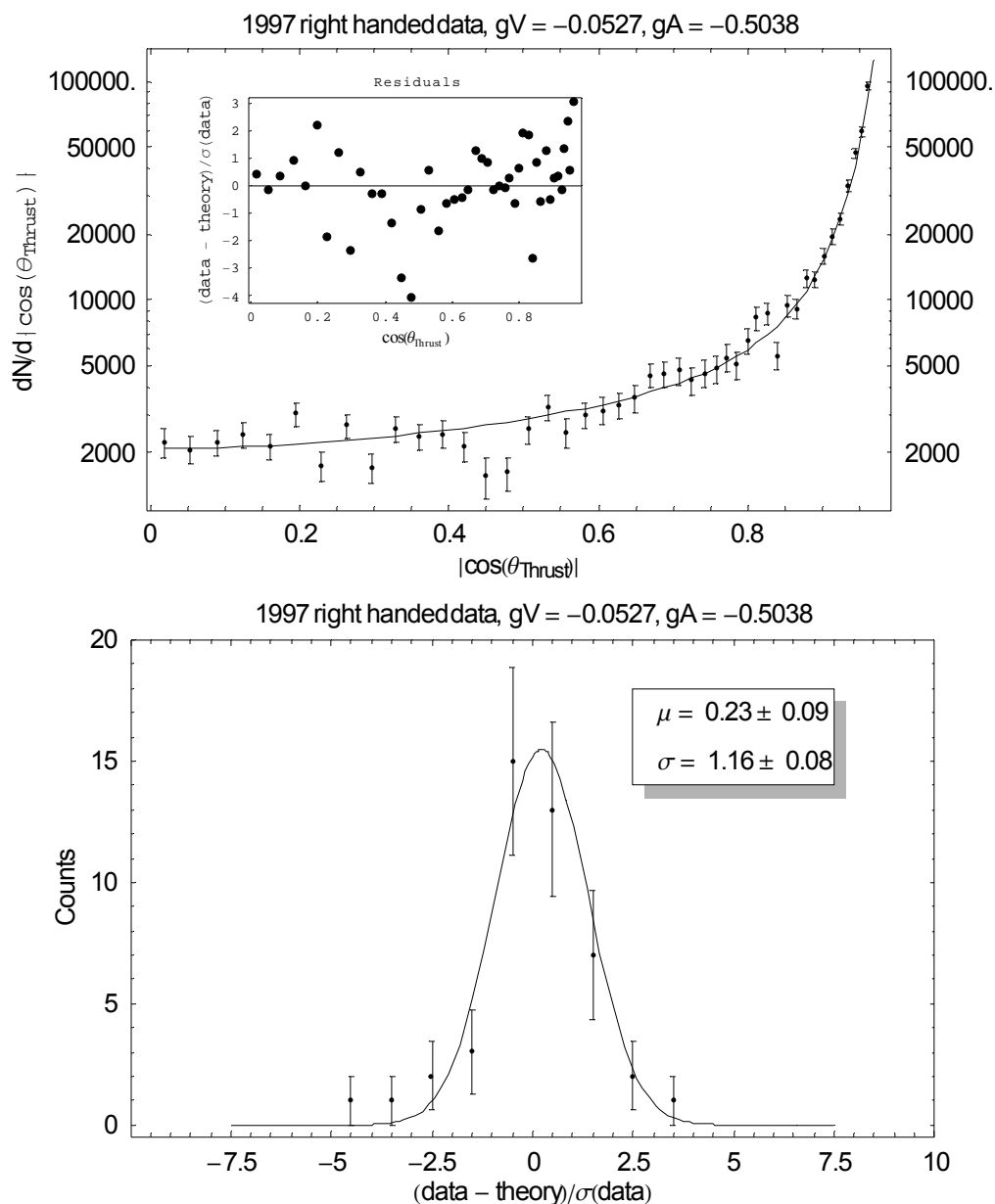


Figure 7-8 1997 right-handed data overlaid with the theoretical model. The top plot shows the binned data with statistical error bars using LAC tower boundaries. The solid line is the analytical expression of the theoretical wide-angle Bhabha differential cross section using the results from the extended log-likelihood fit. The inset shows the residuals as a function of $|\cos \theta_{\text{Thrust}}|$. The bottom plot shows the distribution of residuals as points with associated error bars overlaid with a Gaussian fit (solid line). The results of the Gaussian fit show a mean near zero and a standard deviation near one, as expected.

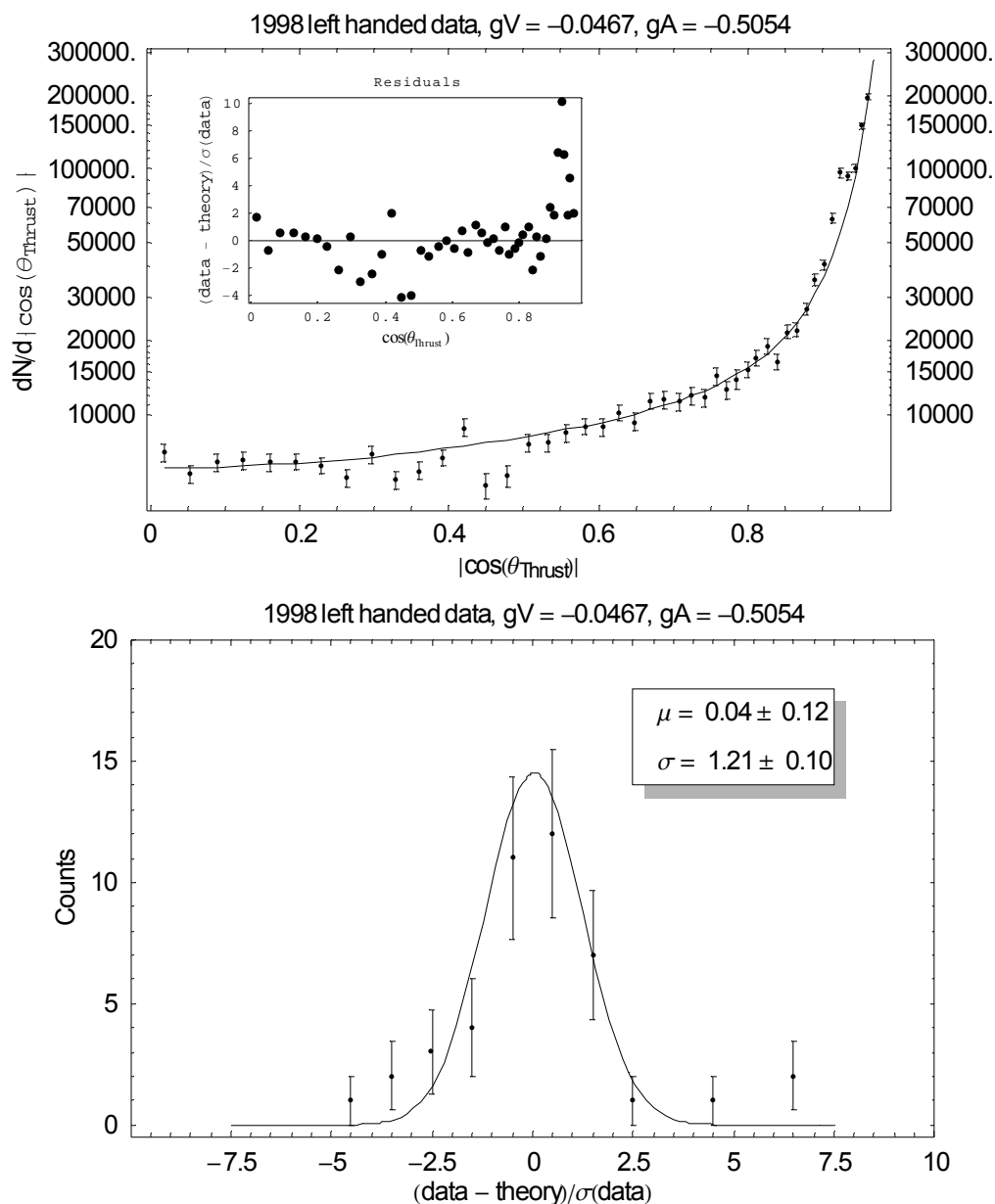


Figure 7-9 1998 left-handed data overlaid with the theoretical model. The top plot shows the binned data with statistical error bars using LAC tower boundaries. The solid line is the analytical expression of the theoretical wide-angle Bhabha differential cross section using the results from the extended log-likelihood fit. The inset shows the residuals as a function of $\cos \theta_{\text{Thrust}}$. The bottom plot shows the distribution of residuals as points with associated error bars overlaid with a Gaussian fit (solid line). The results of the Gaussian fit show a mean near zero and a standard deviation near one, as expected.

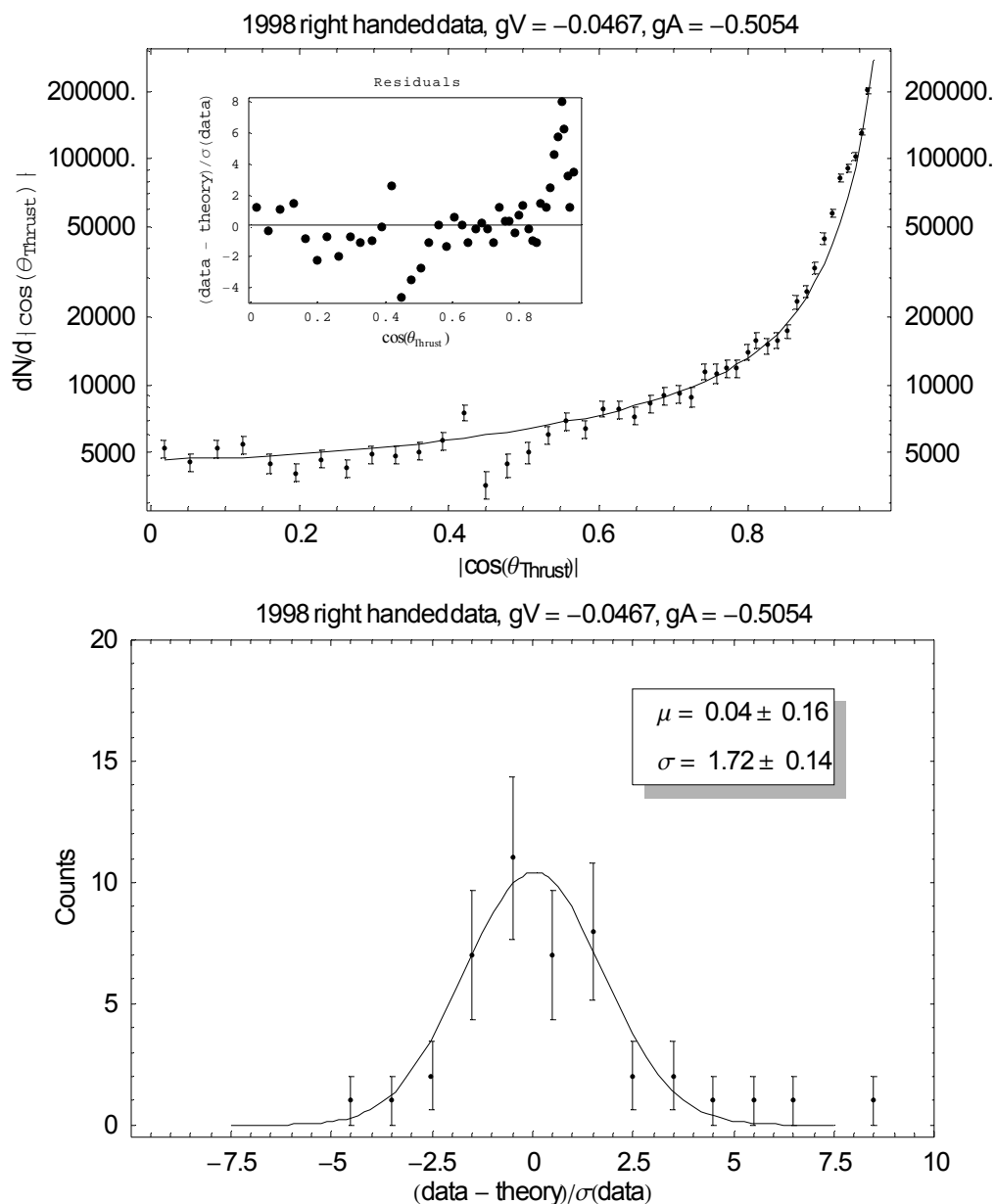


Figure 7-10 1998 right-handed data overlaid with the theoretical model. The top plot shows the binned data with statistical error bars using LAC tower boundaries. The solid line is the analytical expression of the theoretical wide-angle Bhabha differential cross section using the results from the extended log-likelihood fit. The inset shows the residuals as a function of $\cos \theta_{\text{Thrust}}$. The bottom plot shows the distribution of residuals as points with associated error bars overlaid with a Gaussian fit (solid line). The results of the Gaussian fit show a mean near zero and a standard deviation near one, as expected.

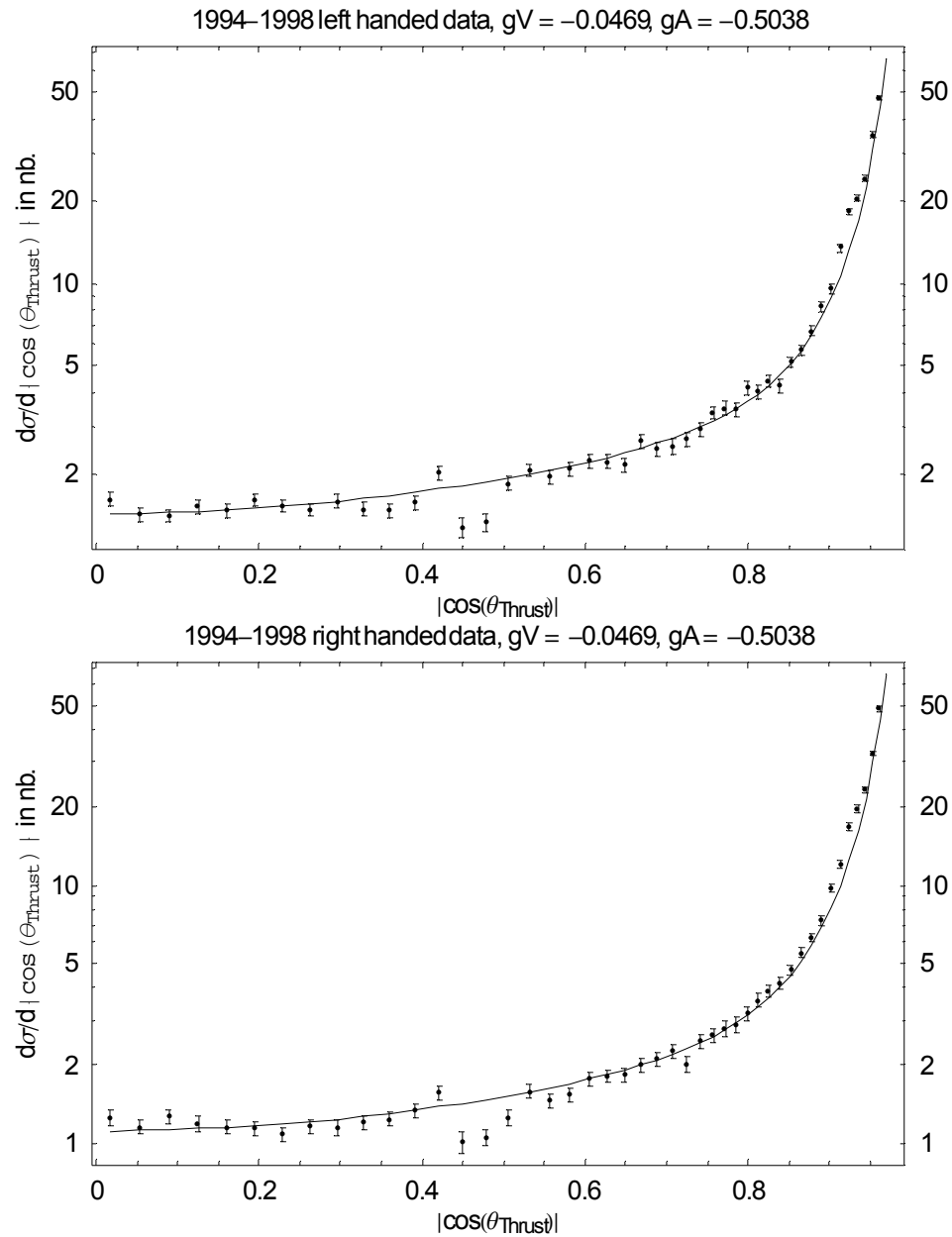


Figure 7-11 Wide-angle Bhabha polarized differential cross section as measured by SLD using the combined result for all SLD run periods, 1994–1998. The points with error bars are corrected WAB events normalized by the luminosity as measured by the LUM. The bins are chosen along LAC tower boundaries. The top plot shows WAB events produced by left-handed electrons, while the bottom plot shows WAB events produced by right-handed electrons. The solid line is the analytical expression of the theoretical wide-angle Bhabha differential cross section using the final combined results for \bar{g}_V^c and \bar{g}_A^c , a luminosity weighted average polarization $P_e = -74\%$ (top plot) and $P_e = +0.74\%$ (bottom plot) and a luminosity weighted average center-of-mass energy $E_{cm} = 91.25$ GeV.

7.4 Systematic Errors

In this section we present a study of the systematic effects that could affect the measurement of \bar{g}_V^e and \bar{g}_A^e . Systematic effects arise due to both uncertainties in the model (due to uncertainties in the free input parameters), and uncertainties in the data. The method used to measure the systematic effects of the free parameters in equations (3.1) through (3.10) is to vary these free parameters, which are listed in Table 3-2, by the size of the uncertainty of each parameter. Additionally, uncertainties are calculated for the efficiency correction model, radiative correction model and of the various luminosity uncertainties that enter by way of equation (7.6). Each source of systematic error is described in detail.

Many of these uncertainties are different and unique for each SLD run period, so it is important to calculate them individually for each run period. In each case, the extended maximum log-likelihood fits are performed by changing each parameter by the size of its uncertainty, and the maximum change in the values of \bar{g}_V^e and \bar{g}_A^e from their central values are taken as the systematic error for that parameter. Since this procedure will result in a unique systematic error for each SLD run period, a global average systematic error is calculated as a luminosity-weighted average of the systematic errors of each SLD run period.

Although we could undertake a study to measure the correlations among each of the input parameters, we instead simply treat them as uncorrelated, which will overestimate their size. This is a reasonable approach since (as will be shown below) each of the systematic errors is small, the approach is conservative and it simplifies the analysis.

The complete list of sources of systematic error and their luminosity weighted average value contribution on the uncertainty on \bar{g}_V^e and \bar{g}_A^e are listed in Table 7-3. The following sections describe each of these systematic errors in detail.

Table 7-3 Sources of systematic errors and their luminosity weighted average contribution to the uncertainty on \bar{g}_V^e and \bar{g}_A^e .

Source of Systematic Uncertainty	 Systematic Error 	
	$\Delta\bar{g}_V^e$	$\Delta\bar{g}_A^e$
Luminosity	0.00005	0.00189
Luminosity Asymmetry	0.00002	0.00001
P_e	0.00026	0.00002
E_{cm}	0.00012	0.00012
E_{cm} width	0.00003	0.00013
Z^0 mass	0.00001	0.00000
Γ_Z	0.00002	0.00023
Efficiency	0.00009	0.00077
Radiative Correction Model	0.00024	0.00376
Total Systematic Error	0.00039	0.00429

7.4.1 Luminosity Uncertainty

The uncertainty in the luminosity comes from the error of the luminosity measurement, and enters via the Poisson term in equation (7.6).

To estimate the size of the uncertainty on the fitted values of \bar{g}_V^e and \bar{g}_A^e due to the uncertainty in the luminosity measurement, we varied the luminosity by plus and minus the size of the total systematic error listed in Table 5-5 above for all run periods and took the largest deviation of the fitted values for \bar{g}_V^e and \bar{g}_A^e as the size of the error for each run period. The luminosity weighted average systematic error due to the uncertainty in the luminosity measurement is ± 0.00005 for \bar{g}_V^e and ± 0.00189 for \bar{g}_A^e .

7.4.2 Luminosity Asymmetry

Another source of uncertainty concerning the luminosity measurement is the asymmetry in the luminosity itself between left-handed beams and right-handed beams. If such a luminosity asymmetry existed, it would induce a false left-right asymmetry that would obviously be reflected in the measurements of the coupling constants in a rather significant way. While the SLC goes to great lengths to insure that equal amounts of luminosity are delivered for both left-handed beams and right-handed beams, the luminosity asymmetry can be measured directly by the LUM using the following equation

$$A_{LR}^{LUM} = \frac{N_L^{eff} - N_R^{eff}}{N_L^{eff} + N_R^{eff}} \quad (7.13)$$

where N_L^{eff} and N_R^{eff} are the number of effective LUM Bhabhas produced by left and right-handed beams, respectively. From the values in Table 5-2 of the effective number of LUM Bhabhas, the luminosity asymmetries for each run period is calculated using equation (7.13) and listed in Table 7-4. From this table it is clear that the measured luminosity asymmetry is very near zero within statistical errors. Another, independent higher-statistics measurement of luminosity asymmetry was performed in which the individual 120 Hz SLC beam records were used[17, 84], which also measured a luminosity asymmetry consistent with zero.

Table 7-4 Luminosity asymmetry as measured by the LUM for each run period. The errors are statistical only.

Run Period	A_{LR}^{LUM}
1993	-0.0042 \pm 0.0029
1994	-0.0030 \pm 0.0025
1995	-0.0030 \pm 0.0036
1996	0.0054 \pm 0.0028
1997	-0.0058 \pm 0.0020
1998	0.0010 \pm 0.0013
Total	-0.0011 \pm 0.0009

Since A_{LR}^{LUM} is so small, we expect the effect on \bar{g}_V^e to be small and on \bar{g}_A^e to be negligible. An increase in the luminosity asymmetry will make the likelihood function increase \bar{g}_V^e slightly since there is no other way for the likelihood function to create an asymmetry since the number of left and right-handed WABs does not change. On the other hand, there is no reason for \bar{g}_A^e to change at all since \bar{g}_A^e is proportional to the total number of WABs, and a luminosity asymmetry does not change the total luminosity. To estimate the size of the effect, we varied the luminosity and refit for \bar{g}_V^e and \bar{g}_A^e and found that the deviation of the fitted values for \bar{g}_V^e and \bar{g}_A^e were small, as expected. We conservatively estimate the luminosity weighted average systematic error due to the luminosity asymmetry to be ± 0.00002 for \bar{g}_V^e and ± 0.00001 for \bar{g}_A^e .

7.4.3 Polarization Uncertainty

Since the polarization varies so slowly relative to the time between polarization measurements, there is a unique polarization measurement for each wide-angle Bhabha event. Therefore, it is possible in principle to incorporate the polarization measurements into

the log-likelihood fits as an observable instead of a parameter (recall that only the per-event sign of the polarization for each beam crossing is used). However, the method we chose to use in the fits was to multiply the per-event sign of the polarization by the absolute value of the mean polarization for each run period as given in Table 4-1. This will result in a slightly larger error for \bar{g}_V^e than a full convolution over the polarization distribution, but still much smaller (by nearly a factor of 7) than the statistical error on \bar{g}_V^e , which is about 5%. This method is also justified since the distribution of polarization measurements are very narrow gaussians and the electron beam polarization enters only linearly in equations (3.1) through (3.10), so that polarization fluctuations above and below the central value for each run period will cancel out.

To estimate the size of the uncertainty on the fitted values of \bar{g}_V^e and \bar{g}_A^e due to the polarization uncertainty, we varied the polarization by the size of the errors in Table 4-1 for all run periods and took the largest deviation of the fitted values for \bar{g}_V^e and \bar{g}_A^e as the size of the systematic error. The luminosity weighted average systematic error due to the uncertainty in the polarization measurement is ± 0.00026 for \bar{g}_V^e and ± 0.00002 for \bar{g}_A^e . The systematic error on \bar{g}_A^e is near 0% as expected.

We should note that with such a high precision polarization measurement it is possible to perform the log-likelihood fits using the per-event polarization errors. Since the uncertainty on \bar{g}_V^e due to the polarization uncertainty is the largest systematic error in this analysis, such an approach is certainly called for if the number of events was larger, as will be the case for physics measurements at the Next Linear Collider, for example. The reason it was not done for this analysis was simply that the statistical error on the measurement of \bar{g}_V^e was so much larger than using the simpler approach, along with a desire to treat all systematic errors simply and uniformly. However, future precision measurements which rely

on detectors like the Compton Polarimeter should use per-event errors in the fits, particularly with the advent of tools such as RooFit[81] which make handling per-event errors almost trivial.

7.4.4 Center-of-Mass Energy

There are two uncertainties that arise in measuring the center-of-mass energy: the average energy of each bunch and the energy profile of each bunch. Both of these affects could influence the measurements of \bar{g}_V^e and \bar{g}_A^e since the beams are tuned to collide at the peak of the Z^0 cross section, which is a very strong and broad Breit-Wigner resonance ($\Gamma_Z = 2.4952$ GeV). Therefore, any deviation of the beam energies from the Z^0 pole will result in different parts of the Z^0 distribution being sampled.

The average bunch energy of each electron and positron beam are each individually measured on a per beam crossing basis by the WISRD. Additionally, the finite energy width of each beam's energy profile is measured by periodically scanning a 15-micron graphite wire through a point of high dispersion in the electron beam and measuring the resulting radiation. The energy width is a very stable parameter of the SLC, so only a few energy width measurements are made during any given run.

Unfortunately, the technique we've used up to this point of refitting the data with a modified model by changing the free parameters of interest in the Born level expression given by equation (3.11) cannot be used in this case, because we have been assuming that the center-of-mass energy is fixed. It may be the case that the radiative correction coefficients encapsulated in ϵ_1 , ϵ_2 and ϵ_3 have an energy dependence that would not be taken into account by simple scalar quantities. Therefore, we are not justified in using the technique described in

section 3.2 which used the UNIBAB Monte Carlo since we require a model that explicitly includes the energy dependence in the radiative correction coefficients, $c_1(E_{\text{cm}})$, $c_2(E_{\text{cm}})$ and $c_3(E_{\text{cm}})$.

We therefore use dMIBA[18], a semi-analytical Fortran 77 program that dresses the 10 lowest order Born level terms given in equations (3.1) through (3.10) with all of the important radiative corrections discussed in section 3.2. In many ways it is superior to our method of dressing the 10 lowest order Born level terms with 3 simple constants to incorporate the radiative corrections because in addition to correctly handling the center-of-mass energy, it incorporates our event selection criteria by performing numerical integrations over the phase space of our event selection cuts while still preserving the lowest order analytical expressions. The reasons we did not use dMIBA for the entire wide-angle Bhabha analysis was due to its computationally intensive nature and the appealing simplicity of our tree level method. Even though dMIBA is semi-analytical, computationally it is still an order of magnitude slower than our tree level expression with three simple constants.

The original dMIBA program did not include the effects of polarization when it was written, but due to dMIBA's semi-analytical nature it was straight forward to identify the 10 lowest order Born level terms before they were dressed with radiative corrections (in subroutine `sdi f`) and modify them to include polarization according to equations (3.1) through (3.10).

The center-of-mass energy as measured by the WISRD is given in Table 4-2, from which it is seen that the uncertainty for all of the run periods ranges between 25 MeV and 30 MeV. To estimate the size of the uncertainty on the fitted values of \bar{g}_V^e and \bar{g}_A^e due to the center-of-mass energy uncertainty, we varied the center-of-mass energy by the size of the errors in Table 4-2 for the all run periods and took the largest deviation of the fitted values

for \bar{g}_V^e and \bar{g}_A^e as the size of the systematic error. The luminosity weighted average systematic error due to the uncertainty in the center-of-mass energy measurement is ± 0.00012 for \bar{g}_V^e and ± 0.00012 for \bar{g}_A^e .

The center-of-mass energy width for each run as measured by the wire scans are also given in Table 4-2. We are not justified to use the same technique to estimate the systematic error due to the finite center-of-mass energy width as we did for the center-of-mass energy uncertainty because the beam profile is fixed for every collision. Whereas a colliding electron and positron could have any energy within the range of energies given by the measurement of the energy uncertainty for any given beam crossing, the finite beam energy width profile only tells us the relative amounts of off energy collisions during a given run period. Therefore, the proper way to estimate the size of the uncertainty on the fitted values of \bar{g}_V^e and \bar{g}_A^e due to the center-of-mass energy width is to convolve the energy width distribution with the dMIBA p.d.f.. Although this is possible in principle, the computational time needed to perform this convolution would be enormous. We therefore take a simpler approach by simply performing our extended log-likelihood fit using dMIBA at a discrete set of energy points over the gaussian beam energy profile to estimate the convolution.

We refit the dataset for each run period using the dMIBA p.d.f. at the five different energy points given in Table 4-2. The resulting five values of \bar{g}_V^e and five values of \bar{g}_A^e as a function of E_{cm} are then each fit to a cubic polynomial which is then convolved with a gaussian with a mean and standard deviation equal to the E_{cm} and $E_{cm} + E_{cm}^{width}$, respectively, for the given run period. The results for the 1997 dataset are shown in Figure 7-12.

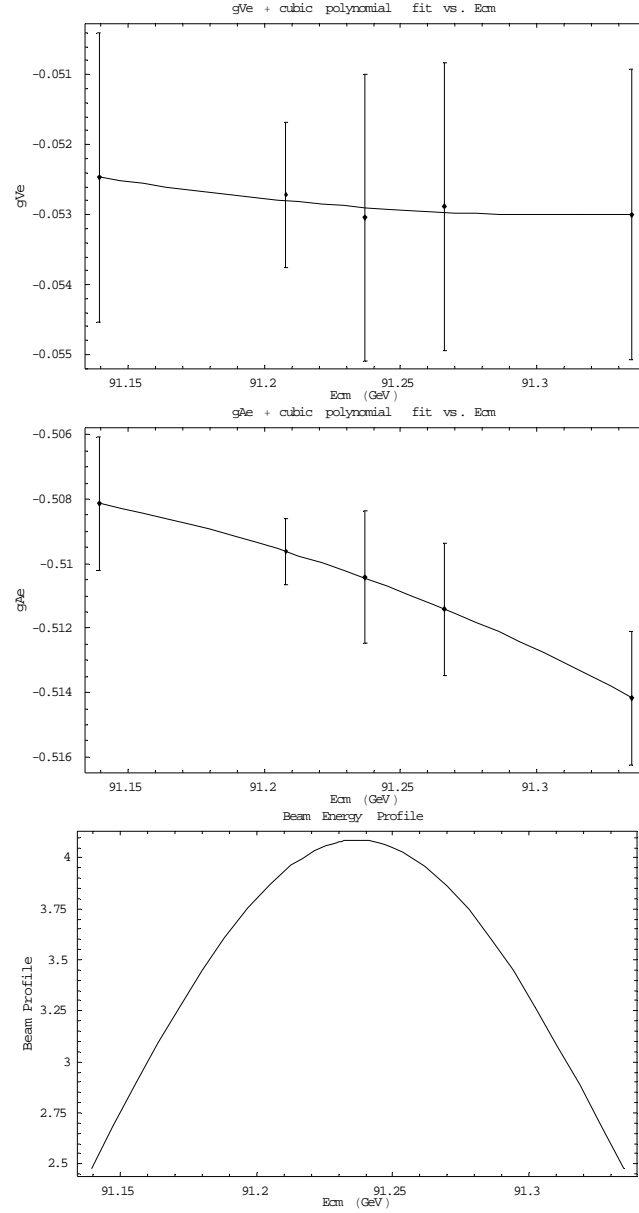


Figure 7-12 **dMIBA** is used to refit values of \bar{g}_V^c and \bar{g}_A^c for five different center-of-mass energies: E_{cm}^0 , $E_{cm}^0 \pm \delta E_{cm}$ and $E_{cm}^0 \pm E_{cm}^{width}$. These new values of \bar{g}_V^c and \bar{g}_A^c are then fit to a cubic polynomial which is then convolved with a gaussian with $\mu = E_{cm}^0$ and $\sigma = E_{cm}^{width}$. The E_{cm} data used is from the 1997 run period, and our results are representative of the entire SLD dataset.

The results of these convolutions for each run period are shown in Table 7-5.

Table 7-5 Results of convoluting $\bar{g}_v^e(E_{cm})$ and $\bar{g}_A^e(E_{cm})$ with the gaussian E_{cm} width distribution for each run period.

Convolutions with E_{cm} Distributions		
Run Period	\bar{g}_v^e	\bar{g}_A^e
1994	-0.03410	-0.49806
1995	-0.05031	-0.48800
1996	-0.05445	-0.53235
1997	-0.05285	-0.51065
1998	-0.04693	-0.51246

In principle, we should convolve all of our fits with the E_{cm} distribution in this manner (some 92 independent fits in all). However, using the convolution method just described would require using dMIBA for all of the fits, totaling $92 \times 5 = 460$ fits, which is simply an unreasonable amount of CPU time with the current technology²⁷. Instead, we use the results in Table 7-5 above to correct the final fit results listed in Table 7-1. These corrections are listed in Table 7-6.

²⁷ All data analysis, including the log-likelihood fits, were performed on a Dell Latitude C400 laptop (1 Pentium III CPU clocking at 1.2 GHz) running Microsoft Windows XP Professional.

Table 7-6 Corrections to be applied to \bar{g}_V^e and \bar{g}_A^e to account for finite E_{cm} width.

E_{cm} Width Corrections		
Run Period	$\Delta\bar{g}_V^e$	$\Delta\bar{g}_A^e$
1994	-0.00033	0.00019
1995	0.00002	0.00017
1996	0.00001	0.00020
1997	-0.00019	0.00023
1998	0.00003	0.00033

We take half the size of the corrections as the systematic error due to the finite energy width of the beams. This conservative technique will only slightly overestimate the systematic error since we are treating the results of the convolution fits as uncorrelated with the non-convoluted fits. The luminosity weighted average systematic error due to the finite energy width of the beams is ± 0.00003 for \bar{g}_V^e and ± 0.00013 for \bar{g}_A^e .

7.4.5 Z^0 Mass Uncertainty

The Z^0 mass and its uncertainty come from the LEP Z^0 line shape fit[7]. To estimate the size of the uncertainty on the fitted values of \bar{g}_V^e and \bar{g}_A^e due to the uncertainty of the Z^0 mass, we varied the Z^0 mass by ± 2.1 MeV for all run periods and took the largest deviation of the fitted values for \bar{g}_V^e and \bar{g}_A^e as the size of the systematic error. The luminosity weighted average systematic error due to the uncertainty in the Z^0 mass is ± 0.00001 for \bar{g}_V^e and ± 0.00000 for \bar{g}_A^e .

7.4.6 Z^0 Width Uncertainty

The Z^0 width and its uncertainty come from the LEP Z^0 line shape fit[7]. To estimate the size of the uncertainty on the fitted values of \overline{g}_V^e and \overline{g}_A^e due to the uncertainty of the Z^0 width, we varied the Z^0 width by ± 2.3 MeV for all run periods and took the largest deviation of the fitted values for \overline{g}_V^e and \overline{g}_A^e as the size of the systematic error. The luminosity weighted average systematic error due to the uncertainty in the Z^0 width is ± 0.00002 for \overline{g}_V^e and ± 0.00023 for \overline{g}_A^e .

7.4.7 Radiative Correction Model

To estimate the systematic error due to modeling the radiative corrections presented in section 3.2, the value of \overline{g}_V^e and \overline{g}_A^e in Table 7-1 for the Maximum Likelihood fit of the 1997 SLD dataset (the beam parameters of which were used to generate the UNIBAB dataset) were used to recalculate new values of the radiative correction coefficients, the results of which were $\epsilon_1 = -0.0581$, $\epsilon_2 = 0.7180$ and $\epsilon_3 = 0.8597$. These new values of the radiative correction coefficients were then used to refit the SLD datasets for all run periods, and we took the largest deviation of the fitted values for \overline{g}_V^e and \overline{g}_A^e as the size of the systematic error. The luminosity weighted average systematic error due to the uncertainty in modeling the radiative corrections is ± 0.00024 for \overline{g}_V^e and ± 0.00376 for \overline{g}_A^e .

7.4.8 Efficiency Correction

To estimate the size of the uncertainty on the fitted values of \overline{g}_V^e and \overline{g}_A^e due to the uncertainties in the Pseudo Event efficiency modeling technique discussed in section 6.5.1

above, the value of each correction factor was randomly varied by ± 1 standard deviation of the binomial error for each calorimeter tower, and these new values were then used to refit the SLD datasets from all run periods. This approach was performed multiple times for all run periods, and we took the largest deviation of the fitted values for \bar{g}_V^e and \bar{g}_A^e as the size of the systematic error. The luminosity weighted average systematic error due to the uncertainties in the Pseudo Event efficiency modeling technique is ± 0.00009 for \bar{g}_V^e and ± 0.00077 for \bar{g}_A^e .

7.4.9 Systematic Error Summary

The systematic errors are summarized in Table 7-3.

The largest systematic error for \bar{g}_V^e , contributing 0.56% to the total systematic error, is due to the uncertainty in the measured value of the polarization. This is understandable as \bar{g}_V^e is such a sensitive function of the polarization. The SLD Polarimeter has been well modeled to arrive at this error estimation. The next largest contribution for the uncertainty in \bar{g}_V^e is the uncertainty in the model of the radiative corrections, which contributes 0.50% to the total systematic uncertainty. It might be possible to reduce this error by using dMIBA to perform all of the fits, since then the radiative corrections to the tree-level diagrams are handled explicitly. However, this would require more computational resources.

The largest systematic error for \bar{g}_A^e , contributing 0.75% to the total systematic uncertainty, is again due to the uncertainty in the model of the radiative corrections. This constitutes 88% of the total systematic error. Clearly, this analysis could benefit from using dMIBA to perform all of the fits. The next largest systematic error comes in at a distant

second and is due to the uncertainty in the luminosity measurement, which contributes 0.38% to the total systematic error.

7.5 Final Measurement of \bar{g}_V^e and \bar{g}_A^e

The final results for \bar{g}_V^e and \bar{g}_A^e are calculated by applying the corrections due to the finite E_{cm} width in Table 7-6 to the fit results in Table 7-1. By incorporating the systematic errors listed in Table 7-3, our results are

$$\bar{g}_V^e = -0.0469 \pm 0.0024 \text{ (stat.)} \pm 0.0004 \text{ (sys.)}$$

$$\bar{g}_A^e = -0.5038 \pm 0.0010 \text{ (stat.)} \pm 0.0043 \text{ (sys.)}$$

7.6 Comparison to the Standard Model

Our results for \bar{g}_V^e and \bar{g}_A^e from section 7.5 above may be compared to the Standard Model predictions calculated by ZFITTER (see section 3.2 above) of $\bar{g}_V^e = -0.03657$ and $\bar{g}_A^e = -0.50134$, which were calculated using $M_{\text{top}} = 175$ GeV and $M_H = 150$ GeV. A useful way to compare our measurement to the Standard Model is to define an angular dependent version of A_{LR} for wide-angle Bhabha scattering:

$$A_{\text{LR}}^{e^+e^-}(|\cos\theta|) = \frac{\partial_{|\cos\theta|}\sigma_L - \partial_{|\cos\theta|}\sigma_R}{\partial_{|\cos\theta|}\sigma_L + \partial_{|\cos\theta|}\sigma_R} \quad (7.14)$$

where $\partial_{|\cos\theta|}\sigma_{L,R}$ is the differential cross section for wide-angle Bhabha scattering for left (L) and right (R) handed initial state electrons. Equation (7.14) is analogous to equation (2.13) but uses the wide-angle Bhabha differential cross section in place of σ .

Figure 7-13 is a plot of $A_{LR}^{e^+e^-}(|\cos\theta_{Thrust}|)$ vs. $|\cos\theta_{Thrust}|$ for the entire 1994-1998 WAB dataset, and is overlaid with two curves of $A_{LR}^{e^+e^-}(|\cos\theta|)$ using two different values of \bar{g}_V^e and \bar{g}_A^e . The upper curve uses our final measurement of \bar{g}_V^e and \bar{g}_A^e from section 7.5 above, and the lower dashed curve uses the values of \bar{g}_V^e and \bar{g}_A^e calculated by ZFITTER. The data were binned using KAL tower boundaries and scaled using the luminosity weighted polarization $P_e = 74\%$ according to equation (2.14).

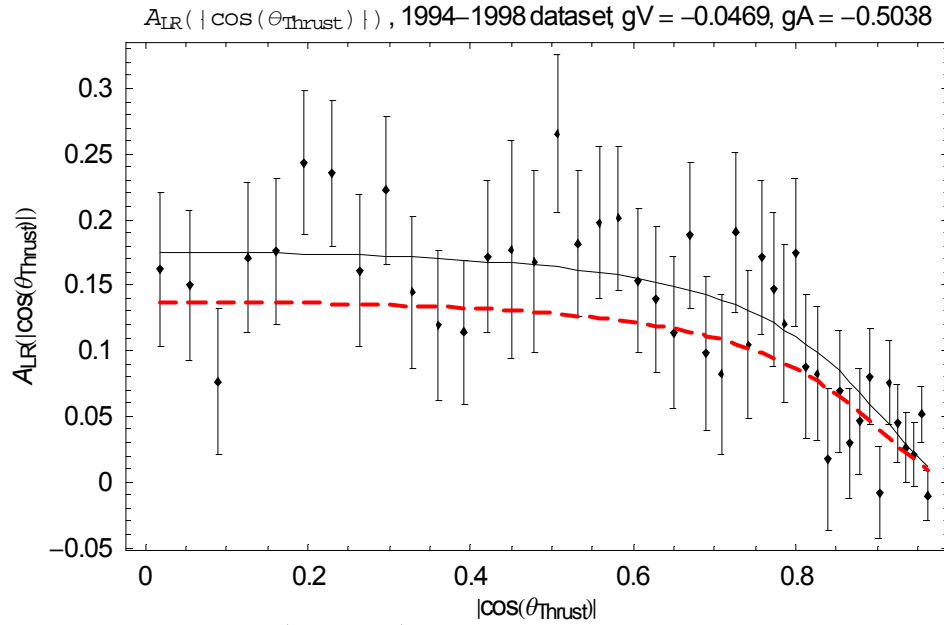


Figure 7-13 $A_{LR}^{e^+e^-}(|\cos\theta_{Thrust}|)$ vs. $|\cos\theta_{Thrust}|$ for the entire 1994-1998 WAB dataset. The upper solid curve uses our final results of $\bar{g}_V^e = -0.0469$ and $\bar{g}_A^e = -0.5038$. The lower dashed curve uses Standard Model predictions from ZFITTER of $\bar{g}_V^e = -0.03657$ and $\bar{g}_A^e = -0.50134$.

Figure 7-14 shows the residual distributions for each curve overlaid with a fit to a gaussian. The middle plot in the figure shows the residual distribution for our final result, which shows excellent agreement with the data. The lower plot in the figure is the residual distribution for the Standard Model prediction, which is inconsistent with the data.

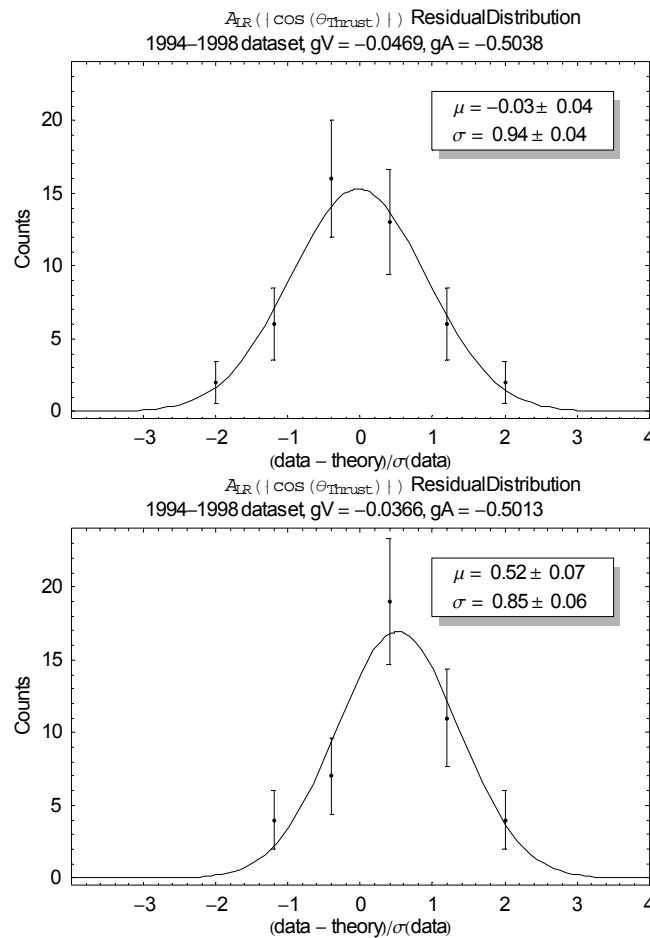


Figure 7-14 Residual distributions for Figure 7-13. The top plot shows the distribution of residuals for our final result, which is fit to a gaussian and shows good agreement with the data, having a mean consistent with zero and a standard deviation near one. The bottom plot shows the residual distribution for the Standard Model prediction, which is inconsistent with the data.

CHAPTER 8 CONCLUSION

This dissertation presented a measurement of the two Z^0 coupling parameters to the electron based on polarized wide-angle Bhabha scattered events ($e^+e^- \rightarrow e^+e^-$) from the 1994-1998 SLD datasets. We developed a Maximum Likelihood fitting technique which allowed the use of all Bhabha scattered events from the full angular acceptance of SLD's calorimeters in a natural way, including the large-angle region where the Z^0 resonance dominates and the small-angle region used for luminosity measurements where t-channel photon exchange dominates.

We measure

$$\bar{g}_V^e = -0.0469 \pm 0.0024 \text{ (stat.)} \pm 0.0004 \text{ (sys.)}$$

$$\bar{g}_A^e = -0.5038 \pm 0.0010 \text{ (stat.)} \pm 0.0043 \text{ (sys.)}$$

which, using equation (2.11), represents a measurement of the effective weak mixing angle of

$$\sin^2 \theta_W^{\text{eff}} = 0.2267 \pm 0.0012 \text{ (stat.)} \pm 0.0003 \text{ (sys.)}$$

The measurement uncertainty of \bar{g}_A^e is limited by the 0.85% systematic error, which is itself dominated by the uncertainty in the method used to model the radiative corrections (which contribute 0.75% to the total systematic error) and the uncertainty introduced by the luminosity measurement (which contributes 0.38% to the total systematic error).

We also measured the luminosity for the 1993-1998 SLD run period to be

$$\mathcal{L} = 19,247 \pm 17(\text{stat.}) \pm 146(\text{sys.}) \text{ nb}^{-1}$$

This measurement is limited by the 0.76% systematic error, which is composed of 0.70% experimental error and 0.30% theoretical uncertainty. This level of precision is significantly better than the design goal of 3%[43].

The LEP experiments do not have polarized electron beams, but measure \bar{g}_V^e and \bar{g}_A^e using a different technique by combining the lepton forward-backward asymmetries, tau polarization and the electron partial width Γ_{ee} to yield a measurement of $\bar{g}_V^e = -0.0378 \pm 0.0011$ and $\bar{g}_A^e = -0.50112 \pm 0.00035$ [7]. Our measurement of \bar{g}_A^e agrees with LEP, but our result for \bar{g}_V^e differs by over three standard deviations.

Our measurement of \bar{g}_A^e agrees with the Standard Model, but our measurement of \bar{g}_V^e differs from the Standard Model by four standard deviations.

APPENDIX A SLD COLLABORATION

Kenji Abe,⁽¹⁵⁾ Koya Abe,⁽²⁴⁾ T. Abe,⁽²¹⁾ I. Adam,⁽²¹⁾ H. Akimoto,⁽²¹⁾
 D. Aston,⁽²¹⁾ K.G. Baird,⁽¹¹⁾ C. Baltay,⁽³⁰⁾ H.R. Band,⁽²⁹⁾ T.L. Barklow,⁽²¹⁾
 J.M. Bauer,⁽¹²⁾ G. Bellodi,⁽¹⁷⁾ R. Berger,⁽²¹⁾ G. Blaylock,⁽¹¹⁾ J.R. Bogart,⁽²¹⁾
 G.R. Bower,⁽²¹⁾ J.E. Brau,⁽¹⁶⁾ M. Breidenbach,⁽²¹⁾ W.M. Bugg,⁽²³⁾
 T.H. Burnett,⁽²⁸⁾ P.N. Burrows,⁽¹⁷⁾ A. Calcaterra,⁽⁸⁾ R. Cassell,⁽²¹⁾
 A. Chou,⁽²¹⁾ H.O. Cohn,⁽²³⁾ J.A. Coller,⁽⁴⁾ M.R. Convery,⁽²¹⁾
 R.F. Cowan,⁽¹³⁾ G. Crawford,⁽²¹⁾ C.J.S. Damerell,⁽¹⁹⁾ M. Daoudi,⁽²¹⁾
 N. de Groot,⁽²⁾ R. de Sangro,⁽⁸⁾ D.N. Dong,⁽²¹⁾ M. Doser,⁽²¹⁾ R. Dubois,⁽²¹⁾
 I. Erofeeva,⁽¹⁴⁾ V. Eschenburg,⁽¹²⁾ S. Fahey,⁽⁵⁾ D. Falciari,⁽⁸⁾
 J.P. Fernandez,⁽²⁶⁾ K. Flood,⁽¹¹⁾ R. Frey,⁽¹⁶⁾ E.L. Hart,⁽²³⁾ K. Hasuko,⁽²⁴⁾
 S.S. Hertzbach,⁽¹¹⁾ M.E. Hu_{er},⁽²¹⁾ M. Iwasaki,⁽¹⁶⁾ D.J. Jackson,⁽¹⁹⁾
 P. Jacques,⁽²⁰⁾ J.A. Jaros,⁽²¹⁾ Z.Y. Jiang,⁽²¹⁾ A.S. Johnson,⁽²¹⁾
 J.R. Johnson,⁽²⁹⁾ R. Kajikawa,⁽¹⁵⁾ M. Kalelkar,⁽²⁰⁾ H.J. Kang,⁽²⁰⁾
 R.R. Kofler,⁽¹¹⁾ R.S. Kroeger,⁽¹²⁾ M. Langston,⁽¹⁶⁾ D.W.G. Leith,⁽²¹⁾
 V. Lia,⁽¹³⁾ C. Lin,⁽¹¹⁾ G. Mancinelli,⁽²⁰⁾ S. Manly,⁽³⁰⁾ G. Mantovani,⁽¹⁸⁾
 T.W. Markiewicz,⁽²¹⁾ T. Maruyama,⁽²¹⁾ A.K. McKemey,⁽³⁾ R. Messner,⁽²¹⁾
 K.C. Mo_{er},⁽²¹⁾ T.B. Moore,⁽³⁰⁾ M. Morii,⁽²¹⁾ D. Muller,⁽²¹⁾ V. Murzin,⁽¹⁴⁾
 S. Narita,⁽²⁴⁾ U. Nauenberg,⁽⁵⁾ H. Neal,⁽³⁰⁾ G. Nesom,⁽¹⁷⁾ N. Oishi,⁽¹⁵⁾
 D. Onoprienko,⁽²³⁾ R.S. Panvini,⁽²⁷⁾ C.H. Park,⁽²²⁾ I. Peruzzi,⁽⁸⁾
 M. Piccolo,⁽⁸⁾ L. Piemontese,⁽⁷⁾ R.J. Plano,⁽²⁰⁾ R. Prepost,⁽²⁹⁾
 C.Y. Prescott,⁽²¹⁾ B.N. Ratcliff,⁽²¹⁾ J. Reidy,⁽¹²⁾ P.L. Reinertsen,⁽²⁶⁾
 L.S. Rochester,⁽²¹⁾ P.C. Rowson,⁽²¹⁾ J.J. Russell,⁽²¹⁾ O.H. Saxton,⁽²¹⁾
 T. Schalk,⁽²⁶⁾ B.A. Schumm,⁽²⁶⁾ J. Schwiening,⁽²¹⁾ V.V. Serbo,⁽²¹⁾
 G. Shapiro,⁽¹⁰⁾ N.B. Sinev,⁽¹⁶⁾ J.A. Snyder,⁽³⁰⁾ H. Staengle,⁽⁶⁾ A. Stahl,⁽²¹⁾
 P. Stamer,⁽²⁰⁾ H. Steiner,⁽¹⁰⁾ D. Su,⁽²¹⁾ F. Suckane,⁽²⁴⁾ A. Sugiyama,⁽¹⁵⁾

S. Suzuki,⁽¹⁵⁾ M. Swartz,⁽⁹⁾ F.E. Taylor,⁽¹³⁾ J. Thom,⁽²¹⁾ E. Torrence,⁽¹³⁾
 T. Usher,⁽²¹⁾ J. Va'vra,⁽²¹⁾ R. Verdier,⁽¹³⁾ D.L. Wagner,⁽⁵⁾ A.P. Waite,⁽²¹⁾
 S. Walston,⁽¹⁶⁾ A.W. Weidemann,⁽²³⁾ J.S. Whitaker,⁽⁴⁾ S.H. Williams,⁽²¹⁾
 S. Willocq,⁽¹¹⁾ R.J. Wilson,⁽⁶⁾ W.J. Wisniewski,⁽²¹⁾ J.L. Wittlin,⁽¹¹⁾
 M. Woods,⁽²¹⁾ T.R. Wright,⁽²⁹⁾ R.K. Yamamoto,⁽¹³⁾ J. Yashima,⁽²⁴⁾
 S.J. Yellin,⁽²⁵⁾ C.C. Young,⁽²¹⁾ H. Yuta.⁽¹⁾

(The SLD Collaboration)

⁽¹⁾*Aomori University, Aomori, 030 Japan,*

⁽²⁾*University of Bristol, Bristol, United Kingdom,*

⁽³⁾*Brunel University, Uxbridge, Middlesex, UB8 3PH United Kingdom,*

⁽⁴⁾*Boston University, Boston, Massachusetts 02215,*

⁽⁵⁾*University of Colorado, Boulder, Colorado 80309,*

⁽⁶⁾*Colorado State University, Ft. Collins, Colorado 80523,*

⁽⁷⁾*INFN Sezione di Ferrara and Università di Ferrara, I-44100 Ferrara, Italy,*

⁽⁸⁾*INFN Lab. Nazionali di Frascati, I-00044 Frascati, Italy,*

⁽⁹⁾*Johns Hopkins University, Baltimore, Maryland 21218-2686,*

⁽¹⁰⁾*Lawrence Berkeley Laboratory, University of California, Berkeley, California 94720,*

⁽¹¹⁾*University of Massachusetts, Amherst, Massachusetts 01003,*

⁽¹²⁾*University of Mississippi, University, Mississippi 38677,*

⁽¹³⁾*Massachusetts Institute of Technology, Cambridge, Massachusetts 02139,*

⁽¹⁴⁾*Institute of Nuclear Physics, Moscow State University, 119899, Moscow, Russia,*

⁽¹⁵⁾*Nagoya University, Chikusa-ku, Nagoya, 464 Japan,*

⁽¹⁶⁾*University of Oregon, Eugene, Oregon 97403,*

⁽¹⁷⁾*Oxford University, Oxford, OX1 3RH, United Kingdom,*

⁽¹⁸⁾*INFN Sezione di Perugia and Università di Perugia, I-06100 Perugia, Italy,*

⁽¹⁹⁾*Rutherford Appleton Laboratory, Chilton, Didcot, Oxon OX11 0QX, United Kingdom,*

⁽²⁰⁾*Rutgers University, Piscataway, New Jersey 08855,*

⁽²¹⁾*Stanford Linear Accelerator Center, Stanford University, Stanford, California 94309,*

⁽²²⁾*Soongsil University, Seoul, Korea 156-743,*

⁽²³⁾*University of Tennessee, Knoxville, Tennessee 37996,*

⁽²⁴⁾*Tohoku University, Sendai 980, Japan,*

⁽²⁵⁾*University of California at Santa Barbara, Santa Barbara, California 93106,*

⁽²⁶⁾*University of California at Santa Cruz, Santa Cruz, California 95064,*

⁽²⁷⁾*Vanderbilt University, Nashville, Tennessee 37235,*

⁽²⁸⁾*University of Washington, Seattle, Washington 98105,*

⁽²⁹⁾*University of Wisconsin, Madison, Wisconsin 53706,*

⁽³⁰⁾*Yale University, New Haven, Connecticut 06511.*

BIBLIOGRAPHY

- [1] S. L. Glashow, Nucl. Phys. **22**, 579 (1961).
- [2] S. Weinberg, Phys. Rev. Lett. **19**, 1264 (1967).
- [3] A. Salam, in *Proceedings of the Eighth Nobel Symposium held May 19-25, 1968*, edited by N. Svartholm (Almqvist & Wiksells, Aspenasgarden, Lerum in the county of Alvsborg, Sweden, 1968), p. 367.
- [4] K. Kodama *et al.*, Phys. Lett. **B504**, 218 (2001).
- [5] B. Baller *et al.*, Nucl. Phys. B, Proc. Supp. **98**, 43 (2001).
- [6] B. Kayser, Phys. Rev. D **66**, 392 (2002).
- [7] D. Abbaneo *et al.*, hep-ex **0112021** (2001).
- [8] K. Hagiwara *et al.*, Phys. Rev. D **66** (2002).
- [9] K. Abe *et al.*, Phys. Rev. Lett. **84**, 5945 (2000).
- [10] C. Y. Prescott, W. B. Atwood, R. L. Cottrell, et al., Phys. Lett. **B84**, 524 (1979).
- [11] G. Arnison *et al.*, Phys. Lett. **B122**, 103 (1983).
- [12] G. Arnison *et al.*, Phys. Lett. **B126**, 398 (1983).
- [13] D. C. Kennedy, B. W. Lynn, C. J. C. Im, et al., Nucl. Phys. **B321**, 83 (1989).
- [14] M. Bohm and W. Hollik, Nucl. Phys. **B204**, 45 (1982).
- [15] H. J. Bhabha, Proceedings of the Roayl Society of London. Series A, Mathematical and Physical Sciences **152**, 559 (1935).
- [16] M. B. Smy, Ph.D. thesis, Colorado State University [SLAC Report No. 515, 1997]
- [17] P. C. Rowson, D. Su, and S. Willocq, Ann. Rev. Nucl. Part. Sci. **51**, 345 (2001).
- [18] P. Comas and M. Martinez, Z. Phys. **C58**, 15 (1993).
- [19] H. Anlauf, H.-D. Dahmen, P. Manakos, et al., hep-ex **9512006** (1995).
- [20] Dmitri Yu. Bardin *et al.*, Comput. Phys. Commun. **133**, 229 (2001).
- [21] S. Wolfram, *The Mathematica Book, 4th ed.* (Wolfram Media/Cambridge University Press, Champaign, Illinois, 1999).
- [22] G.S. Abrams *et al.*, Phys. Rev. Lett. **63**, 724–727 (1989).
- [23] SLAC Linear Collider Conceptual Design Report, SLAC-R-0229 (1980)
- [24] R. Alley *et al.*, Nucl. Instrum. Methods Phys. Res., Sect. A **A365**, 1 (1995).
- [25] J. T. Seeman, Ann. Rev. Nucl. Part. Sci. **41**, 389 (1991).

- [26] E. M. Reuter and J. A. Hodgson, in *IEEE 1991 Particle Accelerator Conference (APS Beam Physics)*, San Francisco, California, 1991), p. 1996.
- [27] J. E. Clendenin, High Yield Positron Systems for Linear Colliders, SLAC-PUB-4743 (1989)
- [28] R. Pitthan, H. Braun, J. E. Clendenin, et al., in *IEEE 1991 Particle Accelerator Conference (APS Beam Physics)*, San Francisco, California, 1991), p. 2098.
- [29] T. Limberg, P. Emma, and R. Rossmanith, in *1993 IEEE Particle Accelerator Conference (PAC 93)*, Washington, DC, 1993), p. 429.
- [30] R. D. Elia, Ph.D. thesis, Stanford University [SLAC Report No. 429, 1994]
- [31] R. C. King, Ph.D. thesis, Stanford University [SLAC Report No. 452, 1995]
- [32] E. C. Torrence, Ph.D. thesis, Massachusetts Institute of Technology [SLAC Report No. 509, 1997]
- [33] A. Lath, Ph.D. thesis, Massachusetts Institute of Technology [SLAC Report No. 454, 1994]
- [34] R. C. Field, M. Woods, J. Zhou, et al., *IEEE Trans. Nucl. Sci.* **45**, 670 (1998).
- [35] D. V. Onoprienko, Ph.D. thesis, University Of Tennessee [UMI-99-85660, 2000]
- [36] D. Griffiths, *Introduction to Elementary Particles* (John Wiley & Sons, Inc., 1987).
- [37] M.E. Levi *et al.*, SLAC-PUB **4921**, 3 (1989).
- [38] G. Blaylock, SLD Physics Note **22**, 11 (1993).
- [39] P. C. Rowson, R. Frey, S. Hertzbach, et al., SLD Note **264**, 18 (1999).
- [40] K. Abe *et al.*, *Phys. Rev. Lett.* **78**, 2075 (1997).
- [41] M. Fero, P. L. Reinersten, B. A. Schumm, et al., SLD Physics Note **50**, 55 (1996).
- [42] J. P. Fernandez, SLD Physics Note **258**, 5 (1999).
- [43] SLD Design Report, SLAC-R-0273 (1984)
- [44] C. J. S. Damerell *et al.*, *Nucl. Instrum. Methods Phys. Res.* **A288**, 236 (1990).
- [45] K. Abe *et al.*, *Nucl. Instrum. Methods Phys. Res.* **A400**, 287 (1997).
- [46] M. J. Fero, D. C. Williams, M. D. Hildreth, et al., *Nucl. Instrum. Methods Phys. Res.* **A367**, 111 (1995).
- [47] H. Staengle, Ph.D. thesis, Colorado State University [SLAC Report No. 549, 1999]
- [48] T. J. Pavel, Ph.D. thesis, Stanford University [SLAC Report No. 491, 1996]
- [49] J. Va'vra, *Nucl. Instrum. Methods Phys. Res.* **A433**, 59 (1999).
- [50] K. Abe *et al.*, *Nucl. Instrum. Methods Phys. Res.* **A343**, 74 (1994).
- [51] J. E. Brau, *Nucl. Instrum. Methods* **A312 Erratum-ibid.A320:612,1992**, 483 (1992).

- [52] IEEE Standards Board, *IEEE Standard FASTBUS Modular High-Speed Data Acquisition and Control System* (The Institute of Electrical and Electronics Engineers, Inc., 1985).
- [53] K. T. Pitts, Ph.D. thesis, University of Oregon [SLAC Report No. 446, 1994]
- [54] A. C. Benvenuti *et al.*, Nucl. Instrum. Methods Phys. Res. **A290**, 353 (1990).
- [55] D. C. Williams, Ph.D. thesis, Massachusetts Institute of Technology [SLAC Report No. 445, 1994]
- [56] S. C. Berridge *et al.*, IEEE Trans. Nucl. Sci. **39**, 1242 (1992).
- [57] W. R. Nelson, H. Hirayama, and D. W. O. Rogers, SLAC-Report **0265**, 398 (1985).
- [58] R. Frey, Personal Communication (1995)
- [59] T. Duncan, Capacitive Coupling Cross-Talk in Kapton Multiconductor Cables (1995)
- [60] J. Bogart, J. Huber, and J. J. Russell, LUM Note **94-01**, 6 (1994).
- [61] R. Brun, F. Bruyant, M. Maire, et al., GEANT3, CERN-DD/EE/84-1 (1987)
- [62] S. L. White, Ph.D. thesis, University of Tennessee [UMI-96-19664, 1995]
- [63] J. Hylen, J. A. J. Matthews, G. Bonvicini, et al., Nucl. Instrum. Methods Phys. Res. **A317**, 453 (1992).
- [64] Barbiellini, Nucl. Instrum. Methods **123**, 125 (1975).
- [65] J. F. Crawford, E. B. Hughes, L. H. O'Neill, et al., Nucl. Instrum. Methods **127**, 173 (1975).
- [66] L.H. O'Neill *et al.*, Phys. Rev. Lett. **37**, 395 (1976).
- [67] S. Jadach, E. Richter-Was, B. F. L. Ward, et al., in *26th International Conference on High-energy Physics*, edited by J. R. Sanford, Dallas, TX, USA, 1992).
- [68] S. Jadach, W. Placzek, E. Richter-Was, et al., Comput. Phys. Commun. **102**, 229 (1997).
- [69] F. A. Berends, R. Kleiss, and W. Hollik, Nuclear Physics **B304**, 712 (1988).
- [70] G. Grindhammer, M. Rudowicz, and S. Peters, Nucl. Instrum. Methods **A290**, 469 (1990).
- [71] K. Pitts, LUM Note **93-01**, 14 (1993).
- [72] F. A. Berends, R. Kleiss, and W. Hollik, Nucl. Phys. **B304**, 712 (1988).
- [73] M. Huffer, Personal Communication (2002)
- [74] J. J. Russell, Personal Communication (2002)
- [75] M. Caffo *et al.*, in *Z physics at LEP 1*, edited by G. Altarelli, R. Kleiss and C. Verzegnassi, Geneva, 1989), p. 171.
- [76] D. R. Yennie, S. C. Frautschi, and H. Suura, Ann. Phys. **13**, 379 (1961).
- [77] M. Bohm, A. Denner, and W. Hollik, Nucl. Phys. **B304**, 687 (1988).

- [78] F. A. Berends, W. L. van Neerven, and G. J. H. Burgers, Nucl. Phys. **B297**, 429 (1988).
- [79] D. Levinthal, F. Bird, R. G. Stuart, et al., Z. Phys. **C53**, 617 (1992).
- [80] S. Gonzalez, SLD Physics Note **24** (1993).
- [81] W. Verkerke and D. Kirkby, RooFit (v 01-00-02 of July 2, 2002),
<http://roofit.sourceforge.net/>
- [82] R. Brun and F. Rademakers, Nucl. Instrum. Methods Phys. Res. **A389**, 81 (1997).
- [83] F. James and M. Roos, Comput. Phys. Commun. **10**, 343 (1975).
- [84] P. C. Rowson, SLD Note **251** (1996).